https://lib.uliege.be https://matheo.uliege.be

Mémoire

Auteur : Christopher, Steven
Promoteur(s) : Nazé, Yaël
Faculté : Faculté des Sciences
Diplôme : Master en sciences spatiales, à finalité approfondie
Année académique : 2022-2023
URI/URL : http://hdl.handle.net/2268.2/18698

Avertissement à l'attention des usagers :

Tous les documents placés en accès ouvert sur le site le site MatheO sont protégés par le droit d'auteur. Conformément aux principes énoncés par la "Budapest Open Access Initiative"(BOAI, 2002), l'utilisateur du site peut lire, télécharger, copier, transmettre, imprimer, chercher ou faire un lien vers le texte intégral de ces documents, les disséquer pour les indexer, s'en servir de données pour un logiciel, ou s'en servir à toute autre fin légale (ou prévue par la réglementation relative au droit d'auteur). Toute utilisation du document à des fins commerciales est strictement interdite.

Par ailleurs, l'utilisateur s'engage à respecter les droits moraux de l'auteur, principalement le droit à l'intégrité de l'oeuvre et le droit de paternité et ce dans toute utilisation que l'utilisateur entreprend. Ainsi, à titre d'exemple, lorsqu'il reproduira un document par extrait ou dans son intégralité, l'utilisateur citera de manière complète les sources telles que mentionnées ci-dessus. Toute utilisation non explicitement autorisée ci-avant (telle que par exemple, la modification du document ou son résumé) nécessite l'autorisation préalable et expresse des auteurs ou de leurs ayants droit.

FACULTY OF SCIENCES

—

MASTERS IN SPACE SCIENCES

Under the supervision of Prof. Y. Nazé

Optical & X-ray study of the Be + sdO binary ϕ Persei

Steven Christopher

2022 to 2023

Acknowledgements

First of all, I would like to thank my supervisor Professor Yaël Nazé as well as Professor Grégor Rauw for proposing this subject and thus allowing me to contribute to the ongoing study of such a fascinating object. Professor Nazé's guidance and feedback has been invaluable in the completion of this work

I would also like to thank the members of my reading committee, consisting of Professors Grégor Rauw and Damien Hutsemekers, and Dr. Yves Frémat, for taking time to read this work.

Finally I would like to thank my friends and family for their continuing support and advice on this journey, without which I may not have come this far.

Contents

1 Introduction

If one gazes into the northern night sky, from summer to autumn, one may find the constellation Perseus. Whilst home to the well-known bright stars Mirfak and Algol, Perseus is also home to other interesting stars. Among these lesser known but fascinating objects is ϕ Persei.

Part of a subset of rapidly rotating B-type stars known as Be stars that is only recently beginning to be understood, ϕ Persei is a binary system consisting of a Be star primary and an exotic stripped star companion. The first of very few such systems to have its companion directly detected, it is of great interest to the study of the mechanisms and evolution of Be stars. This is aided by its relative brightness, which makes it relatively easy to observe.

Our objective in this work is twofold: we will first use the wealth of optical data from amateur astronomers to obtain a new orbital solution. We will then utilise the Chandra X-ray telescope to characterise the X-ray emission of the system, with our orbital solution being used to determine if there is any dependence on the orbital phase.

The remainder of this section will introduce the Be stars as well as ϕ Persei. Section 2 will cover the reduction and initial analysis of the optical data. Section 3 will cover the methodology used to obtain a new orbital solution with the results in Section 4. Finally, the methodology and results of the X-ray analysis will be in Section 5.

1.1 Massive stars

It has long been known that not all stars are born equal. Indeed, depending on their mass, stars present different temperatures, luminosities and spectral characteristics. More specifically, temperature and luminosity increase with mass for main sequence stars. Stars are classified in term of their spectral characteristics into several types designated, in order of decreasing temperature: O, B, A, F, G, K and M. Within these spectral types, stars are further subclassified from 0 to 9 in order of decreasing temperature. Whilst all spectral types of stars form in groups within molecular clouds, the more massive and hotter O and B-type stars stand out: only the most massive molecular clouds (those massing several thousand solar masses) are capable of forming these stars, forming into groups of O and B type stars known as OB associations [46]. Both of these types of stars can be considered cosmic engines, shaping the environment around them. Indeed, both O and B-type stars present strong stellar winds, courtesy of their high temperatures and luminosities (30000-60000 K and over 30000-1400000 solar luminosities for O-type stars, 10000-30000 K and 25000-30000 solar luminosities for B-type stars).

1.2 Be stars

Among the non-supergiant B-type stars, those currently presenting or having presented Balmer emission lines in the past are known as Be stars. These Balmer lines are emitted by electronic transitions within the hydrogen atom, specifically from any value of the principal quantum number above $n = 2$ to $n = 2$. The line emitted from transition from $n = 3$ to $n = 2$ is known as Hα. The wavelength of the line is given by the Balmer formula:

$$\frac{1}{\lambda} = R\left(\frac{1}{4} - \frac{1}{n^2}\right) \tag{1}$$

Where R is the Rydberg constant, n is the initial value of the principal quantum number of the transitioning electron and λ is the wavelength of the emitted line.

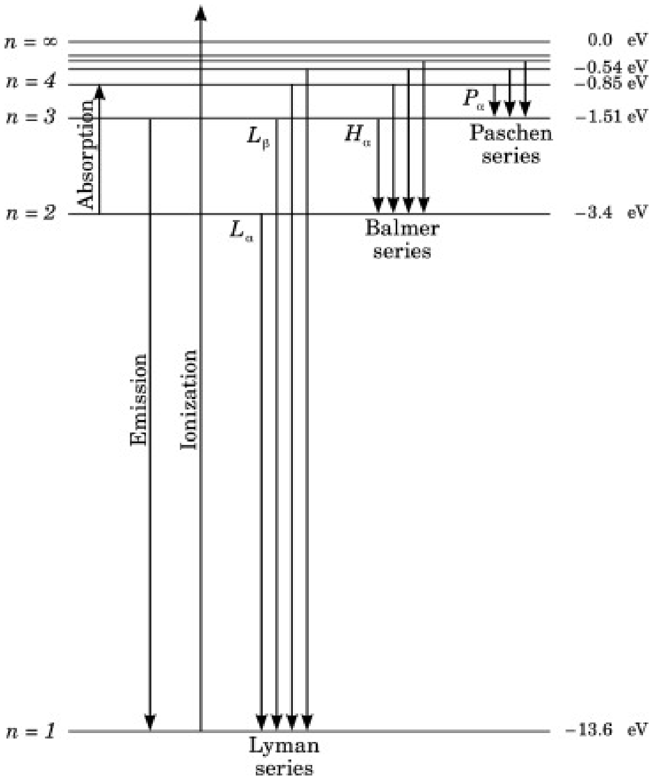

Figure 1: Overview of hydrogen spectral lines, including the Balmer series. From [23]

This broad definition for Be encompasses multiple types of stars, specifically the 'classical' Be stars, Herbig Ae/Be stars, Algol variables as well as the star σ Ori. Of these categories, 'classical' Be stars are characterised by the presence of circumstellar decretion disk. It is there that the Balmer emission arises (the spectral properties of the other Be type and other B-type stars are shown on figure 2). These stars rotate close to the critical limit at which their surface gravity is equal to the rotational centrifugal force, leading to mass loss in the form of a equatorial decretion disk [32]. Hereafter, the term 'Be star' will be used to refer to classical Be stars unless specified otherwise.

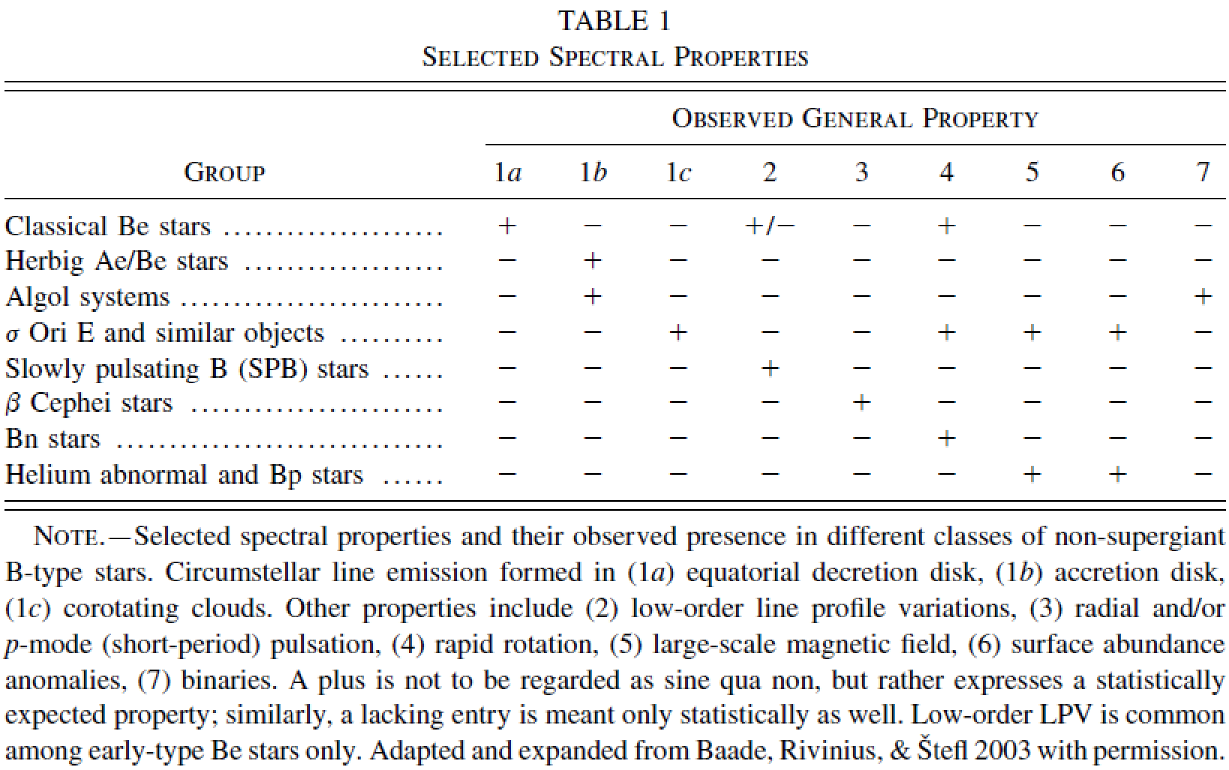

TABLE 1
SELECTED SPECTRAL PROPERTIES

GROUP	OBSERVED GENERAL PROPERTY								
	1*a*	1*b*	1*c*	2	3	4	5	6	7
Classical Be stars	+	−	−	+/−	−	+	−	−	−
Herbig Ae/Be stars	−	+	−	−	−	−	−	−	−
Algol systems	−	+	−	−	−	−	−	−	+
σ Ori E and similar objects	−	−	+	−	−	+	+	+	−
Slowly pulsating B (SPB) stars	−	−	−	+	−	−	−	−	−
β Cephei stars	−	−	−	−	+	−	−	−	−
Bn stars	−	−	−	−	−	+	−	−	−
Helium abnormal and Bp stars	−	−	−	−	−	−	+	+	−

NOTE.—Selected spectral properties and their observed presence in different classes of non-supergiant B-type stars. Circumstellar line emission formed in (1*a*) equatorial decretion disk, (1*b*) accretion disk, (1*c*) corotating clouds. Other properties include (2) low-order line profile variations, (3) radial and/or *p*-mode (short-period) pulsation, (4) rapid rotation, (5) large-scale magnetic field, (6) surface abundance anomalies, (7) binaries. A plus is not to be regarded as sine qua non, but rather expresses a statistically expected property; similarly, a lacking entry is meant only statistically as well. Low-order LPV is common among early-type Be stars only. Adapted and expanded from Baade, Rivinius, & Štefl 2003 with permission.

Figure 2: Table of non-supergiant B star spectral properties. Taken from [32]

1.3 Properties of Be stars

Be stars are primarily B-stars of spectral types B1 and B2 (noted B1e and B2e) . In addition to the HI and HeI absorption lines which make up most of the B-star's spectrum [32], Be stars present HI (specifically Hα), HeI and FeII emission lines as well as SiII and MgII in some cases. These lines are generally double-peaked due to the rapid rotation of the disk leading to the appearance of a blue-shifted peak and a red-shifted peak. Furthermore, certain Be stars present hydrogen emission lines with absorption cores and thin metallic absorption lines superimposed on a broader emission spectrum (as seen for o Aqr on figure 3). Such Be stars are known as shell stars [39].

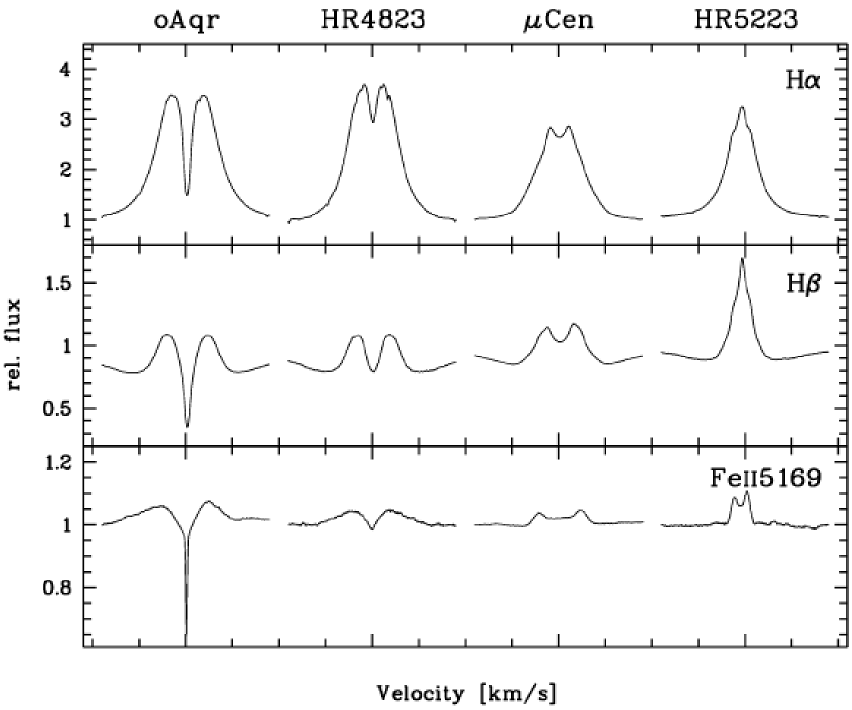

Figure 3: Line profiles of several classical Be stars. Velocity ticks are spaced by 250km/s. Taken from [32]

The shape of the lines depends on the inclination of star's rotation axis relative to the line of sight: if they are aligned (i.e. one of the star's poles is visible) the star will present single peaked emission lines. If the line of sight and axis are perpendicular (i.e. the disk is seen edge on), the star will present shell lines. Finally, if the line of sight and axis are neither perpendicular nor parallel the star will present double-peaked lines [39] (all 3 cases are illustrated on Figure 4).

In addition to emitting the Balmer lines which characterise Be stars, the disk presents an IR continuum brighter than that of the underlying star. This IR emission originates from free-free and bound-free transitions within the disk [32]. Interferometric observations of the Hα emissions of Be star's circumstellar material as well as the linear polarization angle of the star's continuum emissions show that this material does indeed take the shape of a disk, as done by Quirrenbach et al (1994) for ζ Tauri (see Figure 5)[34]

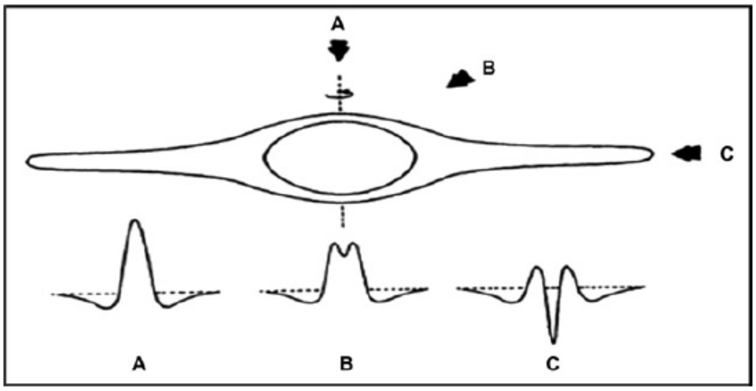

Figure 4: Line profiles and corresponding viewing directions. Taken from [39]

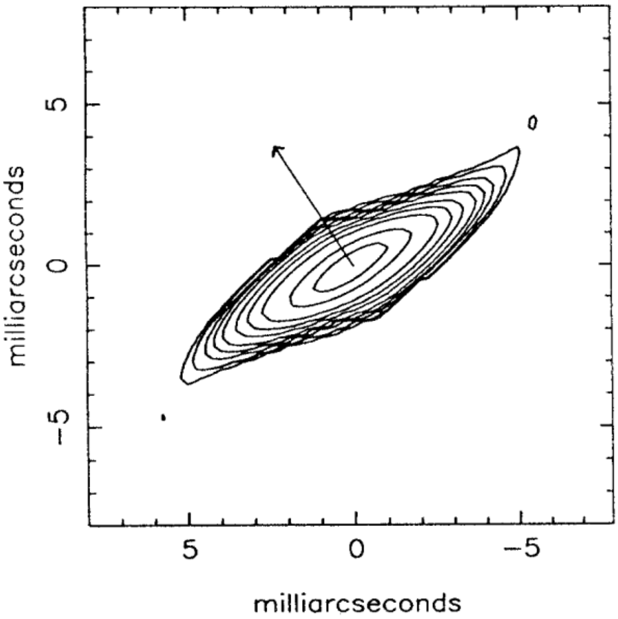

Figure 5: Hα emission map of ζ Tauri, revealing the disk-shaped circumstellar material. The arrow indicates the polarization angle, perpendicular to the disk's plane. Taken from [34]

In addition to the Hα emission, the disk is also the source of the HeI and FeII lines presented by classical Be stars. For the B1.5 Ve + sdO binary ϕ Persei in particular, modelling by Hummel and Štefl (2001) found that the HeI emmiting region is larger than the Hα emitting region's 10 stellar radii, extending to 15 stellar radii from the primary , putting it close to the edge of the primary's Roche lobe (16.9 stellar radii), concentrated on the side of the disk facing the sdO secondary. This suggests that the size of the disks of binary classical Be stars can be of the same order as the size of their Roche lobes[16]. However, in the case of a compact companion star, tidal interaction between the disk and the secondary star will lead to the disk becoming truncated [37].

Finally, some Be systems are known to be X-ray emitters. One such type of system is the Be/X-ray binary (BeXB), a subset of high-mass X-ray binaries (HMXB). These BeXB systems consist of a Be star and a neutron star, with X-ray emission arising from accretion of the Be star's disk onto the neutron star: specifically, accretion would occur at periastron as the neutron star would pass close to the disk, leading to transient Roche Lobe overflow of the disk. The neutron star may even pass through the disk at periastron, leading to a major disruption of the disk. It should be noted that BeXBs should be able to form with black holes or white dwarves as the accreting companion[37]. These systems, while rare, have been detected: a few Be/WD X-ray binaries have been identified in the LMC and SMC via their supersoft X-ray emission[17], and the first Be/BH (MWC 656) was discovered using radial velocity measurements in 2014, with X-ray emission being discovered later that same year [25]. Finally, there are the γ Cas stars, a subset of Be stars presenting very hard and bright X-ray emission, more luminous than the typical emission of massive stars but less than an HMXB. Their emission is thought to arise from two possible mechanisms: the first consists of accretion onto a compact companion, either a white dwarf or a neutron star accreting in the so called "propeller regime"[26] in which the neutron star's magnetic field prevents direct accretion, forming instead an X-ray emitting shell[33]. The second involves interaction between a stellar magnetic field arising from sub-surface convection and a magnetic field arising from instabilities within the disk. There is also a third model involving the collision between the wind of a stripped star companion and the Be primary's disk. However this last model was found to be unlikely by Nazé et al (2022)[27].

1.4 Spin-up and disk formation

Whilst the decretion disk originates from both the rapid rotation of the Be star as well as a mechanism ejecting matter from the surface, an explanation for this rapid rotation and ejection is still required. Three possible causes for the rotation have been considered:

1. The rapid rotation may occur due to a transfer of angular momentum from the inner regions of the star to the surface: after an initial transfer of angular momentum from the surface to the inner regions at the start of the main sequence, this trend is reversed leading to an increase of the outer layer's rotation rate. As the hydrogen in the star's core is depleted, the contraction of the star and subsequent angular momentum transfer lead to the spin-up of the star. Therefore if the star's initial rotation rate is high enough, it is possible for this mechanism to increase this rate to near the critical limit [22].

2. Be stars are simply born as rapid rotators. This proposed explanation is backed up by Zorec and Briot (1997), who found that the frequency of Be stars amongst the B spectral type is of 17% (when considering all spectral subtypes). This value is larger than would

be expected if Be stars were largely spun up during their contraction at the end of the main sequence [51].

3. The rapid rotation is due to mass transfer from a more massive, more evolved companion overflowing its Roche lobe to the Be star progenitor in a close binary system. This mass transfer increases the angular velocity of the Be progenitor, thus speeding up its rotation. Post mass-transfer, these systems should consist of a Be star as well as either a stripped-envelope star (also known as a helium star), a white dwarf or a neutron star [30]. This binary explanation is backed up by the observation of Be + NS X-ray binaries, Be + stripped star binaries and supersoft X-ray emitting Be + WD binaries, as well as by the radial velocity variations of some Be stars being consistent with orbital motion[26]. Despite the ratio of Be + NS binaries to other Be binary types being estimated by Shao and Li (2014) [45] at 1/1000 (excluding Be + BH), few Be + WD and Be + stripped star binaries have been detected [26]. For the latter case, Schootemeijer et al (2018) argue that this apparent scarcity is due to the evolutionary state of most stripped stars: some of the helium star companions detected so far (such as ϕ Persei) are in the short-lived helium shell-burning phase whereas most others (97% to 98% of stars of similar mass to ϕ Persei's companion) are in the helium core-burning phase and thus fainter by nearly an order of magnitude [42].

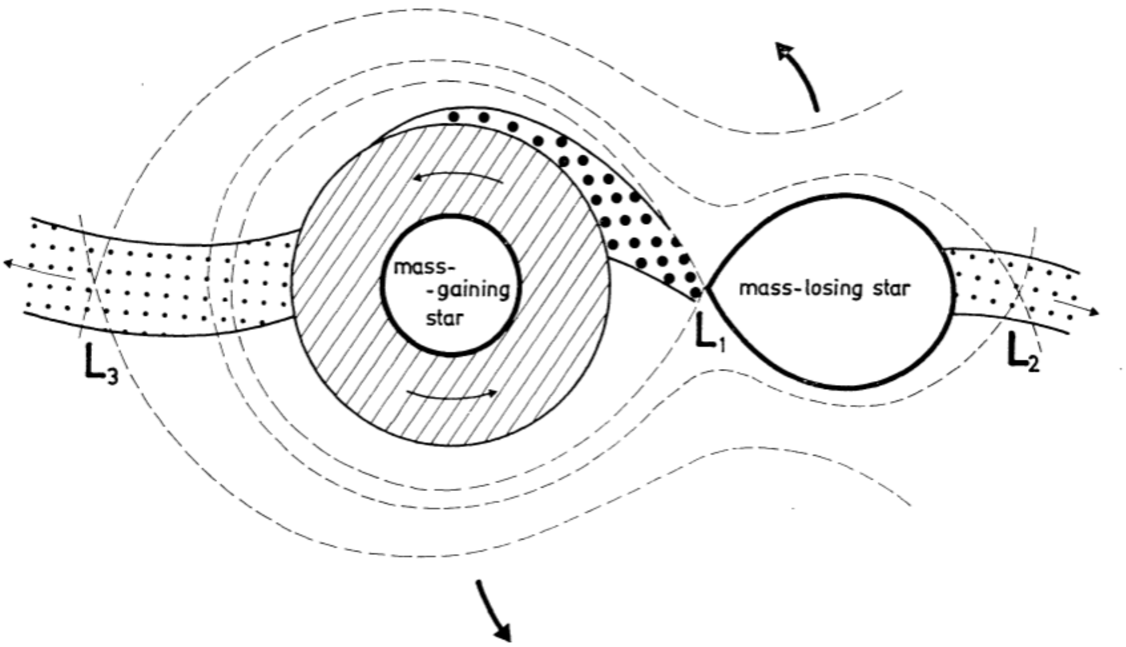

Figure 6: Schematic of mass transfer in a binary system. The bold arrows illustrate the motion of the system's components and the light ones the motion of gas. The dotted lines represent Roche equipotentials. The hatched area represents the disk around the mass gaining component. The bold dotted area shows the flow from the mass losing component to the disk, whereas the two small dotted areas represent possible paths for the flow of material out of the system. Taken from [19]

It should be noted that the mean rotation velocity of Be stars has been estimated to be in the range of 70% to 80% of the critical limit. This result was found assuming the disk was seen edge-on, and using measurements of photospheric line widths. It should also be noted that this method is likely to produce underestimates of the star's rotation velocity: the rapid rotation causes the star to become more oblate, leading to a decrease in temperature and brightness near the equator, and conversely an increase at the poles. This effect, known as gravity darkening, causes an apparent narrowing of the lines. As such the average rotation rate may be higher [32].

If the star is not rotating at the critical limit, an additional 'push' is needed for matter to escape the surface and form the disk. In the case of hot stars, this can simply be from line-driven wind. However gravity darkening will increase the wind away from the equator in a rapidly spinning star. In lower temperature cases, this push could be provided by pulsations of the star's photosphere: these pulsations lead to lower effective gravity on the surface, low enough for radiation pressure to push matter away from the photosphere [32].

Finally, the ejected matter must form a disk. Three models have been proposed [32]:

1. Wind-compressed disks (WCD) require only rapid rotation of the star and stellar winds: the very rapid rotation of the star and thus of its higher-latitude wind could lead to the streamlining (by means of orbital mechanics) of the wind towards the equatorial plane. The resulting shock from the converging high-latitude and equatorial winds compresses the ejected matter into a dense disk[3]. This model fails to reproduce the observed characteristics of decretion disks, such as their strong IR emission with WCD models predicting emissions weaker by several orders of magnitude than those of observed disks [31]. In addition, gravity darkening would cause an increase of wind in the polar regions rather than the equatorial regions, whilst the oblateness of the rapidly rotating star would cause the radiative force to be directed away from its equator. Both of these effects weaken the streamlining towards the equatorial region the WCD mechanism requires [8].
2. Magnetic wind-compressed disks (MWCD) could explain the shortcomings of the previous model by having the star's magnetic field channel the wind from higher latitudes towards the equatorial plane[7]. Furthermore, models of MWCDs have been shown to produce IR emissions in line with observed Be stars, unlike the WCD mechanism[31]. However, whilst magnetohydrodynamic simulations of this mechanism ignoring the rotation of the star itself do produce disks matching those observed, those including the star's rotation (and thus that of its magnetic field) do not, with such disks having larger rotation and radial outflow velocities than the Keplerian velocities in observed Be star disks[32][29]. Furthermore, observed Be stars do not possess the large scale magnetic fields required for the MWCD mechanism. Finally, it has also been found that strong magnetic fields will very rapidly destroy the Keplerian disks expected around Be stars, making MWCD a non-viable explanation for Be stars[49].
3. Viscous disks form when the matter flows out at speeds slightly above Keplerian rotation speeds and spreads outwards under the action of turbulent viscosity. Such disks are also predicted to be geometrically thin as well as to have a steep density drop-off[5]. These viscous models are backed up by interferometric observations of Be stars revealing Keplerian disks with emissions matching those predicted by viscous disk models [18].

1.5 Disk and Be star variability

Be stars exhibit variability, both on short and long timescales. On the short term (minutes or days), the line profiles of Be stars have been observed to vary. This variation has been attributed to non-radial pulsations, and in the case of variation periods matching the rotation period, to sunspots or corotating circumstellar clouds [32].

On the long term (on the scale of years to decades), the star's disk may exhibit variations as well. Specifically, several Be star's disks displayed variations of their double-peaked emission lines, with the ratio V/R of heights of the blue-shifted (V) and red-shifted (R) peaks exhibiting cyclical behaviour [32]. The source of this variation has been interpreted as a one-armed spiral density wave in a viscous disk (as shown on figure 7). Finally, some Be stars have been observed to completely lose their disk before rebuilding them. The dissipation of the disk is thought to be caused by strong radiation driven wind forming within the disk itself or from the disk material being ablated away by the star's radiation[32].

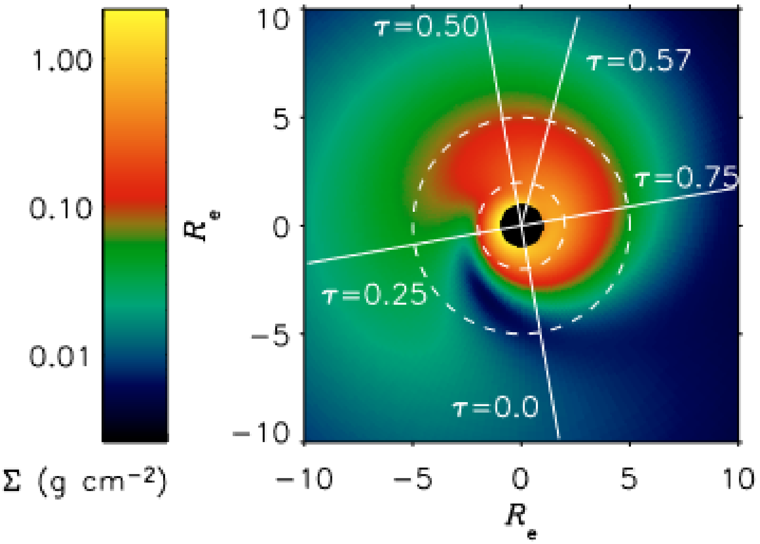

Figure 7: Model of a spiral density wave in the disk of ζ Tauri. τ is the phase of the V/R variation with $\tau = 0$ corresponding to the maximum value of V/R. The line of sight for five values of τ are marked. Taken from [6]

1.6 ϕ Persei

1.6.1 General characteristics

The subject of this thesis is the shell star ϕ Per (HD 10516), a B1.5 Ve + sdO binary with an apparent V magnitude of 4.07. As it is a classical Be star, the primary possesses a circumstellar decretion disk emitting Balmer, HeI and FeII lines as well as IR continuum radiation. The stripped star companion on the other hand, emits primarily in the UV domain [16]. Double-peaked HeII 4686 line is also emitted near the secondary [42].ϕ Per is located at a Gaia distance of 184 ± 8 pc from Earth [2]. Its distance makes it a likely member of the α Per cluster[24]. The orbital period of the secondary, as found by Mourard et al (2015), is of 126.6982 days with the assumption of a circular orbit [24] (this orbital solution is illustrated on Figure 8). Mourard et al (2015) further found the total mass of the system to be $10.8 \pm 0.5 M_{\odot}$. The primary is an exceptionally rapid rotator, with a rotation rate of 93% ± 0.8% of its critical rotation rate [24]. ϕ Per is one of few Be + sdO systems in which the stripped star secondary has been detected.

The secondary is in its helium shell burning phase. While in this short-lived phase, the star is significantly more luminous than in the previous helium core burning phase [42]. The orbital elements and characteristics of both components are summed up in Tables 1 and 2 respectively.

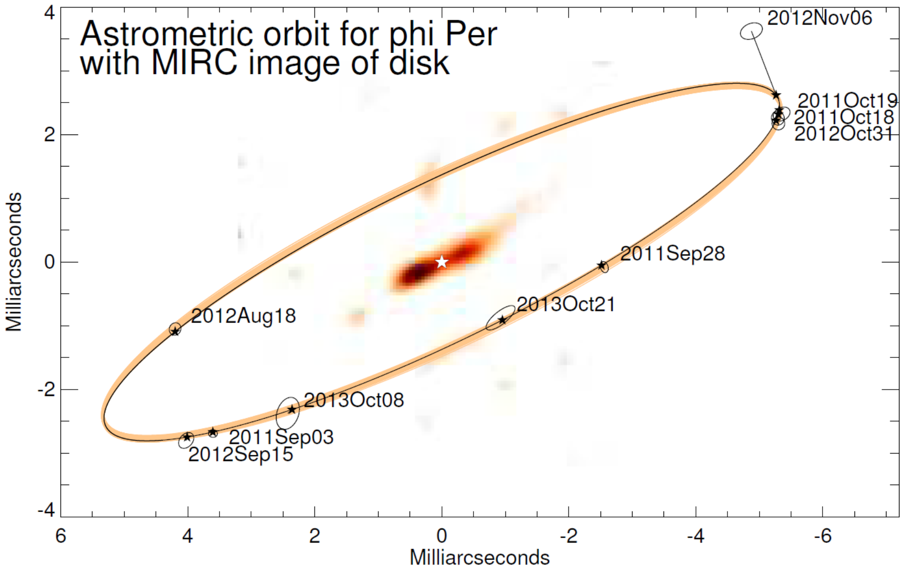

Figure 8: Reconstruction of H-band data taken using the CHARA optical interferometric array's MIRC instrument, showing the orbit of the secondary sdO around the Be primary as determined by Mourard et al (2015). Only the emissions from the disk are shown. The positions of the secondary at 10 different epochs are marked with their error ellipses and the orange outline of the orbit represents the errors on the orbital solution. Taken from [24]

Orbital elements of ϕ Per	
Period (d)	126.6982
Eccentricity (°)	0
Semi-major axis (mas)	5.89 ± 0.02
Inclination (°)	77.6 ± 0.3
Argument of periapsis (°)	0
Longitude of the ascending node (°)	-64.3 ± 0.3
Total mass ($M_\odot$)	10.8 ± 0.5

Table 1: Orbital elements and total mass of the ϕ Per binary as found by Mourard et al (2015). Values without error intervals were fixed for the calculated orbital solution. Data taken from [24]

Binary characteristics of ϕ Per		
	Primary	Secondary
Mass ($M_\odot$)	9.6 ± 0.3	1.2 ± 0.2
Luminosity ($log_{10}\,(L/L_\odot)$)	4.16 ± 0.10	3.8 ± 0.13
Effective temperature (kK)	29.3 ± 3	53 ± 3
Radius ratio (R_{sdO}/R_{Be})	0.20 ± 0.01	

Table 2: Characteristics of the ϕ Per binary's components. Taken from [24]

1.6.2 Disk characteristics

The decretion disk surrounding the primary exhibits Keplerian rotation. Furthermore, its rotation axis was found to be aligned with the system's orbital axis by Mourard et al (2015). In addition their interferometric observations found the inclination of the disk (75° ± 9°) to be very close to the orbital inclination (77.6° ± 0.3°). The position angle of the disk normal was found to match the system's intrinsic polarization angle. Furthermore, the longitude of the ascending node was found to match the position angle of the long axis of the projected disk. All of this indicates that the orbital axis and the disk's axis are co-aligned [24]. The disk presents an Hα emitting region that extends further out from the star than the IR continuum emitting region [24]. This can be seen on Figure 9, where the largest extent of the disk is seen close to Hα's 656.281 nm wavelength. Further disk properties are described in table 3.

In addition to Hα line and continuum regions, the disk also emits HeI 6678, HeI 5876 and FeII 5371 lines. Hummel and Štefl (2001) found that the FeII emitting region is axisymmetric and extends to 12 stellar radii from the primary, whereas the two HeI lines are emitted from a region extending to 15 stellar radii with the emission being strongly concentrated towards the secondary. It should be noted that the HeI region's radius is close to the primary's Roche radius (16.8 stellar radii), [16]. This could allow escaping gas to accrete onto the sdO secondary, leading to the formation of a circumsecondary disk. Such a disk could explain the double-peaked HeII 4686 emission observed around the secondary [24].

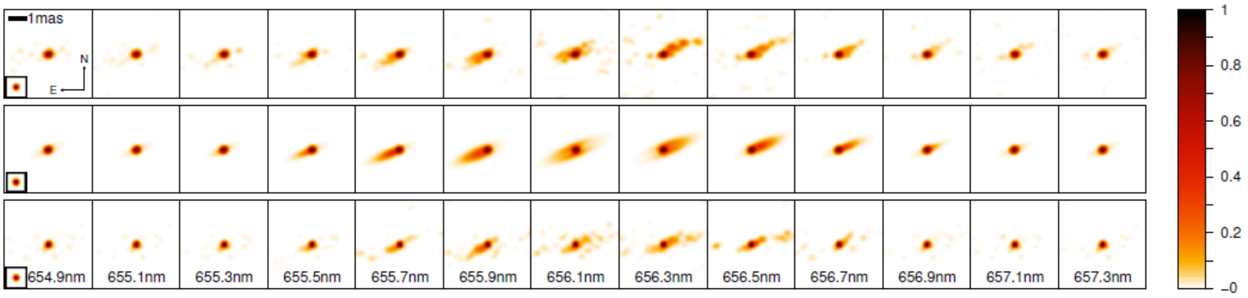

Figure 9: Intensity maps of ϕ Per as a function of wavelength. The top row shows intensity maps as imaged by the CHARA array's VEGA instrument. The middle row shows intensity maps derived from a kinematic model of the disk. The bottom row shows a simulated observation of the same kinematic model. Taken from [24]

Disk characteristics	
Inner radius rotational velocity (km/s)	450 ± 50
Disk continuum FWHM (stellar radii)	6.4 ± 3.4
Disk Hα FWHM (stellar radii)	11.9 ± 3.4
Disk inclination (°)	75 ± 9

Table 3: Taken from [24]

1.6.3 Variability of ϕ Per

ϕ Per exhibits multiple types of variability. Firstly, as a binary system, it exhibits changes in radial velocity resulting in spectral variation. Secondly, as a classical Be star, it exhibits the typical V/R variation. Thirdly, the system exhibits photometric variability, on both short and long-term scales[4]. The short-term variations consist of changes of up to 0.05 mag, occurring on scales on the order of a day. The long-term variations consist of brightening and fading over the course of several years, Božić et al (1995) finding that the change is positively correlated to the disk's Balmer emission [4]. This correlation is due to the increase (decrease) of the disk emission simply leading to an overall increase (decrease) of the brightness of the system [47]. The variation of the Balmer emission (specifically the Hα emission) will be covered in Section 2.2.

1.6.4 Past and future evolution

ϕ Per's primary likely evolved into a Be star via mass transfer from its companion. This is backed up by the direct detection of the stripped star secondary [10] as well as by the alignment of the circumprimary disk's rotation axis with the system's orbital axis [24]. Schootemeijer et al (2018), found that the system had an age of 57 ± 9 Myr, within the 52-60 Myr age range of the α Persei cluster[42]. ϕ Per's progenitor system was found to have had masses of 7.2 ± 0.4 $M_{\odot}$ for the initial primary and 3.8 ± 0.4 $M_{\odot}$ for the initial secondary, as well as an orbital period of 16 ± 4 days. As the initial primary evolved and overflowed its Roche lobe, the initial secondary star was spun up by the mass transfer, leaving it as the current Be primary of the system and the initial primary became the stripped star secondary [42].

Whilst initially neither star was massive enough to undergo a core collapse supernova, as a result of the mass transfer, the Be star is now expected to undergo such an event, with the sdO evolving towards a CO white dwarf. However, as the Be star evolves and fills its Roche lobe, mass transfer will once more occur, this time from the Be star to the sdO. Due to the significantly higher mass of the primary, the mass transfer is expected to further shrink the orbit, which may lead to the formation of a common envelope, with the likely outcome being a merger between the two stars[42].

1.7 Objectives

As previously alluded to, in this thesis we will present a long-term optical study of ϕ Per's circumprimary disk, as well as an X-ray study of the system. The optical data will be used to obtain a new orbital solution for ϕ Per which will then be used to characterise the X-ray emission. The optical data used consists of 186 amateur spectra covering a time span from 2001 to 2022. They were obtained from the BeSS database, operated at LESIA, Observatoire de Meudon, France: http://basebe.obspm.fr. The X-ray data was obtained using the Chandra X-ray Observatory. The basic data reduction for the optical spectra (bias and flat field corrections, wavelength calibration) were done by the amateur astronomers and the remaining steps will be covered in the next section.

2 Optical data

2.1 Data reduction

The first step of the data reduction was to reject spectra which were too low resolution or did not contain the Hα line. Eight spectra were rejected, three due to being too low resolution and the remainder due to not containing the Hα line. The rejected spectra are detailed in Table 4.

Characteristics of rejected spectra				
Observation date	Coordinate reference value (Å)	Wavelength increment (Å)	Telescope resolving power	Reason for rejection
08/08/2010	6494.7222	0.1215	17000	Low resolution
20/09/2012	8171.2331	0.363	4000	Hα not present
19/10/2014	3700.5	0.5	N/A	Low resolution
26/12/2015	4763.5224	0.0786	N/A	Hα not present
04/08/2019	3534.103	0.0915	2914	Hα not present
05/08/2019	3536.3632	0.0916	2925	Hα not present
24/08/2019	7458.9764	0.1799	2834	Hα not present
25/08/2019	5721.5374	0.1847	2371	Low resolution

Table 4: Characteristics of rejected Hα spectra. The coordinate reference value is the lowest wavelength value of the corresponding line profile.

2.1.1 Telluric correction

The second step of the data reduction was to correct for telluric contamination: due to the presence of molecules in the atmosphere absorbing specific wavelengths of light, telluric absorption lines appear in data from ground-based observations, particularly in the red and infrared region of the spectrum (with Hα belonging to the former). Absorption from trace components such as atmospheric water vapour and ozone are of particular concern due to their variability, whereas the more dominant components such as O_2 and N_2 remain mostly constant[1].

Due to the presence of telluric lines, most of the remaining 178 spectra require correction. This correction was carried out using the IRAF software, specifically its 'telluric' task. This task utilizes a calibration spectrum which approximates that of the telluric lines. The calibration spectrum is shifted and scaled to match the real spectrum, before the real spectrum is divided by the shifted and scaled calibration spectrum. This operation can be done automatically or manually, with the latter enabling fine tuning [61].

For this step, the calibration spectra used were sourced from Hinkle et al (2000) [14] and convolved by Gaussians of various widths to mimic different resolutions. The specific calibration spectrum to be used was chosen on a case by case basis. Of the 178 spectra, 148 presented strong telluric lines that required correction. An example of the telluric correction is shown on Figure 10.

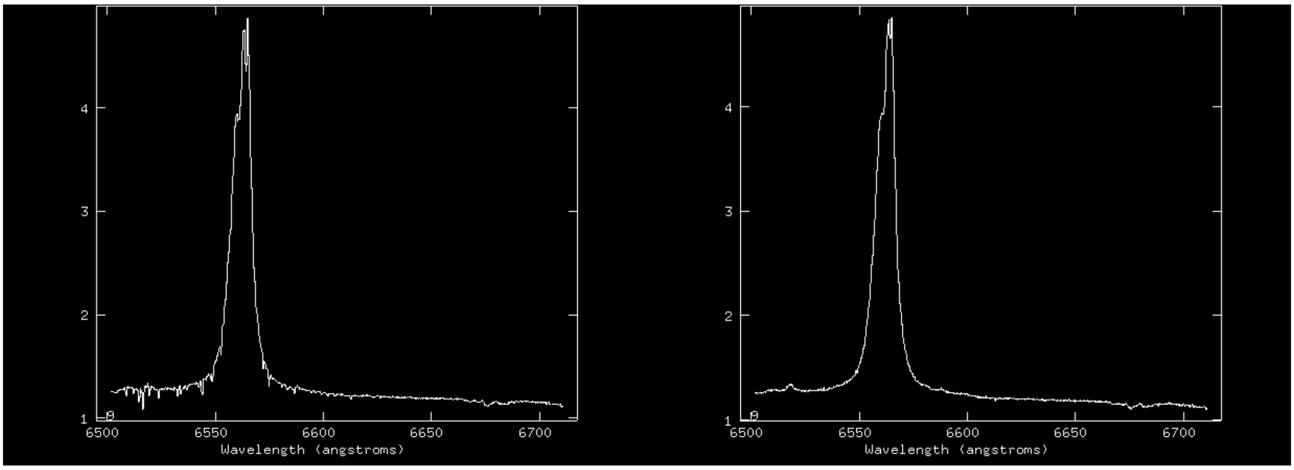

Figure 10: Comparison of the Hα profile of 05/09/2020 prior to (left) and after (right) telluric correction.

2.1.2 Continuum normalization

The third step was to normalize the star's continuum emission. By bringing the continuum to 1 across all spectra it can be used as reference value in later data analysis.

The normalization process was carried out using the MIDAS software[58] by dividing all 178 spectra by an approximation of the continuum. To create this approximation, a polynomial fit was done through a series of chosen windows. These windows were carefully chosen to allow for their use for all spectra. From time to time, an additional point was added manually to improve the results. For most of the 178 Hα spectra, a third order polynomial was used, with a fourth or fifth order polynomial used in the few cases for which the third order was insufficient. An example of the normalization process' results is shown on Figure 11.

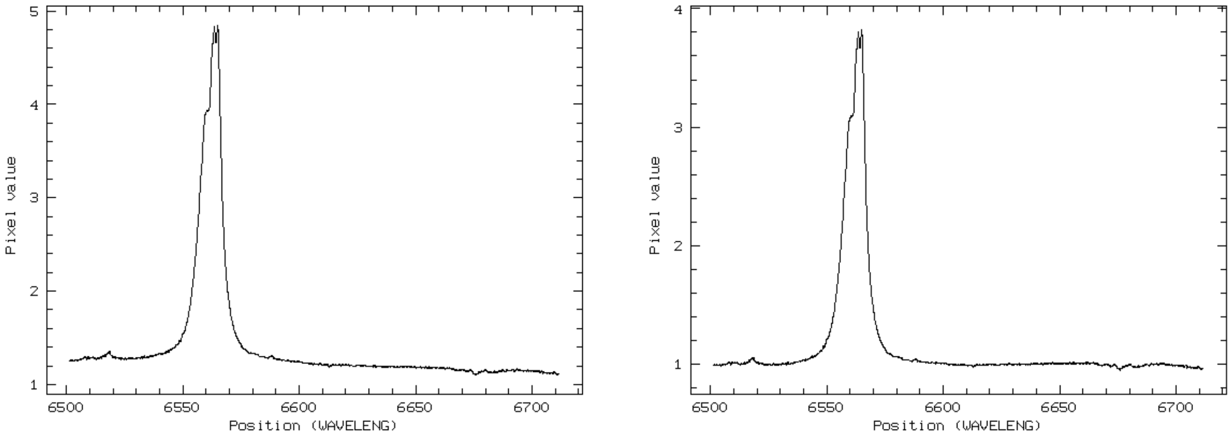

Figure 11: Comparison of the Hα profile of 05/09/2020 prior to (left) and after (right) normalization.

2.2 Line profiles

Before the data is analysed, it should be noted that the line profiles are expressed in terms of flux by wavelength. As the Hα lines are emitted from the decretion disk, the observed line width arises from the Doppler shift of the receding and advancing disk components. As such it is convenient to express the line profiles in terms of radial velocity of the disk components rather than wavelength. The radial velocities can simply be obtained using the Doppler effect formula:

$$\frac{\lambda}{\lambda_{H\alpha}} - 1 = \frac{RV}{c} \tag{2}$$

Where λ is the observed wavelength expressed in Å, $\lambda_{H\alpha} = 6562.85$ Å is the Hα wavelength, c is the speed of light and RV is the corresponding radial velocity.

In addition, the spectra must be corrected for the heliocentric motion of the Earth to get the true radial velocities of the target object at the time of observation. This value was provided in the headers of the data.

The line profiles as a function of radial velocity are shown on Figures 12, 13 and 14.

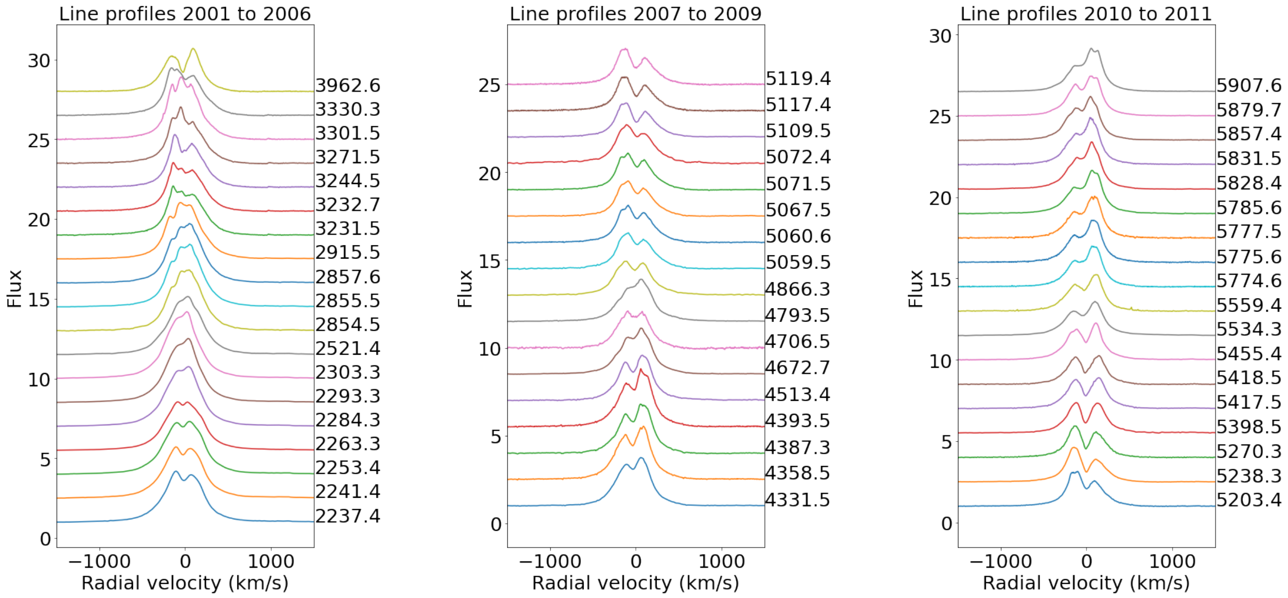

(a) (b) (c)

Figure 12: Hα line profiles from 2001 to 2011. The labels to the right of each profile are the Heliocentric Julian Date of the observation minus 2450000 days.

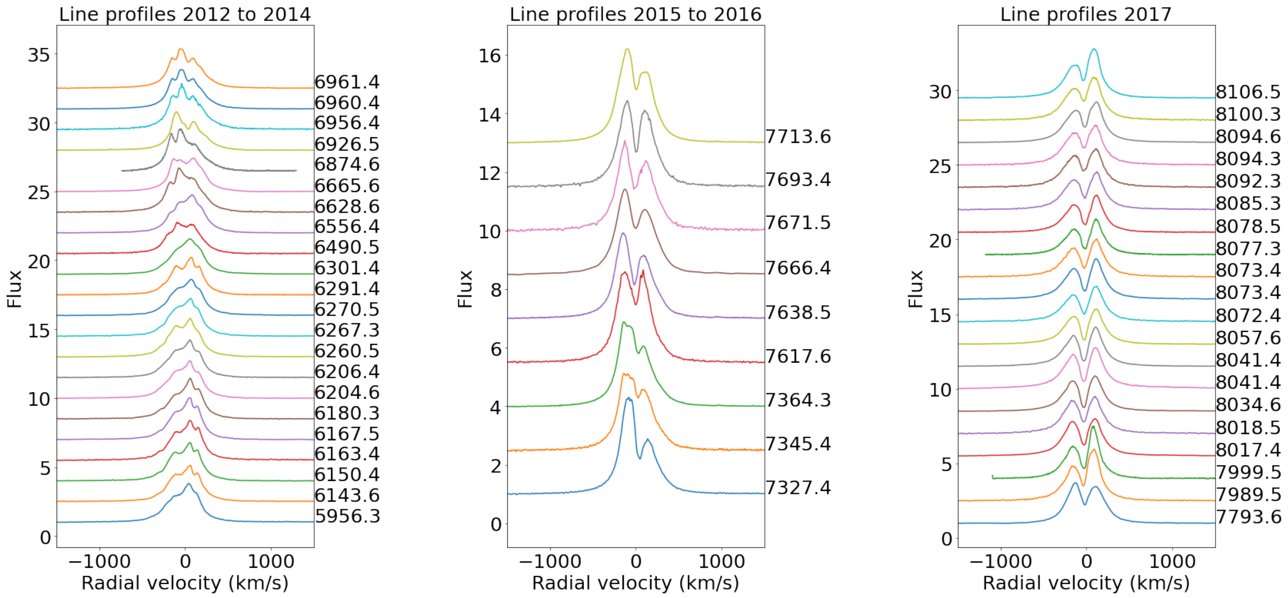

(a) (b) (c)

Figure 13: Hα line profiles from 2012 to 2017.

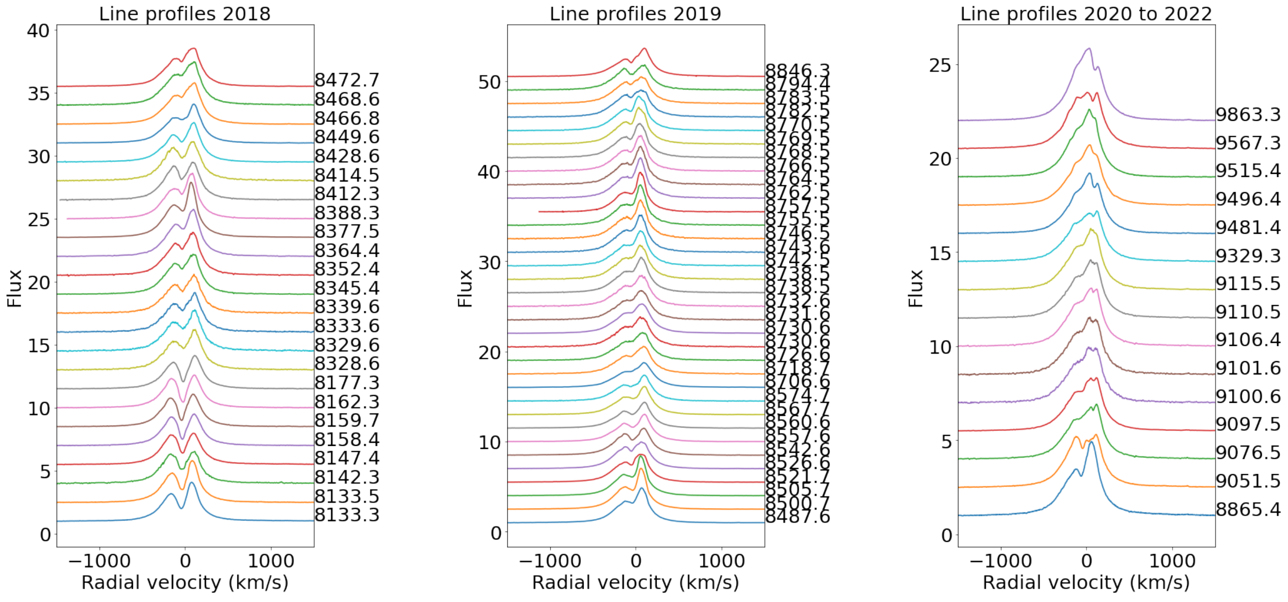

(a) (b) (c)

Figure 14: Hα line profiles from 2018 to 2022.

As can be seen on the above figures, the shape of the Hα line varies greatly over time: in addition to simple changes of the line's height, the line profiles also display changes in the dominant peak over time, as expected from the usual V/R variation in Be stars. The shape of the line's base is also seen to vary. Furthermore, in some years (such as on Figure 13b) the lines display absorption cores of varying depth, while other years the lines (such as on Figure 13a) display no absorption core at all with the lines appearing single-peaked. As previously explained, the presence or absence of the absorption core is dependent on the viewing angle. As such, warping or precession of the disk could cause the variation of the absorption core seen in some Be stars. Martin et al (2011) argue that such warping or precession could be due to the misalignment of the disk's rotation axis with the system's orbital axis, with the tidal forces of the companion then causing the warping or precession [21]. However, in the case of ϕ Per, the orbital and disk axes are co-aligned [24], making this explanation for the varying core unlikely. Hanuschik (1996) found that the outer edges of Be star disks are thicker than the inner regions which combined with high inclinations of around 70° (as a reminder, ϕ Per's disk's inclination is of $75^\circ \pm 9^\circ$) could lead to an increase (decrease) of central absorption as the outer radius of the disk increases (decreases) [13] (the variability of the size of Be star disks will be detailed later in this section). However, Hummel and Štefl (2001) argue that this explanation is not viable for ϕ Per as the presence of the companion constrains the disk's ability to grow [16]. Finally, the line sometimes becomes triple-peaked. Whilst the typical V/R variation can be attributed to spiral density waves, the appearance of a third emission peak requires another explanation.

Maintz et al (2004) found that the third emission peak may arise from the companion star illuminating a section of the disk[20], similarly to what Hummel and Štefl (2001) found for ϕ Per's HeI emission (see Section 1.6.2)[16]. In ϕ Per the third peak is visible in the amateur data from late 2003 to 2004 and from 2012 to 2014 (see Figures 12a and 13a respectively).

In order to properly characterise the variation of the disk Hα emission we can make use of the equivalent width. The equivalent width of the lines is used to measure the strength of a spectral feature. It is defined as the width a spectral feature would have were it a rectangular line with the intensity of the continuum emission whilst still having the same area, with the convention that it is negative for emission features. It is given by:

$$W_\lambda = \int \frac{F_c - F(\lambda)}{F_c} d\lambda \tag{3}$$

Where W_λ is the equivalent width F_c is the flux of the continuum and F is the flux of the spectral feature. Rewriting this in discrete form for the normalized continuum gives:

$$W_\lambda = -\sum_{i=1}^{N} (F_i - 1)\,\Delta\lambda \tag{4}$$

Where N is the total number of data points in a given line profile and $\Delta\lambda$ is the wavelength step between them. For the Hα profiles, the equivalent width calculation was carried out on a limited interval of -750 km/s to 750 km/s. This was done to ensure that only the Hα line itself is taken into account. The calculated equivalent widths are shown on Figure 15.

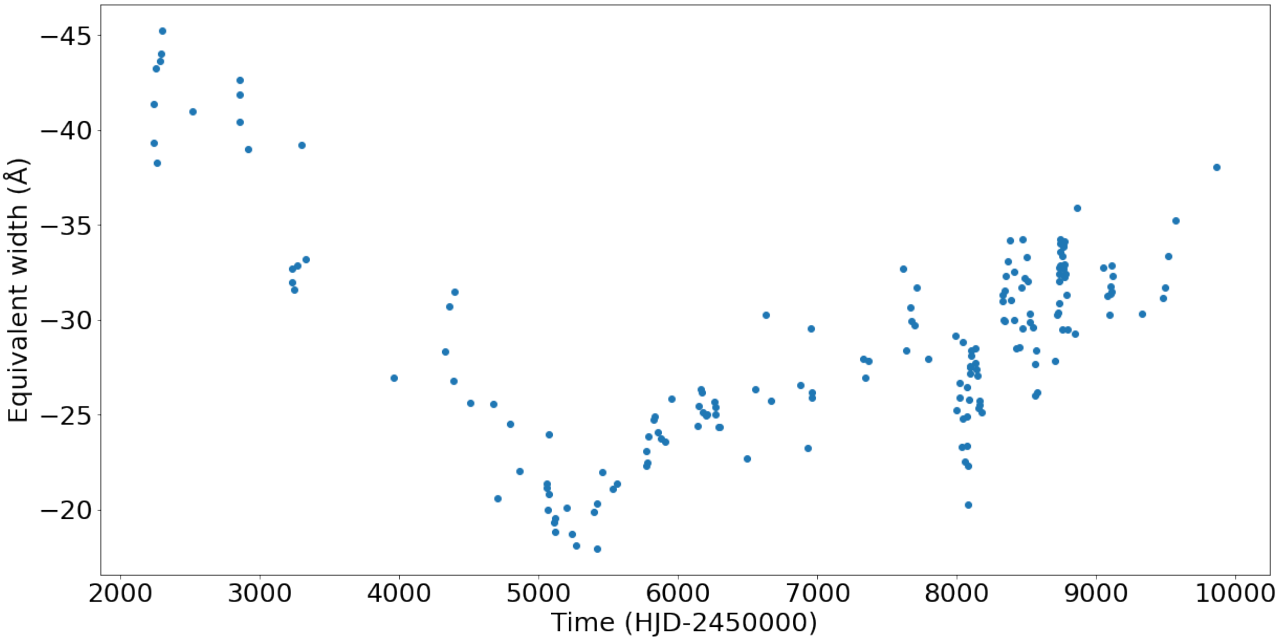

Figure 15: Equivalent width of the Hα line over time

As seen on Figure 15, the equivalent width of the Hα lines drastically varies over time: initally the emission weakens from HJD 2452000 to 2455000, before strengthening once again after 2456000, punctuated by a series of brief spikes and dips.

This result can be compared to those published in literature:

- In 2001, the Hα emission was found to have an equivalent width of -46 Å [24]. In the equivalent widths calculated above, the closest value in 2001 is of -43.2 Å on 09/12/2001 (HJD 2452253).
- Gies et al (2007) reported an equivalent width of -42.6 Å in October 2003, our closest observation yields an equivalent width of -40.0 Å on 03/10/2003 (HJD 2452915)[9].
- Mourard et al (2015) found an equivalent width of -25 Å in late-September to October 2011, closely matching the calculated equivalent width of -24.9 Å on 26/09/2011 (HJD 2458531) [24].

While the equivalent widths obtained are similar to those in the literature, they are nonetheless different. This discrepancy is likely due to differences in methodology: the choice of the interval over which the equivalent width is calculated will have an effect on its value. Furthermore, the data reduction may have an effect on the equivalent width calculation. For instance, during the continuum normalization, certain line profiles had too little continuum for a proper polynomial fit to be made without including part of the line's base. This led to part of the line's base being "cut off" once the continuum was normalized.

The equivalent width was also known to vary prior to the timespan covered by the amateur observations: Hummel and Vrancken (1995) found an equivalent width in November 1993 of -35 Å, showing that the Hα emission strengthened between 1993 and 2001 [15].

The calculated equivalent width (Figure 15) can also be directly compared with the evolution of the line profiles (Figures 12, 13 and 14, all dates in HJD-2450000):

- From the start of the observations on 2200 to 5200, the emission weakens due to an overall decrease of the line's height as well as the appearance of an absorption core on 4000 (see Figures 12a and 12b).
- After 5200, the emission begins to rapidly strengthen as the line's height begins to increase and the absorption core gradually disappears (see Figure 12c).
- After 6000, the line undergoes rapid short-term increases and decreases in height (particularly of the line's peaks), with overall result being a slow strengthening of the emission (see Figure 13a).
- After 7000, the central absorption core is once again observed but it is more than compensated by an increase of the line's height, leading to a strengthening of the emission (see Figure 13b).

- After 8000 a brief decrease of the line's height leads to a dip of the emission strength. It is followed by a rapid strengthening of the emission after 8400 due to an increase of the line's height and the loss of the central absorption (see Figures 13c and 14a).
- By 8500, a rapid decrease of the line's height strongly weakens the line before the line's height begins increasing again up until 8760 which sees a decrease of the line's height and a return of the central absorption (see Figure 14b).
- Finally, after 9000, the Hα undergoes a rapid strengthening as the central absorption disappears and the line's height increases (see Figure 14c).

It should be noted that Grundstrom and Gies (2006) found that the size of the disk scales with the equivalent width [11]. If this is the case, then the equivalent width variation shown on Figure 15 corresponds to an overall decrease of the disk size until 5200 followed by an overall increase during the rest of the timespan covered by the observations. Such variation of the disk size is not unknown in Be stars. Indeed, the disks of Be stars can grow and dissipate as the mass loss of the star increases or decreases. Most Be stars undergo irregular periods of disk growth followed by disk decay without complete loss of the disk, though extreme cases in which the disk completely dissipates or suddenly forms around a diskless B-type star are known to exist [38]. Sarbogal et al (2017) found that ϕ Per's disk is variable, having increased in optical depth between 2012 to 2014, alongside an increase of Hα emission over the same period [40] (also seen in our data). They classified the disk as quasi-stable as while it has varied it has not dissipated [40].

Finally, we can further characterise how the line profile's shape changes by investigating the the V/R variation. Inspecting the line profiles' peaks, one finds:

- Initially, in 2001, the line is double-peaked and roughly symmetric, before becoming single peaked and asymmetric towards the red on 2284 (Figure 12a).
- After 2854, the line gradually becomes triple-peaked with a red-shifted peak that is dominant (Figure 12a).
- The Hα emission continues to display triple-peaked emission after 3231, with a dominant peak in the blue-shifted side of the spectrum. The line briefly becomes double-peaked on 3244, before the third peak reappears and persists until 3330. By 3962, the line is once again double-peaked linewith a dominant red-shifted peak (Figure 12a).
- On 4706, the asymmetry of the lines disappears completely, followed by the lines becoming single peaked and strongly red-shifted on 4793 (Figure 12b).
- 4866 sees the line start off double-peaked symmetric, before the blue-shifted peak becomes dominant on 5059 (Figure 12b).
- The dominant peak shifts from blue to red on 5455 (Figure 12c).

- The line is once again triple-peaked from 6143 to 6961, with the dominant peak being red-shifted until 6628 after which it becomes blue-shifted (Figures 13a).
- From 7327, the lines remain blue-shifted but are once again double-peaked (Figures 13b).
- 7793 sees the dominant peak switch from blue to red (Figures 13c).
- The dominance of the red peak is briefly interrupted from 8142 to 8188 during which the two peaks are roughly symmetric (Figure 14a).
- The red-shifted double-peaked line persists until 8656 after which the line becomes triple-peaked with a dominant red peak for the remainder of the observing period (Figures 14b and 14c).

In order to determine if there is any periodicity to the V/R variation, we have calculated and plotted the V/R ratio for each line profile.

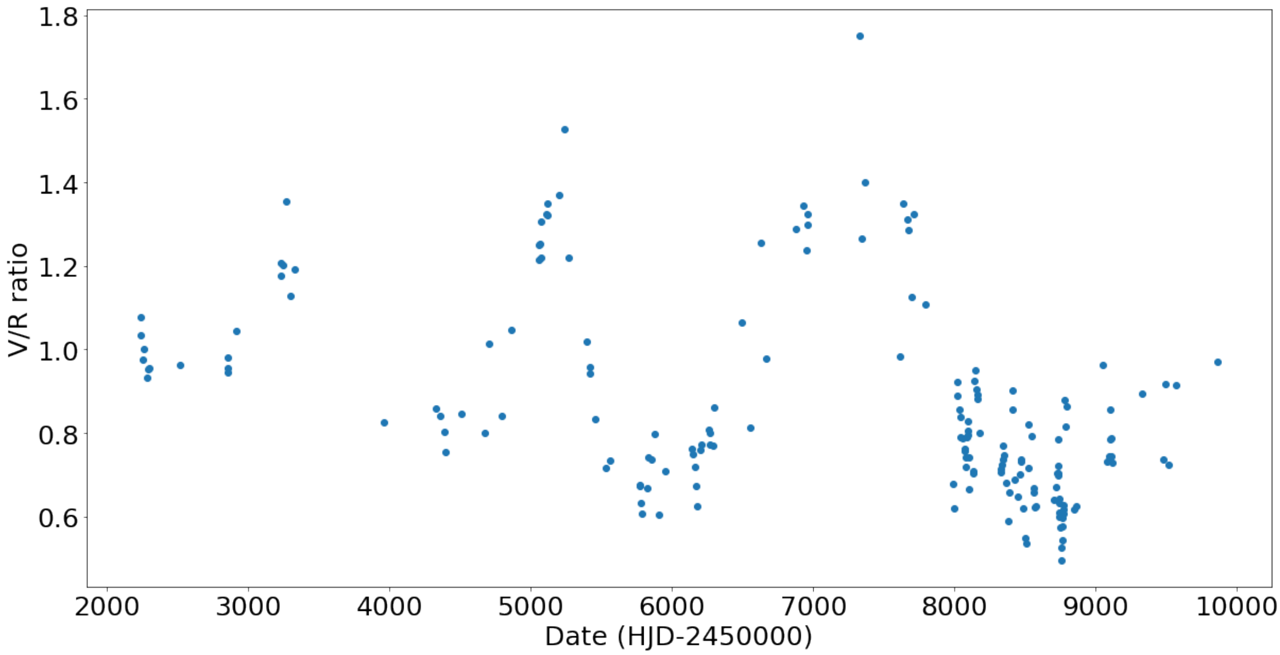

Figure 16: V/R ratio of the Hα line profiles over time

As seen on Figure 16, the V/R ratio appears to undergo long-term cyclical variations lasting roughly 2000 days, much longer than ϕ Per's period of 126.6982 days (as found by Mourard et al (2015)[24]). These correspond to a change of the dominant peak. In addition to these long-term variations there are short-term variations of the V/R ratio, most visible between the changes of the dominant peak. In order to determine whether or not these short-term variations are dependent on the orbital motion, the V/R variation was plotted as a function of the phase

(Figure 17), using the orbital solution found by Mourard et al (2015) [24] previously shown in Table 1 in Section 1.6.1.

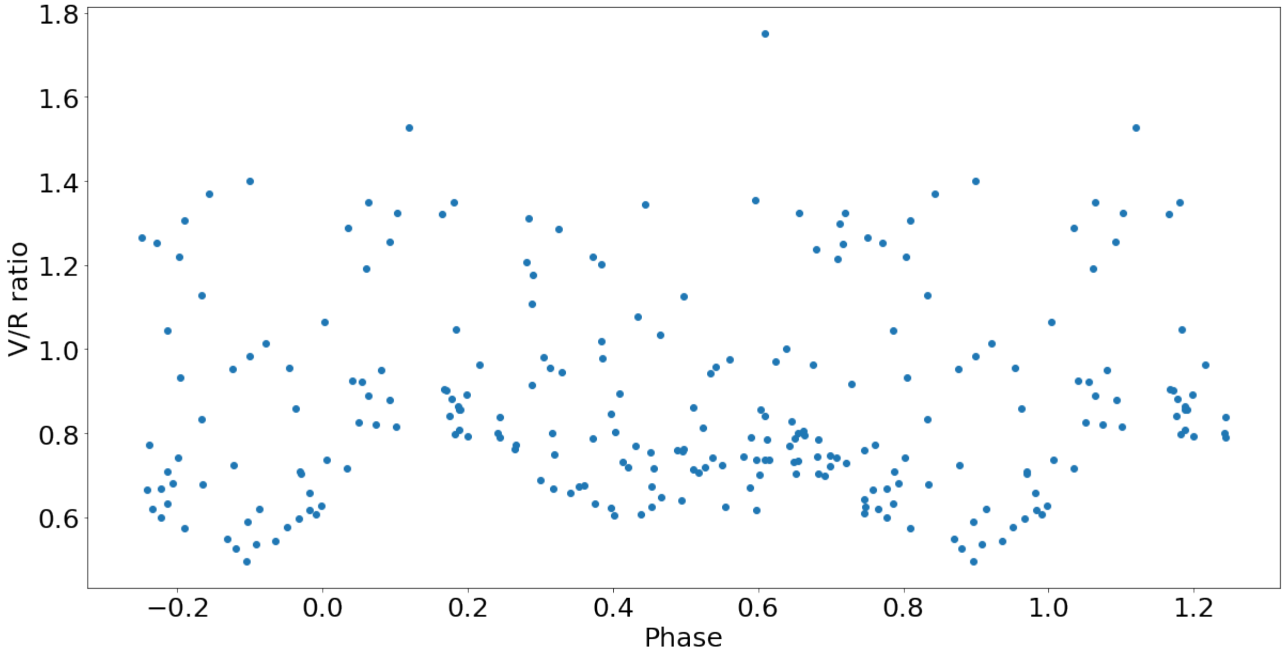

Figure 17: V/R ratio of the Hα line profiles as a function of phase

As seen on Figure 17, there appears to be a periodic variation, with minima at phases 0.4 and 0.8. However, there is a significant amount of scatter arising from the long-term variations. We will therefore restrict ourselves to a time span during which the dominant peak does not change and the line remains double-peaked, in order to verify the periodicity of the short-term V/R variation. We have chosen to use the time span from HJD 2458000 to 2458846, as the line remains consistently double-peaked with a dominance in the red, whilst having enough points to properly cover the entirety of the orbital period.

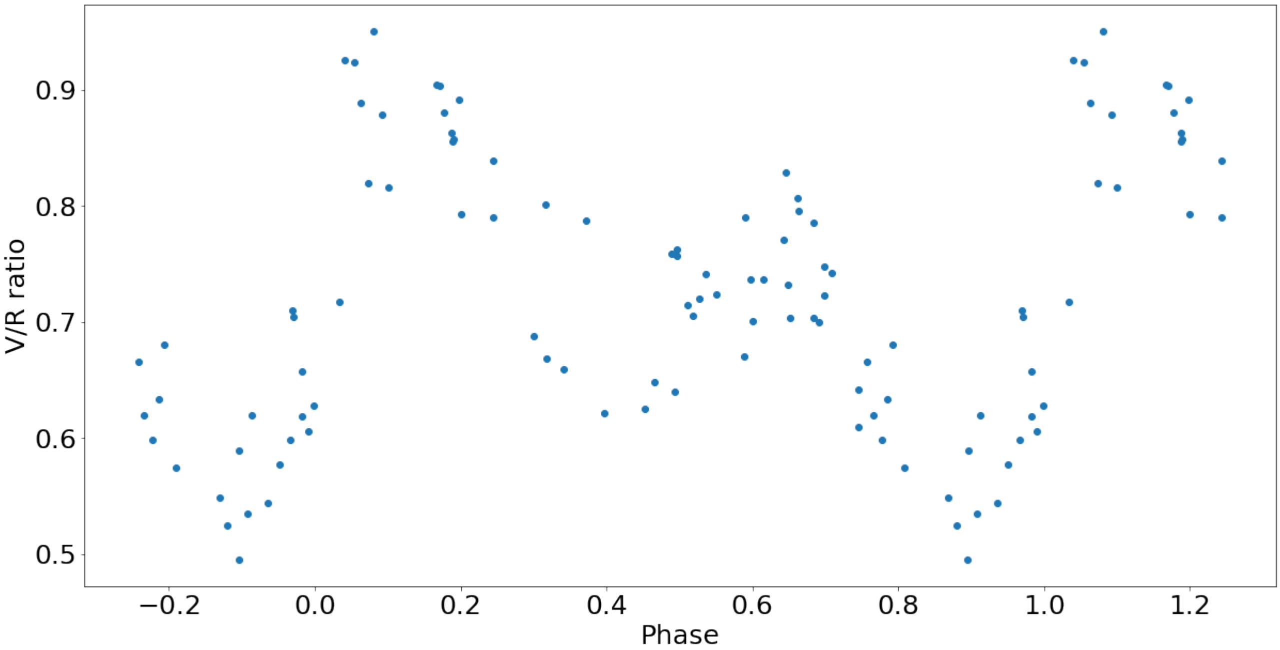

Figure 18: V/R ratio of the Hα line profiles from HJD 2458000 to 2458846 as a function of phase

The periodicity of the short-term V/R variation is clearly seen when examining it during the limited time span (see Figure 18). ϕ Per's V/R variation therefore consists of long-term (roughly 2000 days) cyclical variations alongside short-term variations linked to the orbital motion. This mixing of long-term and short-term orbital variations was also observed by Štefl et al (2007) [50].

3 Radial velocity measurement methodology

With the Hα line profiles in hand, the next step is to calculate an orbital solution from the data. This solution will then be used for the X-ray analysis. The orbital solution can be found thanks to the Doppler effect: as the sdO companion orbits around the Be primary, the primary 'wobbles' around the barycenter of the system. This causes the emission lines to be shifted, including Hα as the disk surrounds the primary star. Therefore measuring the Hα line's radial velocities provides constraints on those of the primary. This section will present two methods of measuring the radial velocities. The method used to fit the radial velocities in order to obtain the orbital solution will be covered as well.

3.1 Centroid method

One method to measure the radial velocities is to calculate the centroid of the Hα line profile.

Its centroid position can be calculated using the following formula:

$$C = \frac{\sum_{i=1}^{N} v_i \left(F_i - 1\right)}{\sum_{i=1}^{N} \left(F_i - 1\right)} \tag{5}$$

Where C is the centroid position, F_i is the normalised flux for a specific radial velocity value v_i.

It is important to note that the centroid velocity is sensitive to the disk variations and the outer regions of the disk (corresponding to the inner parts of the line profile) are known to be highly variable [26]. As such, a second method of measuring the radial velocities will be investigated as well.

3.2 Gaussian method

In order to mitigate the effect of the disk's variations on the measurement of the star's radial velocity, the measurement could be limited to the part of the disk closest to the star. In that case, the resulting radial velocity data will be less affected by any change in the outer region (i.e of the peak itself) [43]. In practice, such a method should only probe the emission wings of the profile, as their highly Doppler-shifted emissions indicate that they are emitted from the innermost regions of the disk.

One method to do this was proposed by Schneider and Young (1980)[41]. They found that the wavelength of a spectral feature can be found by convolving the spectrum with a specially defined function:

$$\int f(\Lambda)\, K(\lambda - \Lambda)\, d\Lambda = 0 \tag{6}$$

Where Λ is the wavelength (this equation can equivalently be expressed as a function of velocity), f is the spectrum, λ is a shift value and K is the special function. That function $K(x)$ is composed of two Gaussians, one inverted relative to the other (see Figure 19). Such a double Gaussian allows for the measurement of the line's position at various heights. The double Gaussian expression of $K(x)$ is given by[41]:

$$K(x) = exp\left[-\frac{(x-a)^2}{2\sigma^2}\right] - exp\left[-\frac{-(x+a)^2}{2\sigma^2}\right] \tag{7}$$

Where σ is the standard deviation of the Gaussians, a is half the separation of the Gaussians. The choice of a and σ, particularly that of a, will affect the resulting velocities.

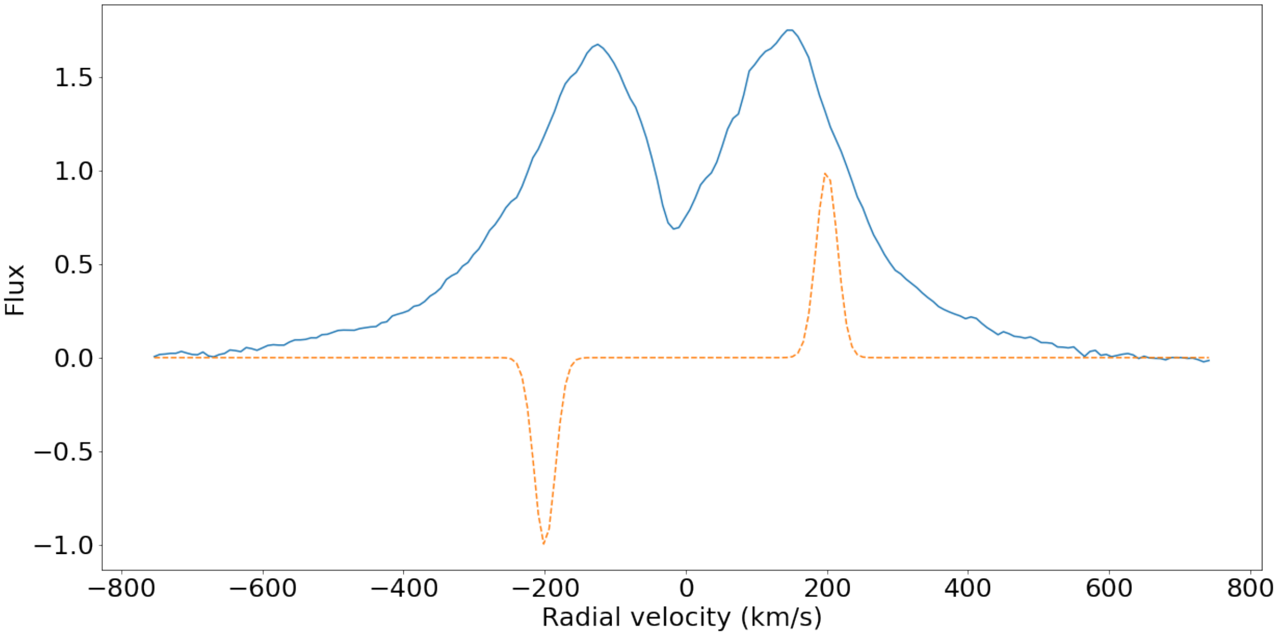

Figure 19: Comparison of the double Gaussian with $a = 200$ km/s and $\sigma = 15$ km/s (dotted line) to the line profile of HJD 2455418 (09/08/2010) which is the line with the smallest amplitude in the available data (continuous line).

If the value chosen for a is too small the Gaussians will probe the inner parts of the line profile hence the result will be affected by the variations of the outer part of the disk. Conversely, if the value of a is too large, the resulting measurements will start being affected by noise as the

Gaussians will probe parts of the profiles which blend with the continuum [44]. Intermediate values can probe the line centroid at 1/4, 1/2 or 3/4 of the profile height.

In order to solve Equation 6, it will simply be evaluated for multiple shifts (λ). The value that satisfies the equality can then be found via linear interpolation of the results.

3.3 Fitting methodology

Once the radial velocities have been obtained, they will be fitted in order to obtain an orbital solution. In a massive binary, the radial velocity variation is periodic. If the orbit is circular (as in ϕ Per):

$$y_i = \gamma + Ksin\left(\omega T_i + \phi\right) \tag{8}$$

Where

$$T_i = t_i - t_0$$

$$\omega = \frac{2\pi}{P}$$

K is the amplitude of the radial velocity variation, P is the orbital period, ϕ is a phase shift, t_0 is a reference epoch, t_i is the date (in HJD-2450000) associated to a given data point i and y_i the corresponding radial velocity. This can be rewritten as:

$$y_i = \gamma + Asin\left(\omega T_i\right) + Bcos\left(\omega T_i\right) \tag{9}$$

This form has the advantage of being linear with respect to the three unknowns. They can be found from the measured radial velocities using a chi-squared minimisation:

$$\chi^2 = \sum_{i=1}^{N} \frac{\left(RV_i - y_i\right)^2}{\sigma_i^2} \tag{10}$$

Where RV_i are the measured radial velocities and σ_i their associated uncertainties. In cases where the uncertainties σ_i of the measured radial velocities are not known (such as in our case, as will be detailed below) the σ_i can simply be set to 1. Values for all three parameters are thus found by solving:

$$\frac{\partial \chi^2}{\partial \gamma} = 0 \tag{11}$$

And its equivalents for A and B. In our case this corresponds to the following matrix equation:

$$\begin{pmatrix} \sum \frac{1}{\sigma_i^2} & \sum \frac{sin(\omega T_i)}{\sigma_i^2} & \sum \frac{cos(\omega T_i)}{\sigma_i^2} \\ \sum \frac{sin(\omega T_i)}{\sigma_i^2} & \sum \frac{sin(\omega T_i)^2}{\sigma_i^2} & \sum \frac{sin(\omega T_i)cos(\omega T_i)}{\sigma_i^2} \\ \sum \frac{cos(\omega T_i)}{\sigma_i^2} & \sum \frac{sin(\omega T_i)cos(\omega T_i)}{\sigma_i^2} & \sum \frac{cos(\omega T_i)^2}{\sigma_i^2} \end{pmatrix} \begin{pmatrix} \gamma \\ A \\ B \end{pmatrix} = \begin{pmatrix} \sum \frac{RV_i}{\sigma_i^2} \\ \sum \frac{RV_i sin(\omega T_i)}{\sigma_i^2} \\ \sum \frac{RV_i cos(\omega T_i)}{\sigma_i^2} \end{pmatrix} \tag{12}$$

In order to solve this matrix equation, the 3x3 matrix is inverted. Calculating the uncertainty on the fitting parameters is normally done using the error propagation formula (where x is a given fitting parameter):

$$\sigma_x^2 = \sum_{i=1}^{N} \sigma_i^2 \left(\frac{\partial x}{\partial RV_i} \right)^2 \tag{13}$$

However, when the uncertainty σ_i is not known, the uncertainty on the fitting parameters obtained via the error propagation formula (Equation 13) will be multiplied by the root-mean-square deviation of the fit, given by the square root of the χ^2 value divided by the degrees of freedom:

$$\sqrt{\frac{\chi^2}{N-D}} \tag{14}$$

Where D is the number of fitting parameters, in our case 3.

Once the fit parameters are found, the next step is to obtain the amplitude and phase shift of the fitting curve. The amplitude i found by applying the Pythagorean theorem to A and B . The phase shift ϕ can be found by equalizing the two expressions of the fitting curve (Equations 8 and 9) as well as by using the sine addition formula on Equation 8:

$$\gamma + K_sin\left(\omega T_i + \phi\right) = \gamma + Asin\left(\omega T_i\right) + Bcos\left(\omega T_i\right) \tag{15}$$

$$\Leftrightarrow \gamma + Ksin\left(\omega T_i + \phi\right) = \gamma + sin\left(\omega T_i\right) cos\left(\phi\right) + cos\left(\omega T_i\right) sin\left(\phi\right) \tag{16}$$

$$\Leftrightarrow Asin\left(\omega T_i\right) + Bcos\left(\omega T_i\right) = sin\left(\omega T_i\right) cos\left(\phi\right) + cos\left(\omega T_i\right) sin\left(\phi\right) \tag{17}$$

$$\Leftrightarrow \frac{B}{A} = \frac{sin\left(\phi\right)}{cos\left(\phi\right)} = tan\left(\phi\right) \tag{18}$$

$$K = \sqrt{A^2 + B^2} \tag{19}$$

With the phase shift now in hand, a new value for the epoch t_0^n can be calculated from ω and from t_0 the initial reference epoch:

$$\omega\left(t_i - t_0\right) + \phi = \omega\left(t_i - t_0^n\right) \tag{20}$$

$$t_0^n = t_0 - \frac{\phi}{\omega} \tag{21}$$

In our case, we have fitted the radial velocities without error values. While we could have estimated the uncertainties from the continuum noise, the quality of the amateur astronomer's calibration of the data is not known. Therefore such an estimation may be insufficient. It is important to note however that our choice to not estimate the radial velocity error will make the orbital solution more susceptible to the effect of line profile variations. Once an orbital solution is calculated an estimation of the radial velocity error can be obtained in the form of the RMS deviation (Equation 14). While this is not ideal as the RMS error will be identical for each data point regardless of the spectrum it is measured from, it will nonetheless be used as it provides a global insight on the data's deviation from our fitting model.

4 Radial velocity results

4.1 Centroid radial velocity result

The first attempt at measuring the radial velocities was carried out using the centroid method, the results of which are shown on figure 20.

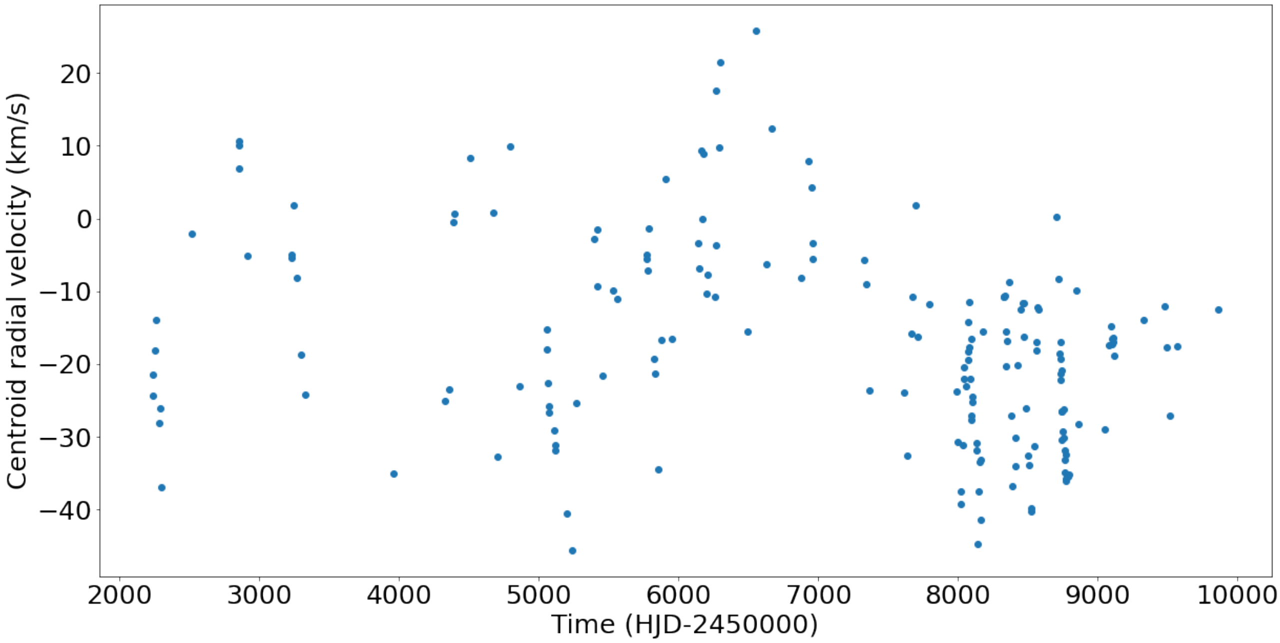

Figure 20: Change of the centroid radial velocity with time

The calculated centroid values are then expressed in terms of the orbital phase using the ephemeris from Mourard et al (2015)[24]: orbital period of 126.6982 ± 0.0035 days with a reference date for the ephemeris of HJD 24561110.03 ± 0.08, defined as the date in which the radial velocity was at its minimum (Figure 21).

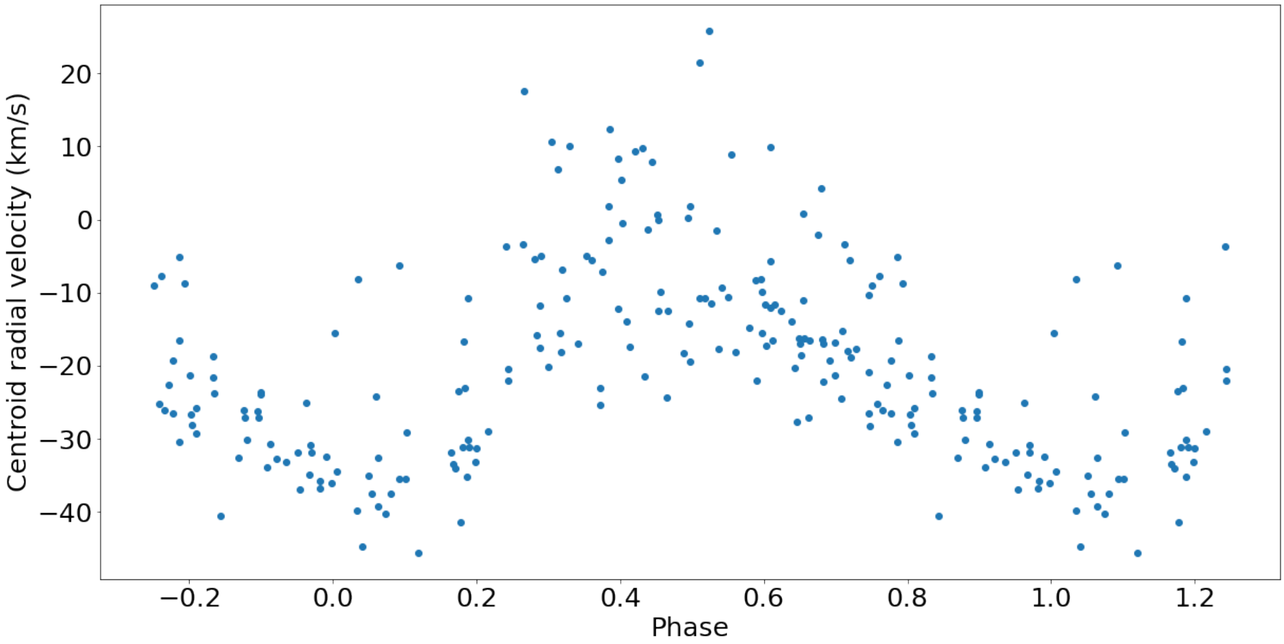

Figure 21: Centroid velocity as a function of phase.

As seen on Figure 21, the overall variation of the centroid velocities very clearly follows the orbital solution of Mourard et al (2015) [24]: the calculated centroid velocity minimum and maximum are close to the expected minimum and maximum phases. However, there is a large dispersion. A possible cause is that the centroid velocity is sensitive to the full profile, hence to the disk variations and the outer regions of the disk (corresponding to the inner parts of the line profile) are known to be highly variable [26].The outer disk variations in particular will strongly affect the centroid velocity as it depends on the normalized flux, with the inner parts of the line profile having the highest flux.

4.2 Gaussian method and initial fitting results

The radial velocity measurements were carried out by evaluating Equation 6 (Section 3) from -100 km/s to 100km/s to cover the -40 km/s to 20 km/s variation obtained using the centroid method (Figure 21) whilst allowing for the measurement of any radial velocities of the primary outside of this interval. These radial velocities were used for the fitting process. The initial epoch and the period used for the following fits will be fixed to Mourard et al's (2015) values of HJD 2456110.03 and 126.6982 days, respectively.

Since the radial velocities measured with the Gaussian method strongly depend on the chosen parameters a and σ, choosing the parameters used for the orbital solution is delicate. We have tested separations of 200, 250 and 300 km/s with σ = 15 km/s. These separations

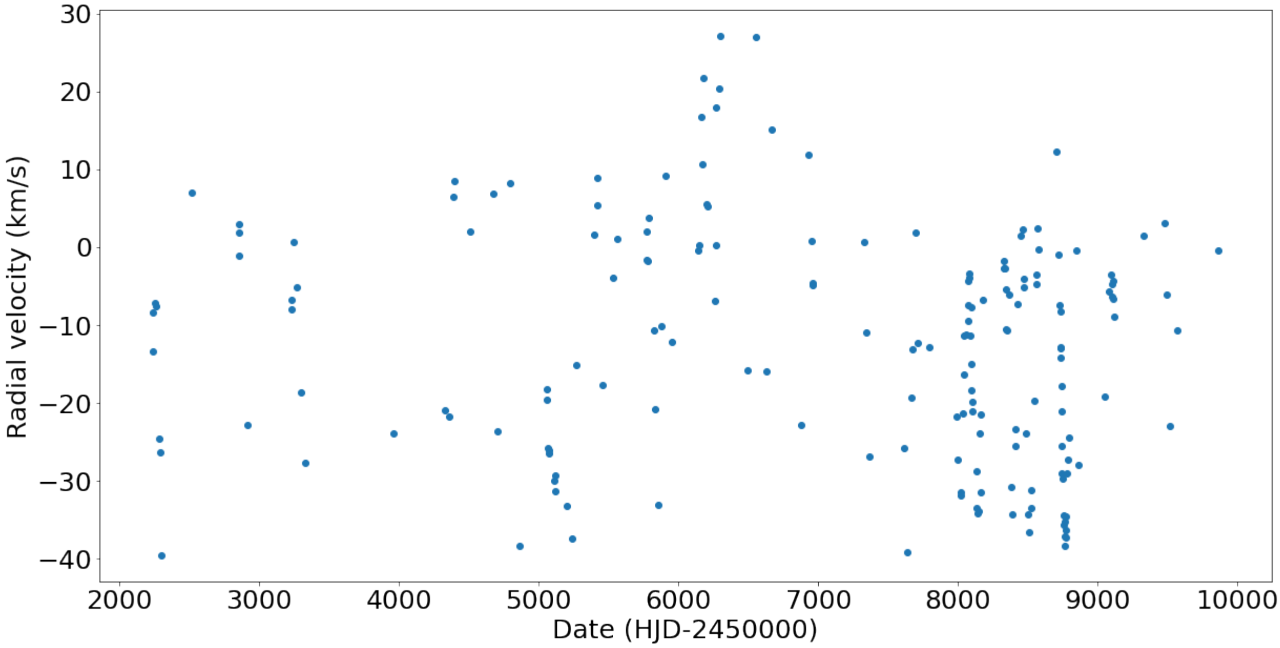

Figure 22: Gaussian radial velocities as a function of time.

correspond to $\frac{3}{4}$, $\frac{1}{2}$ and $\frac{1}{4}$ of the line's height respectively. We found that the root mean-square deviation of the fit obtained increases with the Gaussian separation, with deviations of 8.2, 12.8 and 17.3 km/s for a = 200 km/s, 250 km/s and 300. As a = 200 km/s presents the lowest RMS deviation, we have chosen to use it for our initial orbital solution. The radial velocities obtained for with these parameters are listed in Appendix A along with all other radial velocities obtained from the line profiles hereafter. The radial velocities are shown as a function of time on Figure 22.

The orbital solution obtained with these Gaussian parameters (hereafter Fit 1) is shown on Figures 23. The epoch corresponds to the minimum radial velocity of the primary. This convention is the same as used in Mourard et al's (2015) orbital solution [24]. The error bars in this figure and for all subsequent fits using the line profile data corresponds to the calculated RMS deviation.

Fitting parameters	
	Fit 1
γ (km/s)	-14.3 ± 0.6
A (km/s)	1.8 ± 0.9
B (km/s)	-18.4 ± 0.9
Phase shift (rad)	-1.47 ± 0.05
Amplitude (km/s)	18.5 ± 0.9
New epoch (HJD-2450000)	6108.1 ± 0.9
RMS deviation (km/s)	8.2

Table 5: Fit parameters obtained using all amateur line profiles, with $a = 200$ km/s and $\sigma = 15$ km/s

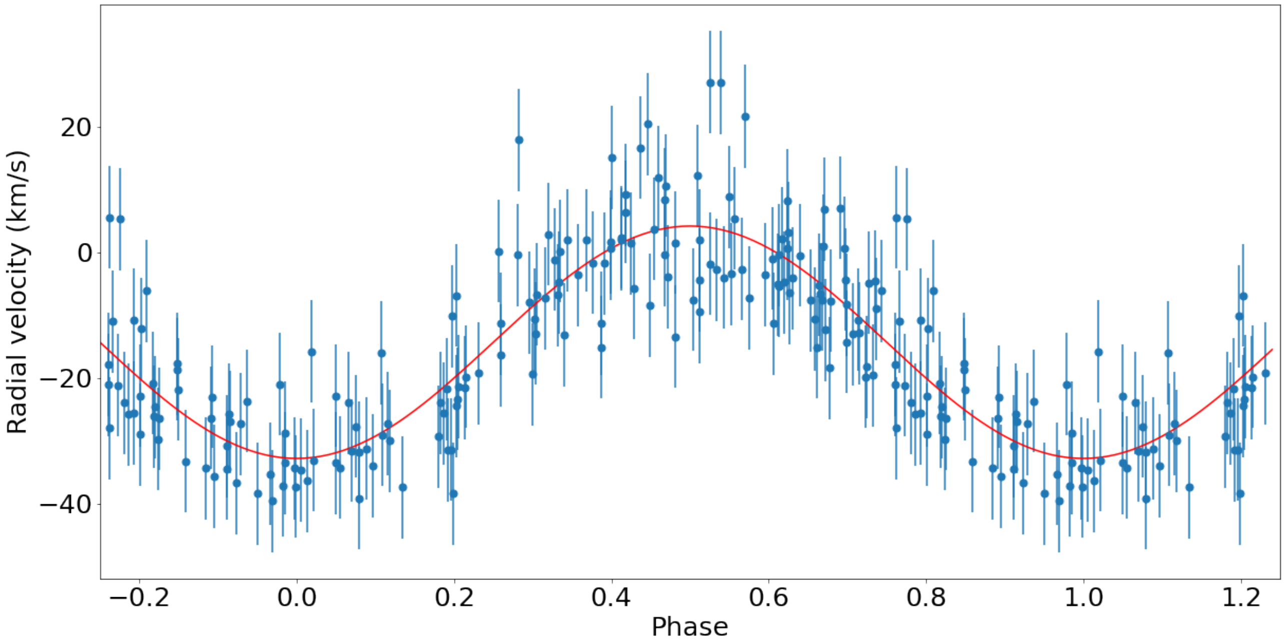

Figure 23: Radial velocity measurements and fitting curve (Fit 1A) as a function of phase, with phase 0 corresponding to the new epoch

This orbital solution can be compared to the one previously obtained by Mourard et al (2015). Their orbital solution was obtained from Hα measurements as well as additional radial velocity measurements from Gies et al (1998)[10][24]. These additional radial velocities were measured on UV spectra taken with the Goddard High Resolution Spectrograph onboard the HST. A full comparison of our orbital solutions and theirs [24] is given below in table 6:

Fitting comparison		
	Fit 1	Mourard et al (2015)
K (km/s)	18.5 ± 0.9	10.2 ± 1.0
γ (km/s)	-14.3 ± 0.6	-2.2 ±0.5
T_0 (HJD-2450000)	6108.1 ± 0.9	6110.03 ± 0.08
No. of data points	178	85
RMS deviation (km/s)	8.2	8.5

Table 6: Comparison of the results of the fit obtained using the amateur line profiles and Mourard et al's results (2015) [24]. K is the amplitude of the orbital motion, γ is the systemic radial velocity and T_0 is the epoch defined as the radial velocity minimum.

A visual comparison of our result and theirs is shown on Figure 24.

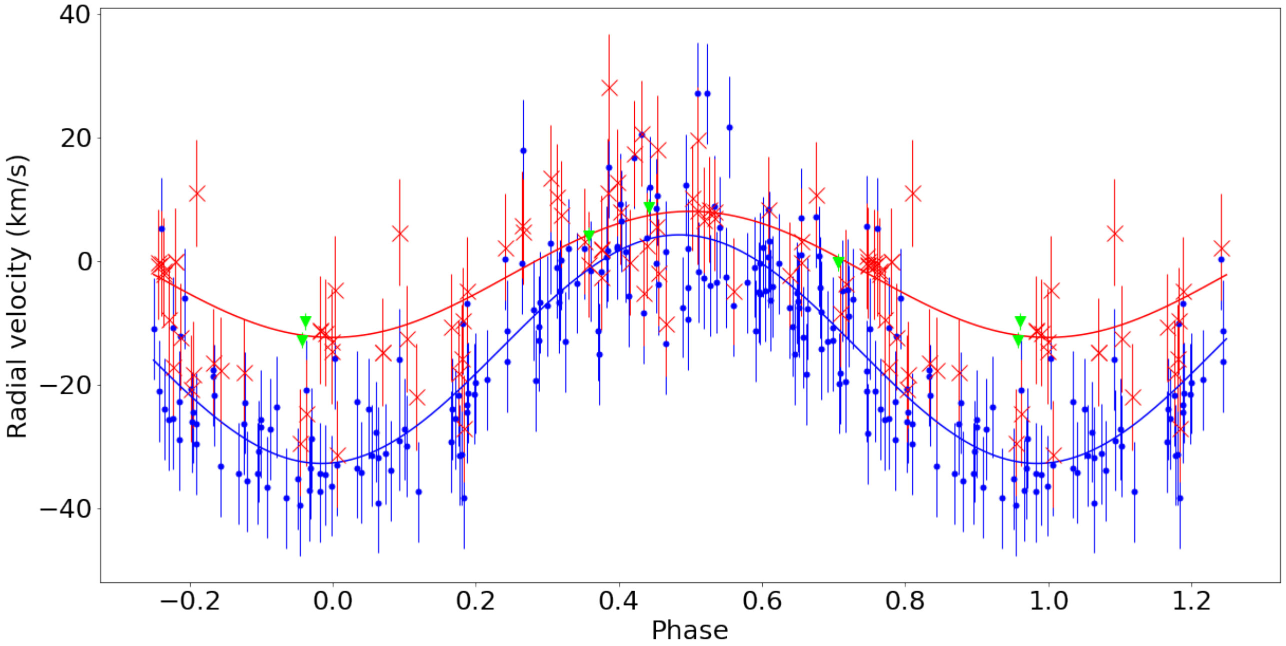

Figure 24: Comparison between Fit 1A (blue dots) and Mourard et al's results (2015) (red X for the Hα data, green triangles for the UV data). Phases defined using Mourard et al's epoch (2015) [24].

While our data points and Mourard et al's points (2015) are relatively overlapping for all three values of a, our best-fit curve is incompatible (Table 6). The Fit 1 amplitude is 6.2σ from Mourard et al's amplitude (2015)[24], the systemic radial velocity displays a difference of 15.2σ and the difference between the two epochs is comparatively small, at 2.1σ. It is unlikely that the this discrepancy arises from a mistake on Mourard et al's part(2015) as their orbital solution matches earlier ones such as one by Gies et al (1998) [24][10]. In order to ensure that these discrepancies do not arise from a problem in our methodology, an attempt was made to replicate Mourard et al's results (2015) using their data (including their errors) and our fitting implementation. The results of this replica fit (hereafter Fit M) are shown in table 7. Fit M's results are very close to Mourard et al's (2015), with a difference below 2σ for the amplitude, epoch and systemic velocity.

Fitting comparison		
	Fit M	Mourard et al (2015)
K (km/s)	10.4 ± 0.7	10.2 ± 1.0
γ (km/s)	-2.2 ± 0.5	-2.2 ±0.5
T_0 (HJD-2450000)	6108.6 ± 1.4	6110.03 ± 0.08
No. of data points	85	85
RMS deviation (km/s)	8.4	8.5

Table 7: Comparison of the results of Fit M and Mourard et al's results (2015) [24]

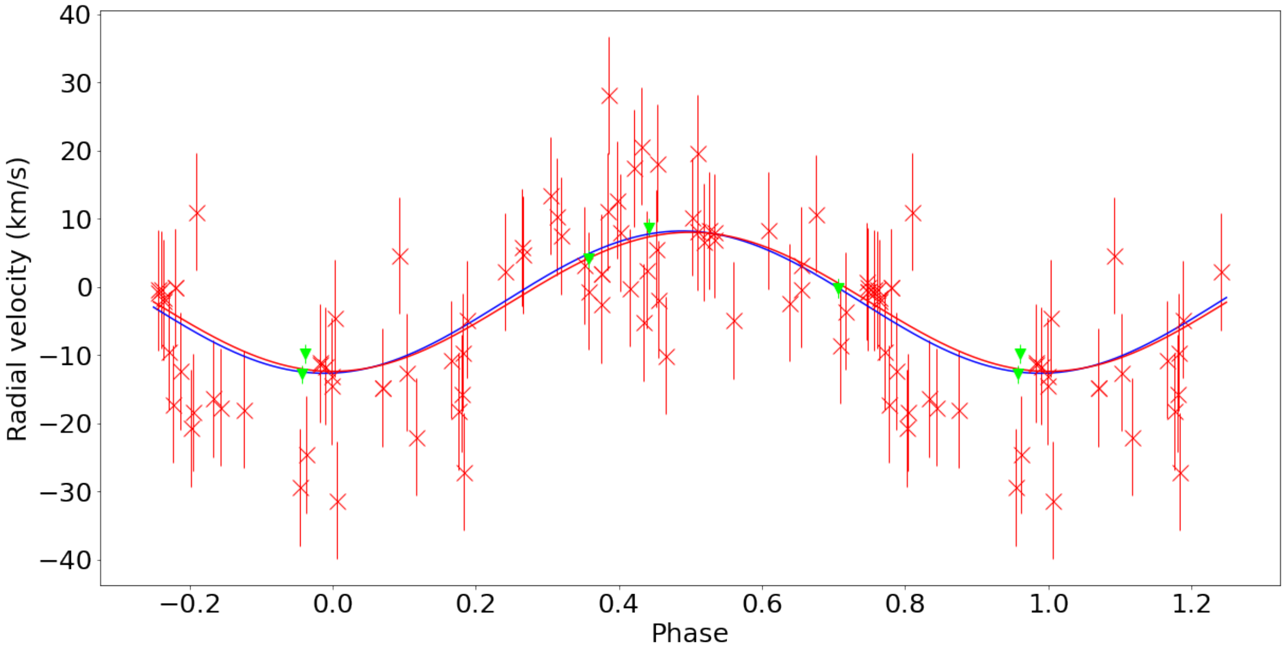

Figure 25: Comparison of the results of Fit M (blue) and Mourard et al's results (2015) [24] (red and green)

It should be noted that the amateur line profiles and Mourard et al's (2015) do not cover the same time span, which could create a discrepancy. In order to verify this, a second fit was carried out (hereafter Fit 2, Table 8 and Figure 26) using Mourard et al's (2015) parameters (a = 250 km/s) for the Gaussians and limiting the data to points within the time span covered by their paper (i.e. HJD 2450023.6 to HJD 2456665.6) [24]. The amplitudes are separated by 2.1σ. The difference between the two systemic radial velocities is still very high, at 6.8σ and the epochs' is now 2.0σ.

Fitting comparison		
	Fit 2	Mourard et al (2015)
K (km/s)	14.7 ± 1.8	10.2 ± 1.0
γ (km/s)	-11.3 ± 1.2	-2.2 ±0.5
T_0 (HJD-2450000)	6105.3 ± 2.3	6110.03 ± 0.08
No. of data points	71	85
RMS deviation (km/s)	10.2	8.5

Table 8: Comparison of the results of Fit 2 and Mourard et al's results (2015) [24] (red and violet).

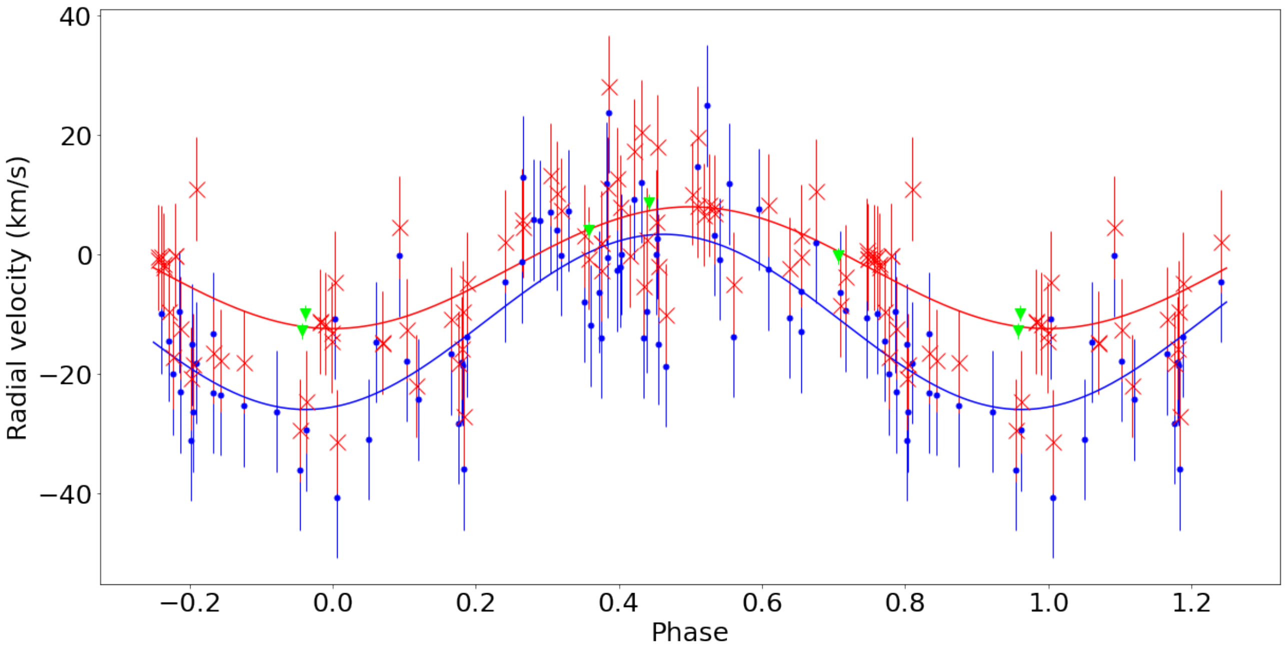

Figure 26: Comparison between the results of Fit 2 and Mourard et al's results (2015)[24] (red and green).

As previously explained, Mourard et al (2015) used radial velocity measurements from Gies et al (1998) in addition to their own measurements [10][24]. These UV radial velocities have much lower uncertainties (1.35 km/s) than those of the $H\alpha$ data (8.6 km/s) (see Figures 24 and 26. The large difference in uncertainties may have skewed the fitting towards these UV points. To investigate this, two fits will be carried out using Mourard et al's data (2015), one fitting the uncertainties of the Gies et al (1998) data to that of the Hα values (hereafter Fit UV) and one without the additional points (Fit H).

Fitting comparison				
	Fit 2	Mourard et al (2015)	Fit H	Fit UV
K (km/s)	14.7 ± 1.8	10.2 ± 1.0	12.8 ± 1.4	12.6 ± 1.4
γ (km/s)	-11.3 ± 1.2	-2.2 ±0.5	-3.7 ± 1.0	-3.6 ± 1.0
T_0 (HJD-2450000)	6105.3 ± 2.3	6110.03 ± 0.08	6108.4 ± 2.1	6108.5 ± 2.1
No. of data points	71	85	79	85
RMS deviation (km/s)	10.2	8.5	8.4	8.2

Table 9: Comparison of the results Fit 2, Mourard et al's results (2015), Fit H and Fit UV

The results of the two new fits on Mourard et al's data (2015) are shown in table 9 as well as on Figures 27 and 29. The amplitude, epoch and systemic radial velocity of the new fits are less than 2σ from Mourard et al's (2015) [24] original fit. When compared to the Fit 2, one finds Fit 2 to be closer to Fit UV and Fit H than to Mourard et al's result (2015): both new fits are 0.8σ, 0.9σ and 4.9σ from Fit 2 for the amplitude, epoch and systemic radial velocity respectively (see Figures 30 and 28). The smaller difference between Fit 2 and both Fit H and Fit UV (compared to Fit 2 and Mourard et al's result (2015)) indicates that the smaller uncertainties of the UV data are at partly responsible for the discrepancy between Fit 2 and Mourard et al's data. However as the difference in systemic velocities remains large, it is likely not the sole cause of the discrepancy. In order to obtain a proper orbital solution in line with what is known of the system's orbit, we will next investigate the likely culprit: the line profile variation.

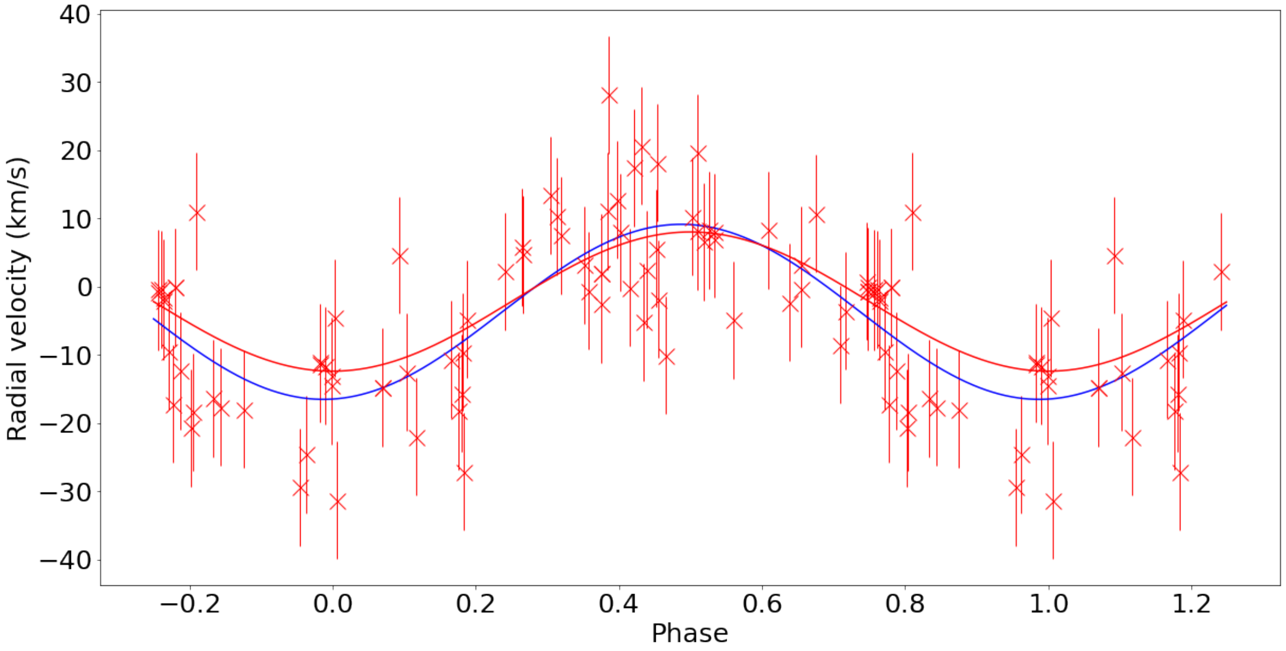

Figure 27: Comparison between the results of the Fit H (blue) and Mourard et al's results (2015)[24] (red).

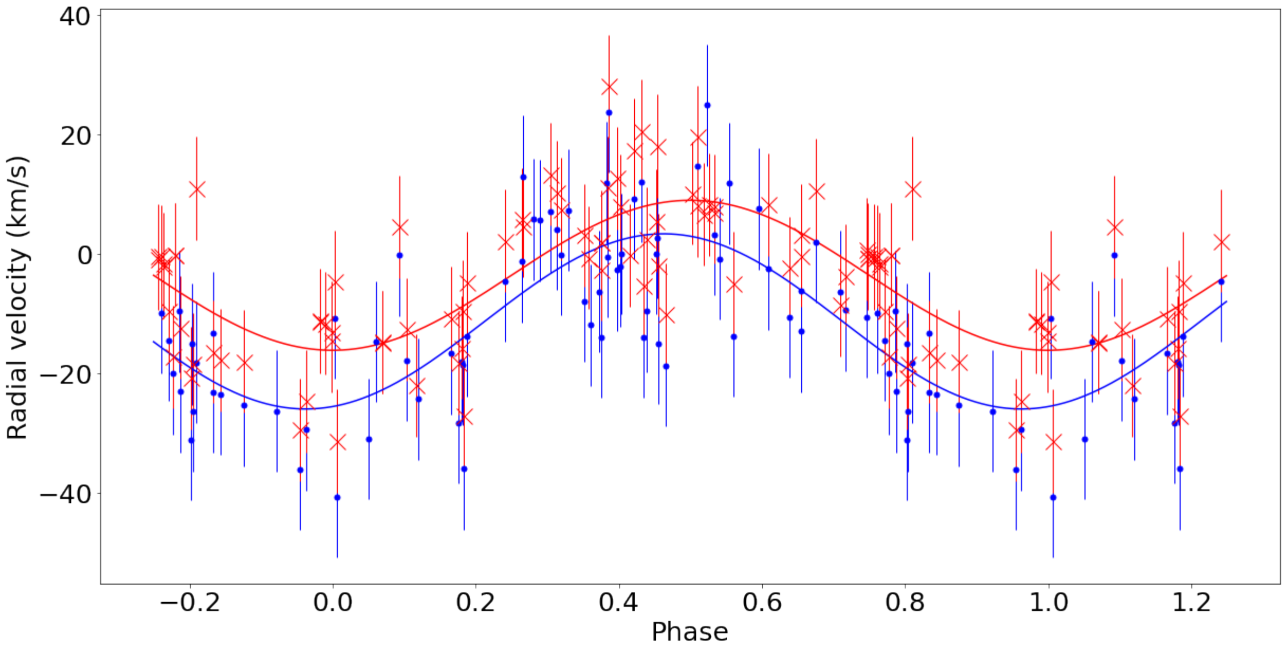

Figure 28: Comparison between the results of the Fit H (red) and Fit 2 (blue).

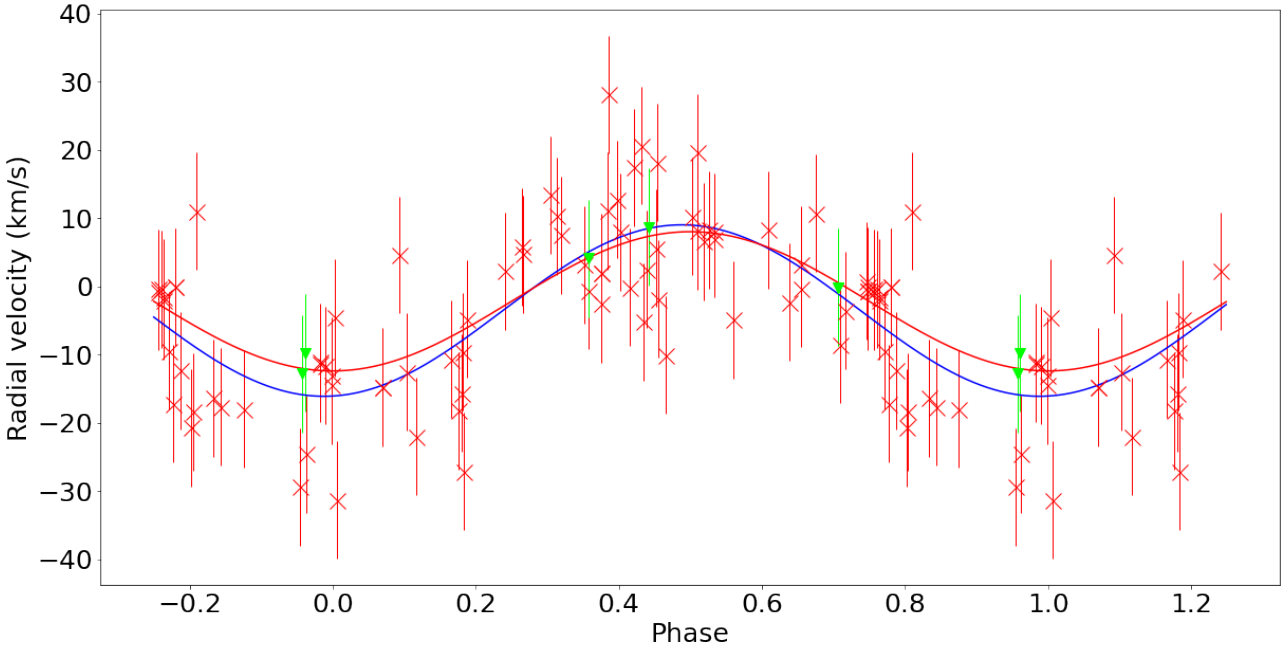

Figure 29: Comparison between the results of the Fit UV (blue) and Mourard et al's results (2015)[24] (red).

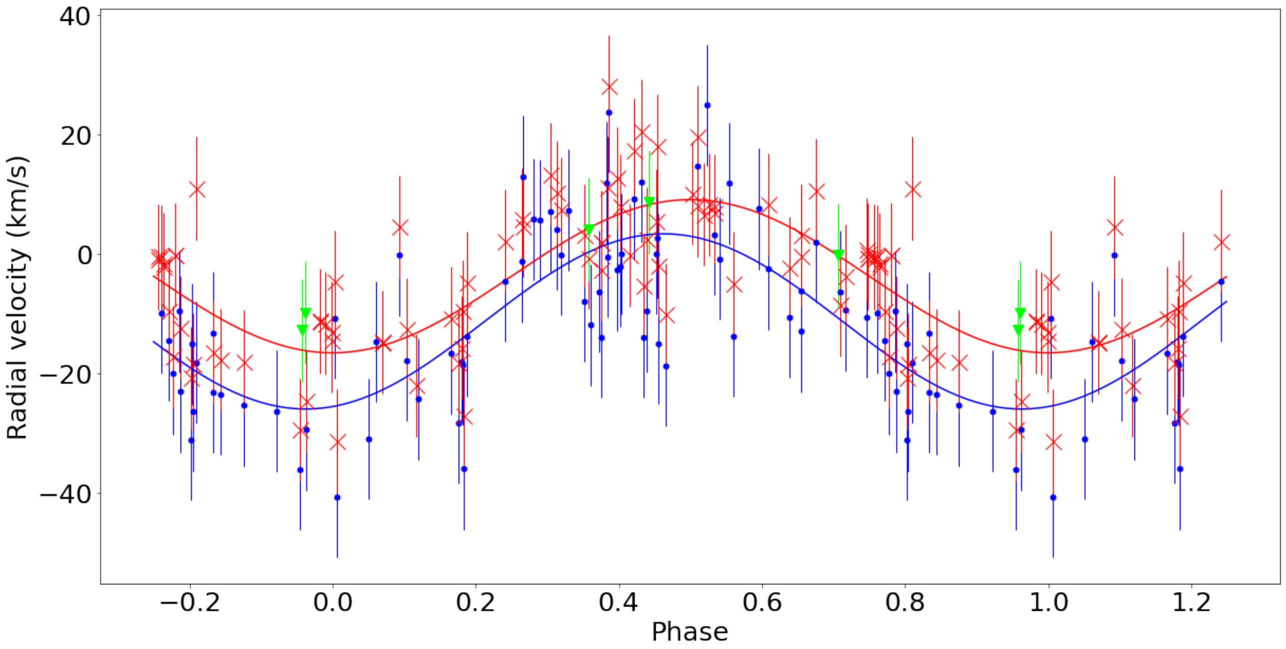

Figure 30: Comparison between the results of the Fit UV (red and green) and Fit 2 (blue).

4.2.1 Line profile variations and improving the fit results

In view of the large dispersion and since the physical characteristics of the orbit (K, γ) should not change, one needs to investigate whether the difference stems from the line profile variations. While the use of Gaussian method mitigates the effect of variations in the outer disk, the inner disk may still undergo variations. Furthermore, the choice of the Gaussian separation and width may modify the impact of the line profile variations on the radial velocity measurement.

In order to properly understand the impact of these line profile variations on the radial velocity measurement, we will investigate how they affects the scatter of the data. We will first look at the impact of the dominant peak of the line profile.

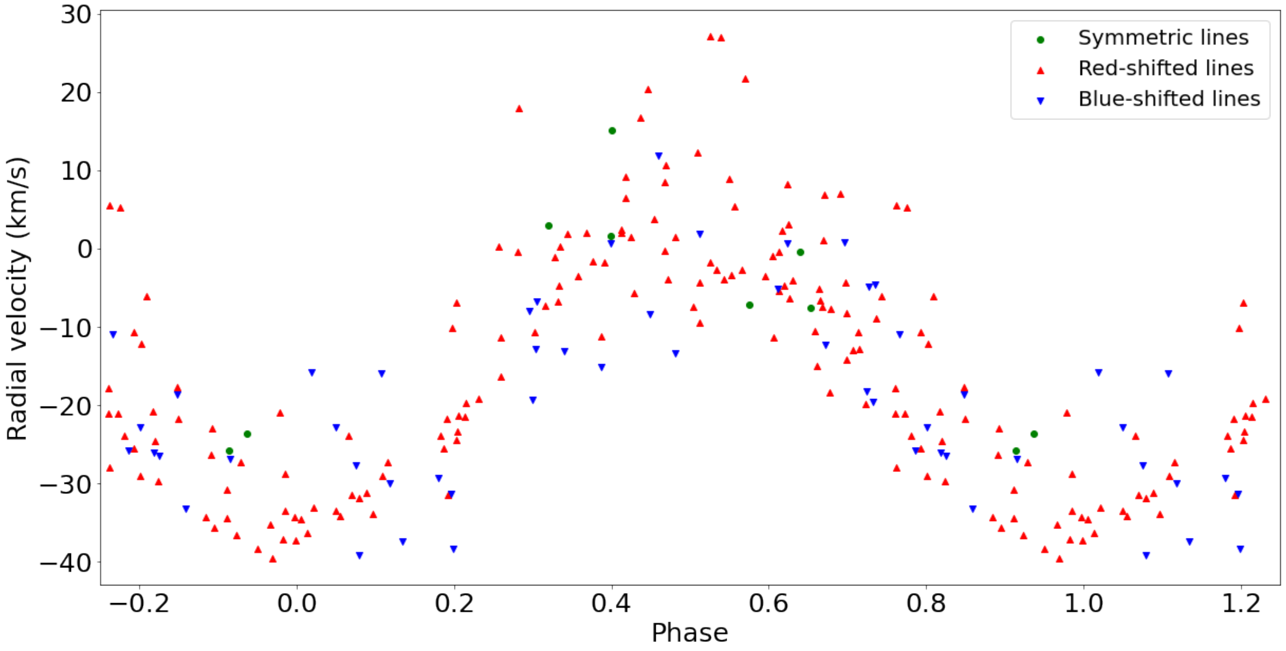

Figure 31: Radial velocity by phase (a = 200 km/s) categorizing the line profiles. Line profiles are considered symmetric if they have V/R ratios above 0.97 but below 1.03.

Figure 31 does not reveal any clear pattern for the radial velocities in relation to their dominant peaks when taking a = 200 km/s. We will therefore increase the separation to 250 km/s.

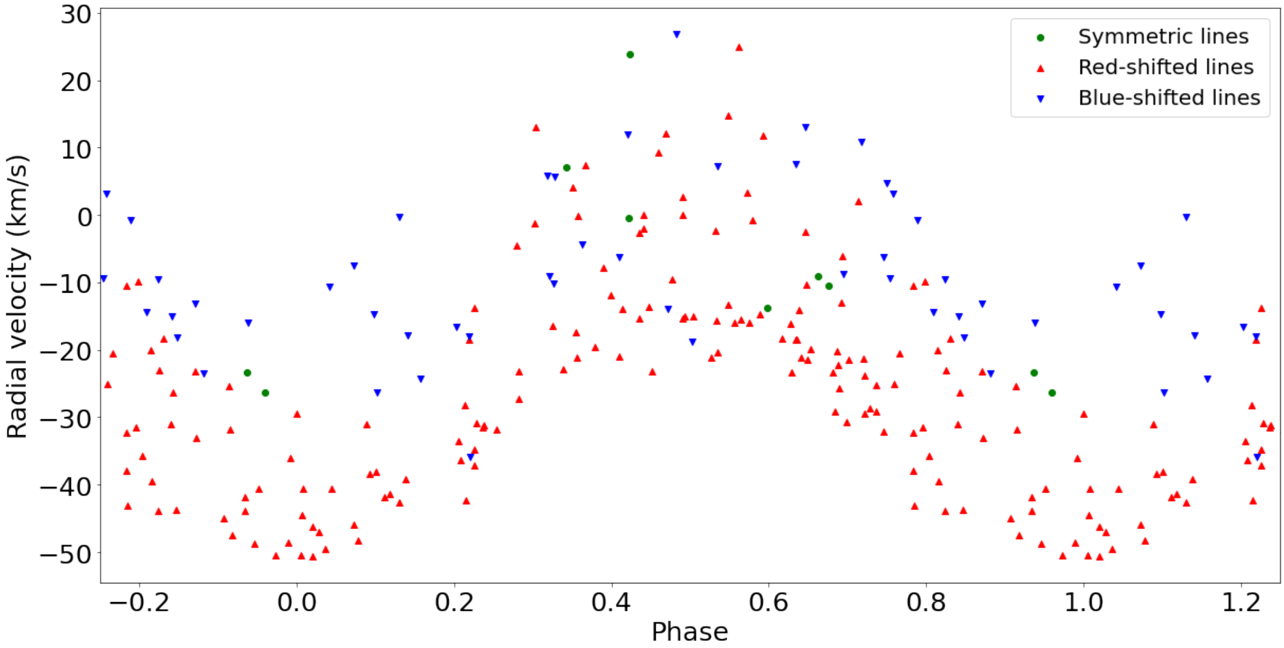

Figure 32: Idem for $a = 250$ km/s

Increasing the Gaussian separation, one finds a clearer pattern to the radial velocities (Figure 32): the radial velocities measured for the blue dominated lines are higher than most of those of the red dominated lines. Since we have chosen the convention that the radial velocities are positive when oriented away from the observer, the higher velocities measured for the blue-dominated lines would indicate an overall redward shift of the line profile. Conversely, the lower velocities of the red-dominated line profiles indicate their blueward shift. This opposite shift relative to the dominant peak has been observed in the past for other Be stars [28].

However, the blue-dominated lines are not the only lines to have shifted radial velocities: while the bulk of the radial velocities from red-dominated lines have velocities between -50 and -10 km/s (Figure 33), others are shifted outside this region. We will therefore investigate the data points that are shifted relative to this bulk region which cannot simply be attributed to blue-dominated double peaked lines. We will investigate the shifted data year by year. Figures 34 to 37 highlight the radial velocities of each year, maintaining $a = 250$ km/s.

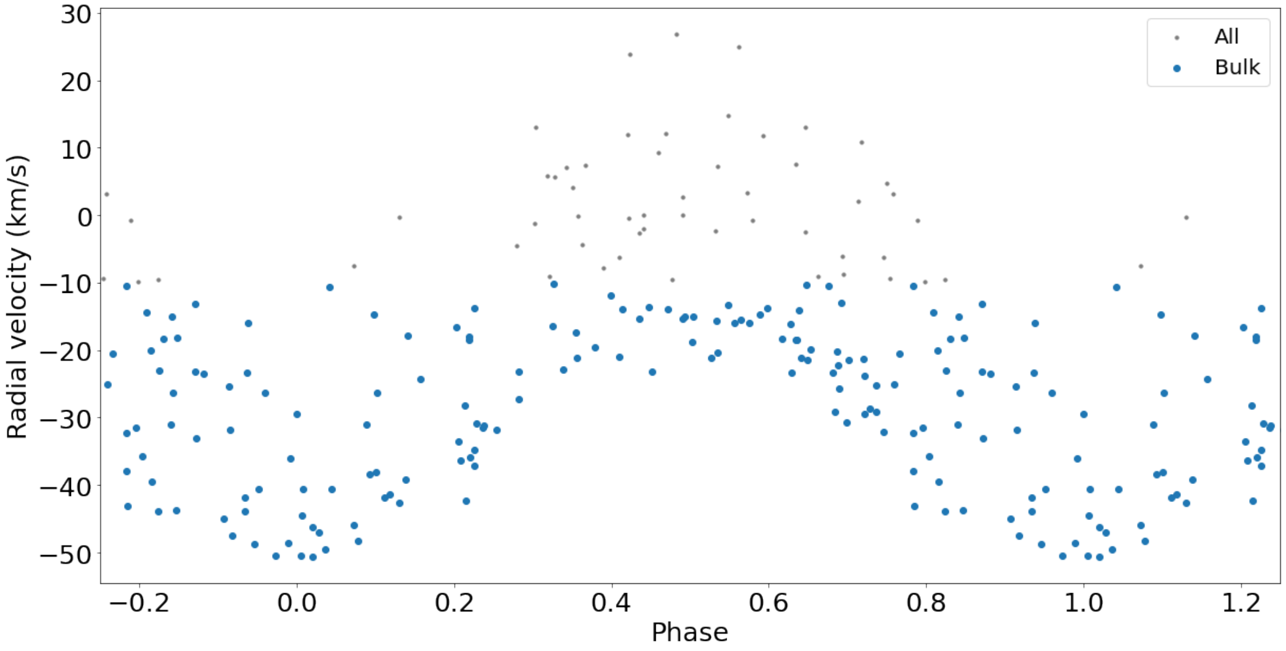

Figure 33: Radial velocity by phase highlighting the bulk of the data.

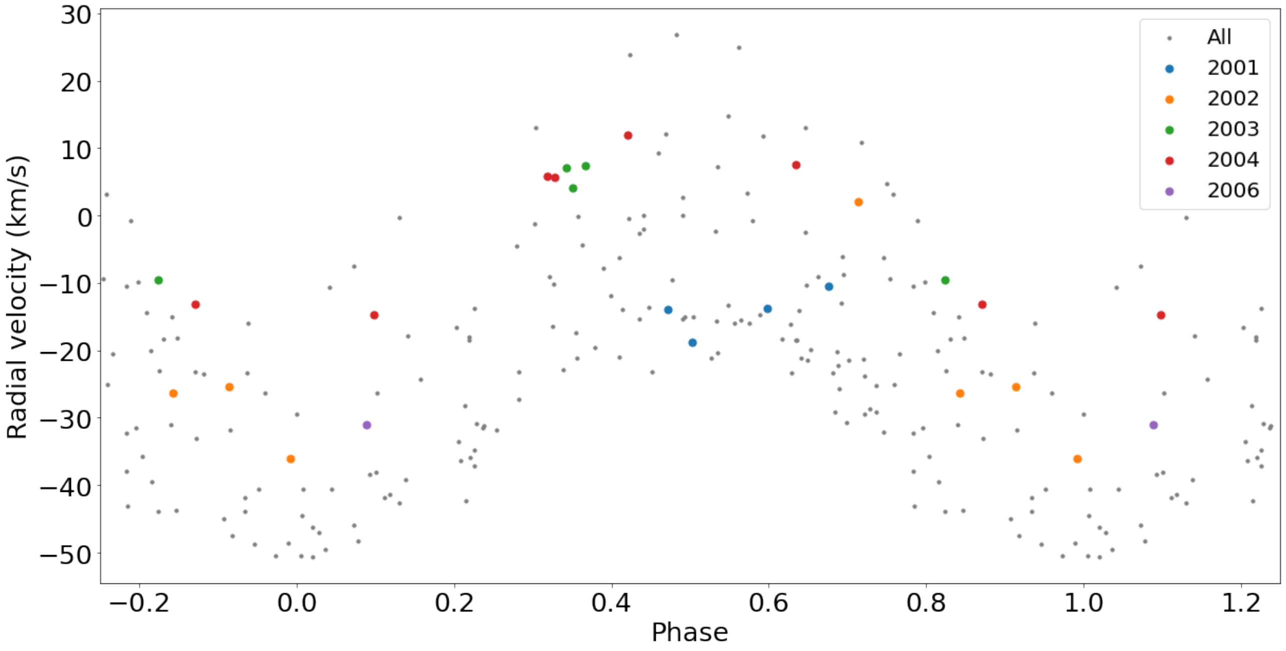

Figure 34: Radial velocity of the centroid as a function of phase highlighting the years 2001 to 2006.

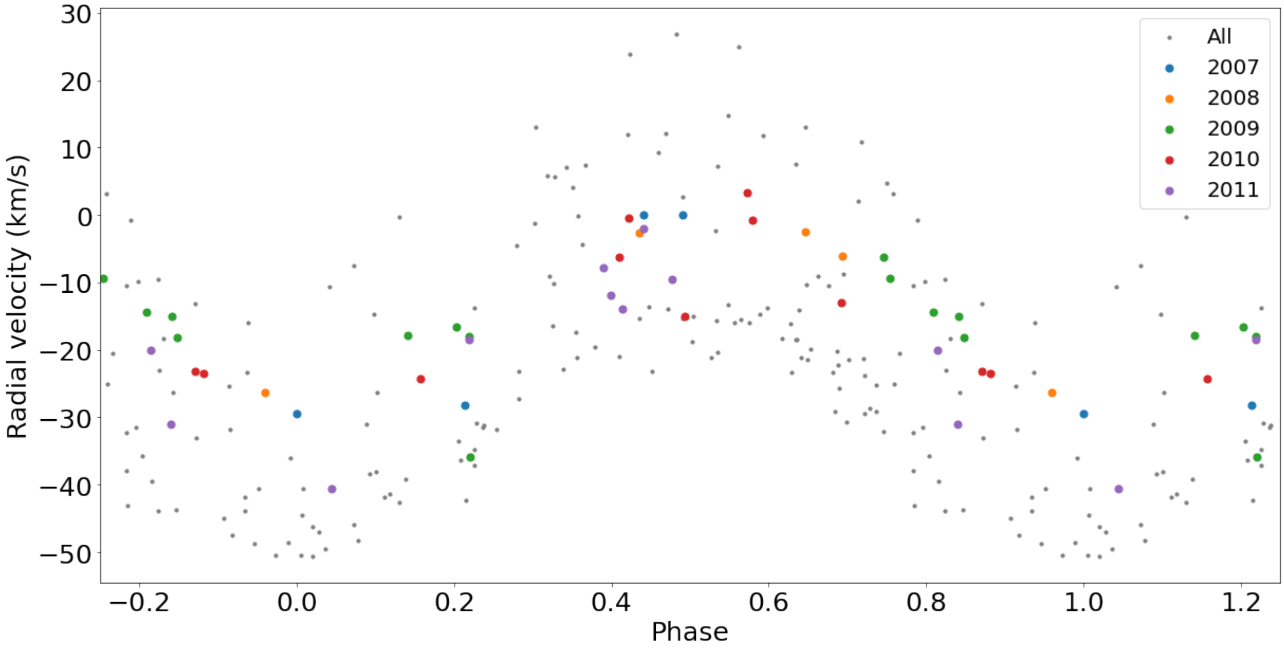

Figure 35: Idem, highlighting 2007 to 2011

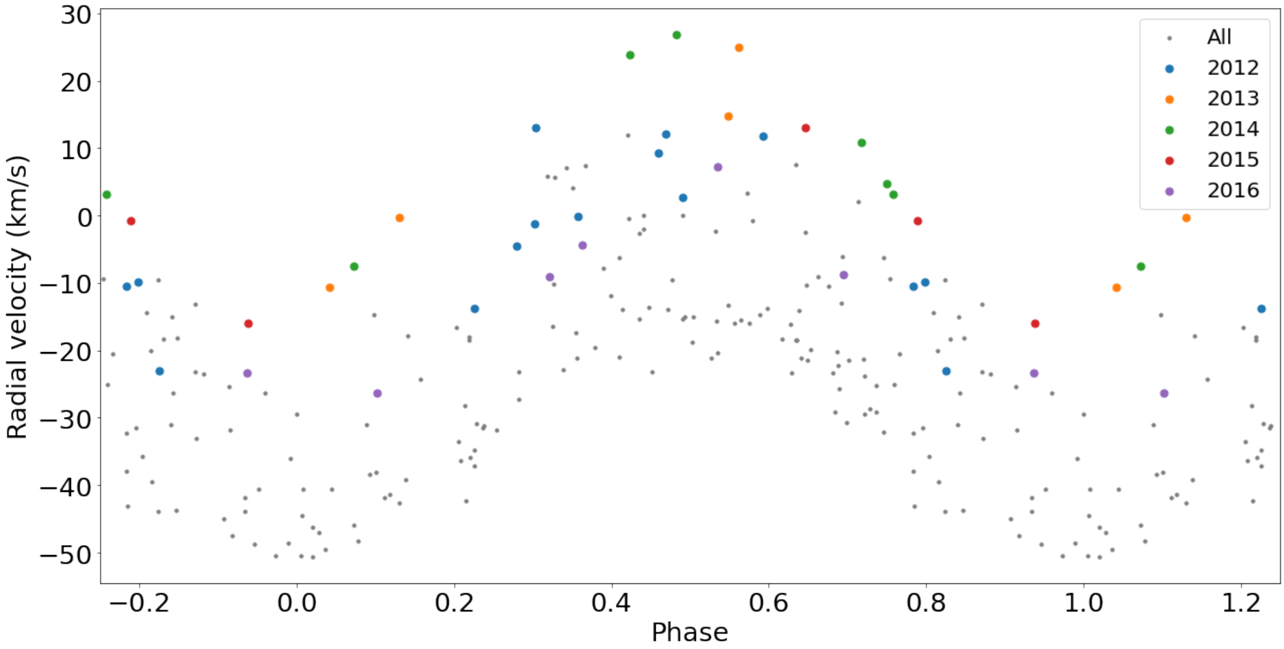

Figure 36: Idem, highlighting 2012 to 2016

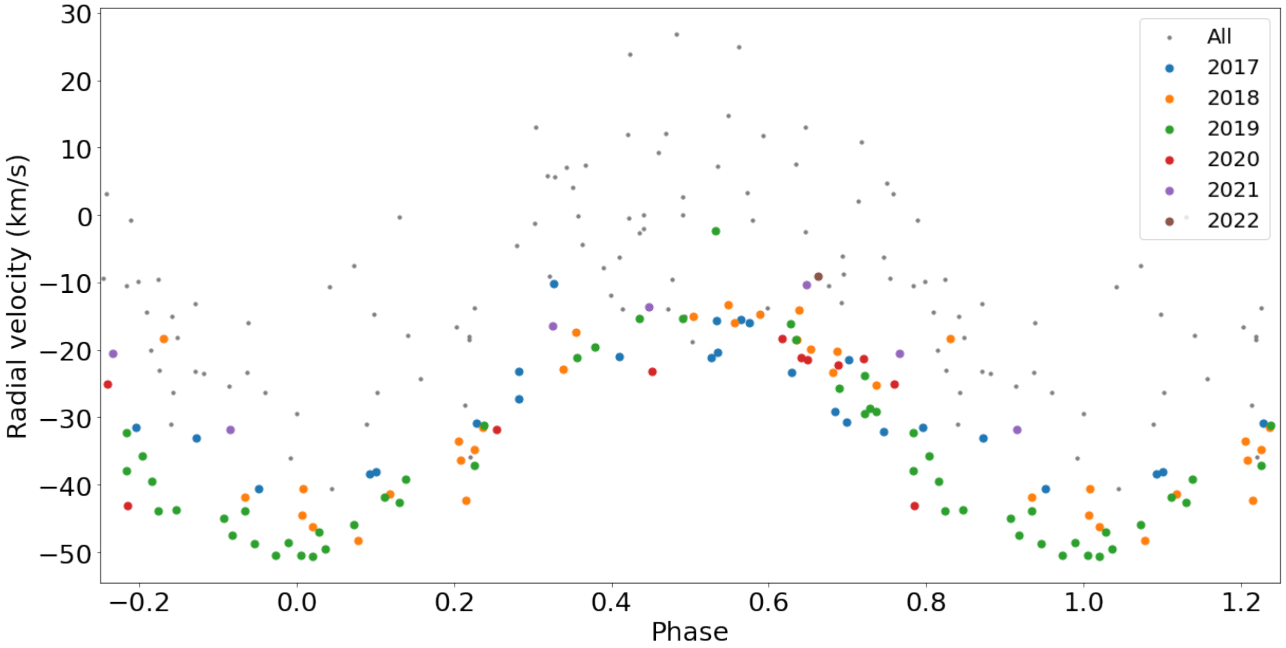

Figure 37: Idem, highlighting 2017 to 2022

- 2003's radial velocities experience a strong positive shift relative to the bulk of the data. Its line profiles are triple-peaked with the red peak dominating (Figure 34).
- 2004's radial velocities are also strongly positively shifted, with the line profiles also being triple-peaked, albeit with a dominant blue peak (Figure 34).
- 2007 presents some radial velocities which are slightly positively shifted relative to the bulk of the data with double-peaked red dominated lines. These lines have rather shallow absorption cores (Figure 35).
- 2008 begins with double-peaked lines and a strong dominance towards the red (having lines similarly shaped to 2007's), before becoming single peaked while remaining asymmetric towards the red. This is briefly interrupted by the appearance of a symmetric double peak. All of the red dominant points are shifted positively relative to the bulk of the data (Figure 35).
- 2010 has some positively shifted radial velocities, corresponding to symmetric and red-dominated double-peaked lines (Figure 35).
- 2012, 2013 and 2014 are all triple-peaked. The red peak dominates until the start of 2014. The overall effect is a strong positive shift relative to the bulk of the data (Figure 36).
- After 2014, the only strongly shifted point are from blue-dominated lines.

Notably, one finds that the radial velocities of triple-peaked lines are the most strongly shifted lines relative to most of the data points. Some of the double peaked red-dominated lines have slightly shifted radial velocities, with 2007 and 2008 being similarly shifted and having similarly shaped red-dominated lines. 2010 also has some shifted points but has differently shaped lines to those of 2007 and 2007. Despite this outlier, similarly shaped lines result in similarly shifted radial velocities.

With this in mind, one way to mitigate the effect of the line profile variation would be to only measure and fit the radial velocities from data solely covering time spans during which the line profiles are relatively stable. Such time spans would have to be long enough to cover the orbital period to be of use in finding an orbital solution. The amplitude and epoch would therefore be less affected by the variations, improving them compared to Fit 1A, 1B, 1C and 2. On the other hand, the systemic radial velocity may remain variable between stable intervals as the lines profiles will in general differ between them. Nonetheless, the stable intervals will be used to find an improved orbital solution. This solution will then be used for the subsequent X-ray analysis.

We will first measure and fit the radial velocities on single years. While the line profile is not likely to be stable enough over the course of a year to obtain an improved orbital solution, we will nonetheless attempt to do so in order to refine the discussion. Only 2004, 2010, 2011, 2016, 2017, 2018 and 2019 have a sufficient number of points covering most of the orbit to be used (see Figures 34, 35, 36 and 37).

Fitting comparison							
	2004	2010	2011	2016	2017	2018	2019
K (km/s)	14.2 ± 1.9	23.6 ± 3.4	17.3 ± 3.0	17.3 ± 3.0	12.1 ± 1.2	16.3 ± 1.3	20.9 ± 0.6
γ (km/s)	-12.8 ± 1.3	-18.4 ± 2.5	-11.0 ± 1.8	-18.9 ± 2.2	-18.2 ± 0.8	-16.2 ± 0.9	-16.3 ± 0.5
T_0 (HJD-2450000)	6107.2 ± 2.4	6116.1 ± 3.0	6107.6 ± 3.8	6113.6 ± 3.6	6106.7 ± 1.8	6111.9 ± 1.7	6105.8 ± 0.6
No. of data points	6	9	9	6	20	24	34
RMS deviation (km/s)	2.9	6.6	5.1	5.3	3.4	4.3	2.5

Table 10: Comparison of fits for individual years. Gaussian parameters used were $a = 200$ km/s and $\sigma = 15$ km/s

The measurements were carried out using the Gaussian method, with an initial guess of a = 200 km/s and σ = 15 km/s. The fit results are shown in table 10. The systemic radial velocity varies year to year, as expected. The epoch result is similarly variable from year to year. If Mourard et al's epoch (2015) were wrong, a gradually increasing drift would be seen but this is not the case: the epoch appears to change randomly from year to year, indicating stochastic variation. The amplitudes vary quite drastically from year to year. This may be the result of a Gaussian separation that is still insufficiently large to shield the measurements from disk variations.

Fitting comparison							
	2004	2010	2011	2016	2017	2018	2019
K (km/s)	15.7 ± 0.3	12.7 ± 3.1	14.8 ± 3.2	15.5 ± 2.1	11.7 ± 1.4	14.8 ± 1.2	18.6 ± 0.7
γ (km/s)	-2.1 ± 0.2	-15.8 ± 2.4	-20.9 ± 2.0	-12.2 ± 1.5	-28.3 ± 1.0	-28.7 ± 0.8	-30.6 ± 0.6
T_0 (HJD-2450000)	6104.2 ± 0.4	6108.01 ± 5.31	6106.3 ± 4.1	6108.1 ± 2.8	6101.8 ± 2.4	6110.8 ± 1.8	6105.0 ± 0.8
No. of data points	6	9	9	6	20	24	34
RMS deviation (km/s)	0.5	6.2	5.6	3.6	4.2	4.2	2.9

Table 11: Idem for Gaussian parameters a = 250 km/s and σ = 15 km/s

Fitting comparison							
	2004	2010	2011	2016	2017	2018	2019
K (km/s)	11.8 ± 0.5	7.2 ± 4.4	15.3 ± 3.0	12.8 ± 2.0	10.3 ± 1.7	11.4 ± 1.3	16.0 ± 0.8
γ (km/s)	5.8 ± 0.3	-16.8 ± 3.2	-27.0 ± 1.8	-5.8 ± 1.5	-32.9 ± 1.2	-35.8 ± 0.9	-38.8 ± 0.6
T_0 (HJD-2450000)	6103.8 ± 0.8	6093.01 ± 12.24	6107.8 ± 3.7	6106.2 ± 3.3	6100.0 ± 3.3	6112.2 ± 2.6	6105.9 ± 1.0
No. of data points	6	9	9	6	20	24	34
RMS deviation (km/s)	0.8	8.4	5.2	3.5	5.2	4.6	3.1

Table 12: Idem for Gaussian parameters $a = 300$ km/s and $\sigma = 15$ km/s

We first test the impact of the Gaussian separation by testing values of 250 and 300 km/s. As seen in Tables 11 and 12, the amplitude for most single-year solutions (particularly 2004, 2016, 2017 and 2018) approaches the values obtained by Mourard et al (2015) of 10.2 ± 1.0 once the Gaussian separation becomes sufficiently large (Table 12)[24]. The epoch however remains inconsistent between fits. On the other hand, 2010, 2011 and 2019 fail to replicate this result. This once again stems from the line profile variation, with 2010's lines being particularly unstable, starting blue-dominated before becoming red-dominated.

This discrepancy between the single-year solutions shows that they cannot be relied upon to improve the result as the line profile remains too variable over the course of the year. We therefore further restricted data to intervals during which the line profile is relatively stable. Four such intervals display sufficient number of points over the orbital phases to perform individual fittings(all dates given in HJD-2450000): 5534 to 5907 (hereafter Int1), 7638 to 7793 (hereafter Int2), 8017 to 8133 (hereafter Int3) and 8328 to 8428 (hereafter Int4) (See Figures 38, 39, 40 and 41 for the corresponding line profiles and Figure 42 for their position on the radial velocity phase curve).

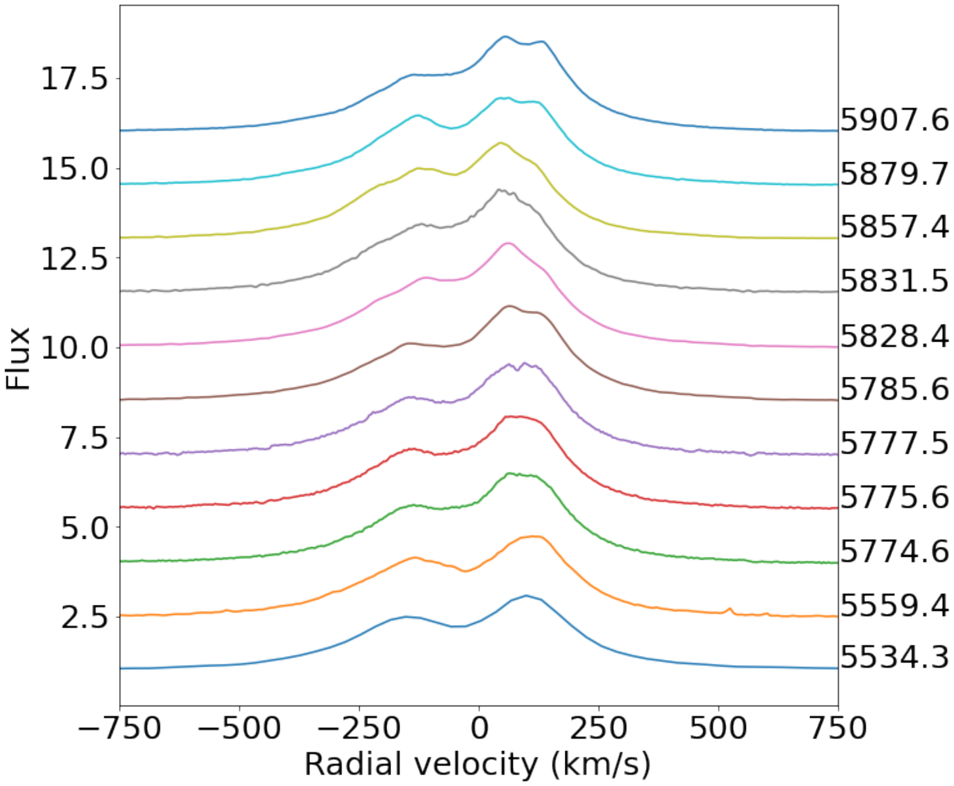

Figure 38: Int1 line profiles.

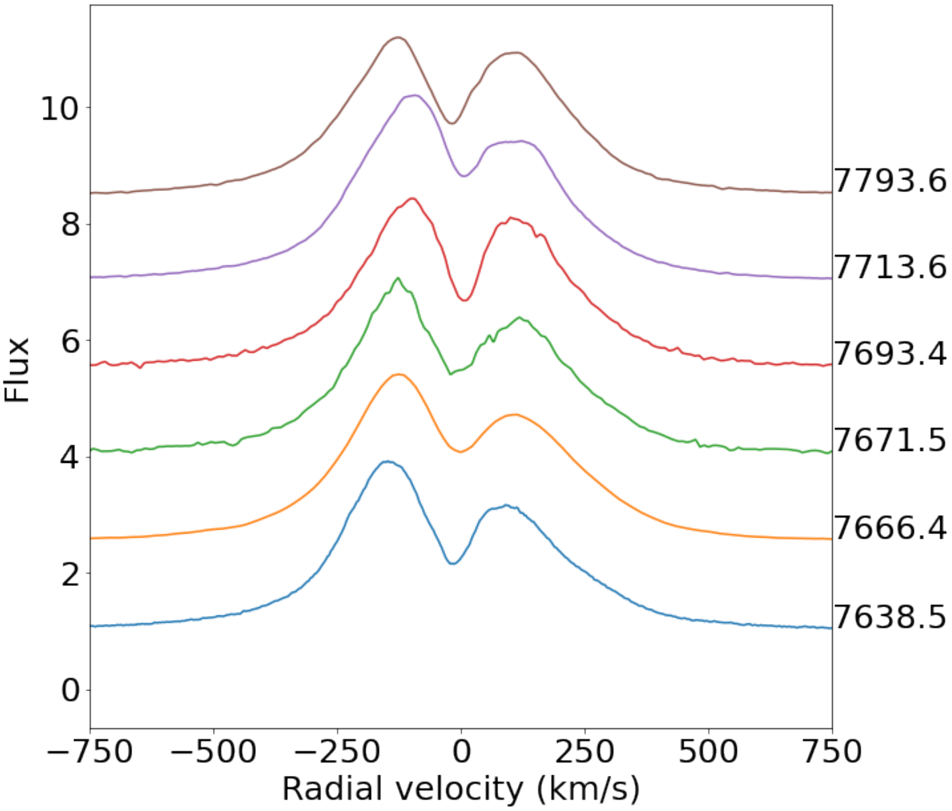

Figure 39: Int2 line profiles.

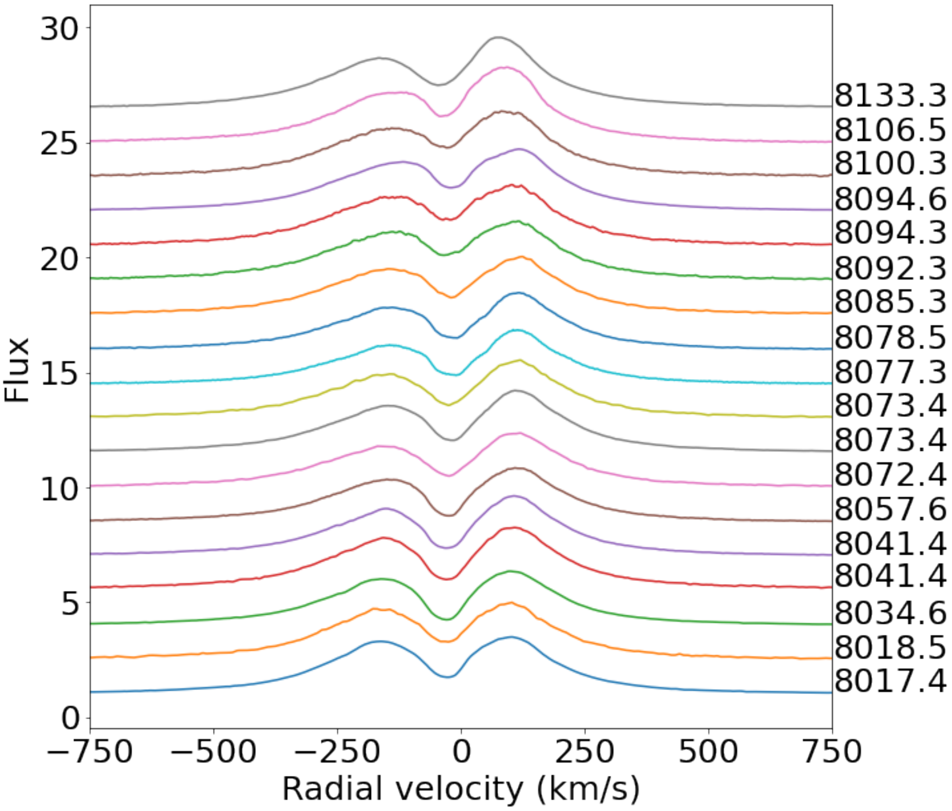

Figure 40: Int3 line profiles.

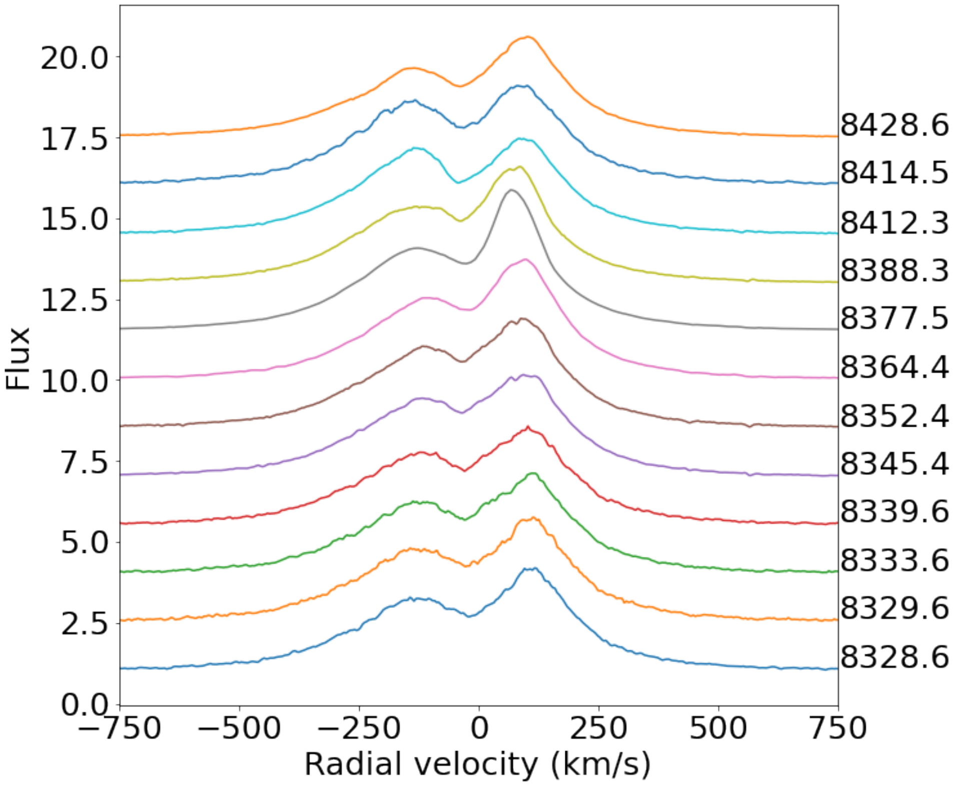

Figure 41: Int4 line profiles.

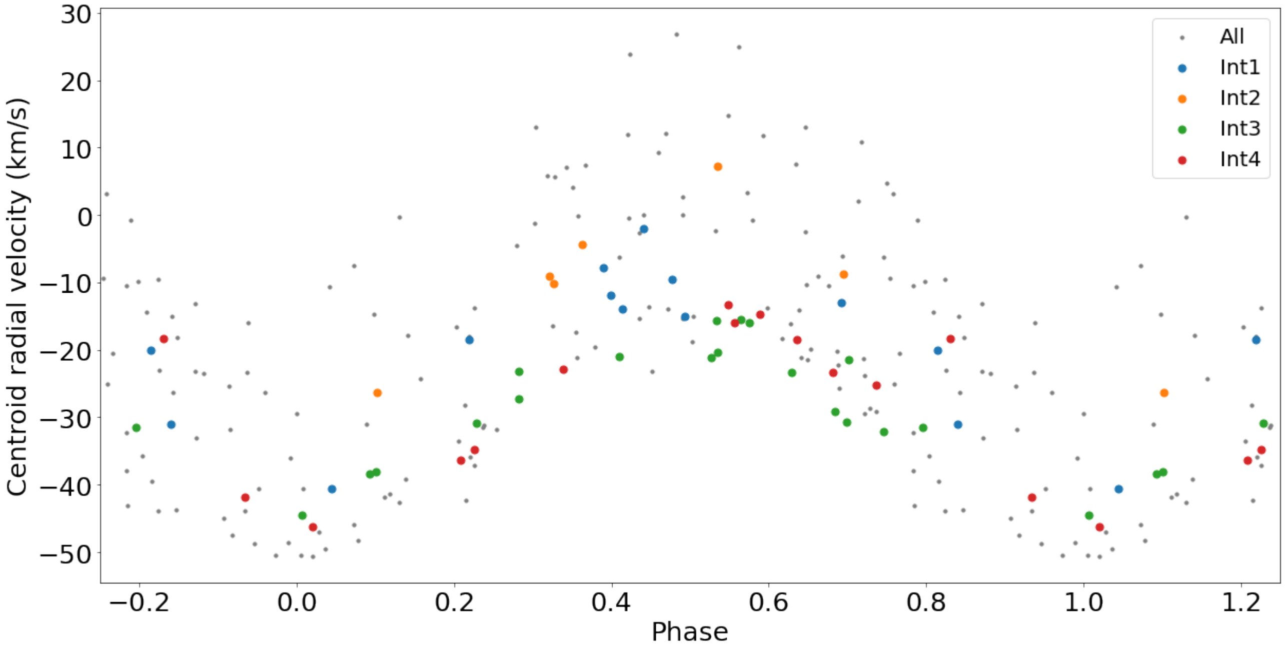

Figure 42: Gaussian radial velocities by phase (a = 250 km/s), highlighting the stable intervals.

The measurements for the fits were carried out with a = 200, a = 250 and a = 300 km/s, all with σ = 15 km/s.

Fitting comparison				
	Int 1	Int 2	Int 3	Int 4
K (km/s)	16.2 ± 2.9	20.7 ± 2.3	13.7 ± 1.2	14.5 ± 2.2
γ (km/s)	-11.1 ± 1.2	-21.4 ± 1.8	-19.1 ± 0.8	-16.2 ± 1.6
T_0 (HJD-2450000)	6108.2 ± 3.2	6109.2 ± 2.0	6105.6 ± 1.8	6112.0 ± 3.2
No. of data points	11	6	18	12
RMS deviation (km/s)	5.7	3.3	3.2	5.3

Table 13: Comparison of fits for periods of stability. Gaussian parameters used were a = 200 km/s and σ = 15 km/s

Fitting comparison				
	Int 1	Int 2	Int 3	Int 4
K (km/s)	13.7 ± 2.9	16.8 ± 2.5	12.3 ± 1.1	13.7 ± 2.1
γ (km/s)	-21.1 ± 1.9	-13.6 ± 1.9	-29.7 ± 0.8	-28.5 ± 1.5
T_0 (HJD-2450000)	6106.3 ± 3.8	6107.7 ± 2.7	6103.4 ± 1.8	6112.5 ± 3.2
No. of data points	11	6	18	12
RMS deviation (km/s)	5.7	3.5	3.0	5.0

Table 14: Idem for Gaussian parameters $a = 250$ km/s and $\sigma = 15$ km/s

Fitting comparison				
	Int 1	Int 2	Int 3	Int 4
K (km/s)	12.9 ± 3.0	12.2 ± 3.9	10.2 ± 1.0	10.4 ± 2.1
γ (km/s)	-27.9 ± 2.0	-6.4 ± 2.9	-34.5 ± 0.7	-36.0 ± 1.5
T_0 (HJD-2450000)	6105.4 ± 4.3	6109.1 ± 5.8	6103.5 ± 2.1	6115.3 ± 4.3
No. of data points	11	6	18	12
RMS deviation (km/s)	5.9	5.4	2.8	5.1

Table 15: Idem for Gaussian parameters $a = 300$ km/s and $\sigma = 15$ km/s

Once again, the amplitudes appear to converge towards the values measured in the past as the Gaussian separation approaches 300 km/s (Tables 13, 14 and 15), cementing $a = 300$ km/s as the value that should be used for the final fit. The amplitudes obtained for the stable line profiles also vary less dataset to dataset than the yearly amplitudes. Indeed, the two most distant amplitude results at $a = 300$km/s (Int 1 and Int 3, Table 15) are only 0.9σ apart compared to the 2.0σ that separates the two most distant yearly amplitude results, those of 2010 and 2019 (Table 12). This showcases the effect further limiting the impact of disk variations has on the fit results. A visual representation of the effect of changing the Gaussian parameters on both the single year data and the stable interval data is shown in Appendix B.

4.3 Final fit

Having compared the fits obtained with different measurement parameters for various sets of line profiles, we are now able to propose a recommended ephemeris. Our best-fit is calculated from radial velocities determined using $a = 300$ km/s and $\sigma = 15$ km/s during Int 3 and Int 4 as well as during two new intervals: Int 5 (8142 to 8177) and Int 6 (9076 to 9515) which did not have sufficient coverage for the single-interval fits. Int 3 and 4 present very close systemic velocities (see Table 15). These two data sets can be combined without much effect on the final fit while increasing the number of points to 30. Int 5 and Int 6 are similarly shifted to Int 3 and 4 (see Figure 43)and will therefore also be combined further increasing the total number of points to 47. The final fit's (Fit 3) parameters and resulting curve are shown in Table 16 and on Figure 44, respectively.

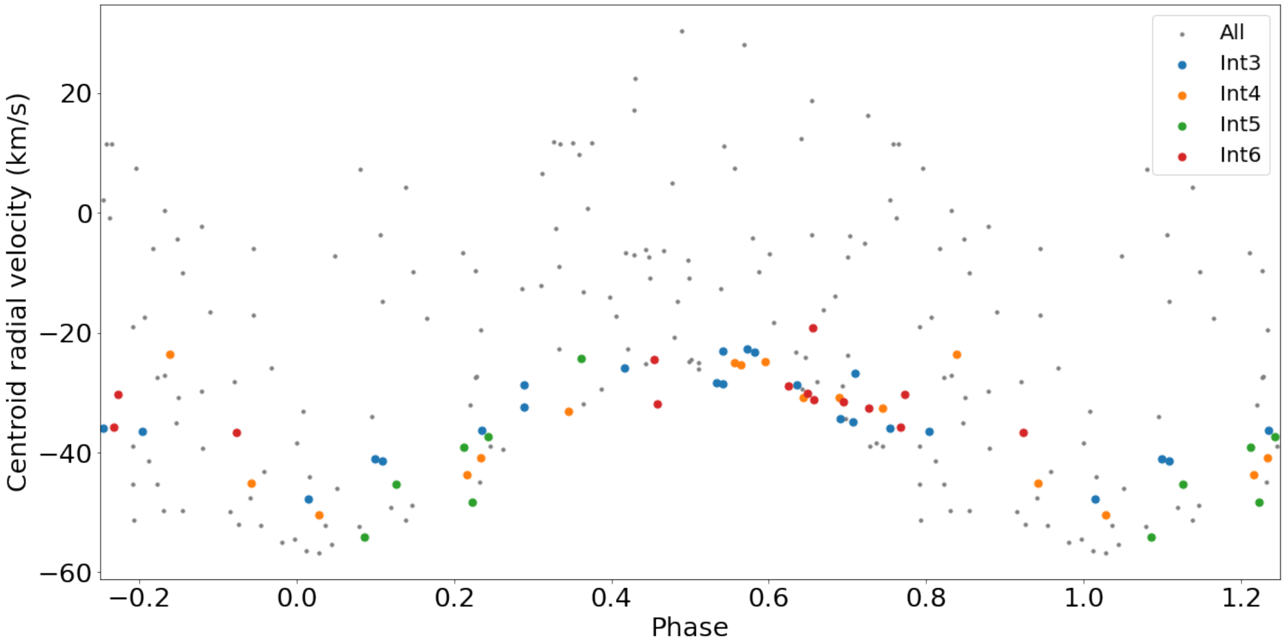

Figure 43: Gaussian radial velocities by phase ($a = 300$ km/s), highlighting the stable intervals.

Fitting parameters (Fit 3)	
γ (km/s)	-35.4 ± 0.7
A (km/s)	0.3 ± 1.0
B (km/s)	-10.2 ± 1.0
Phase shift (rad)	-1.6 ± 0.1
K (km/s)	10.2 ± 1.0
T_0 (HJD-2450000)	6109.5 ± 1.9
No. of data points	47
RMS deviation (km/s)	4.5

Table 16

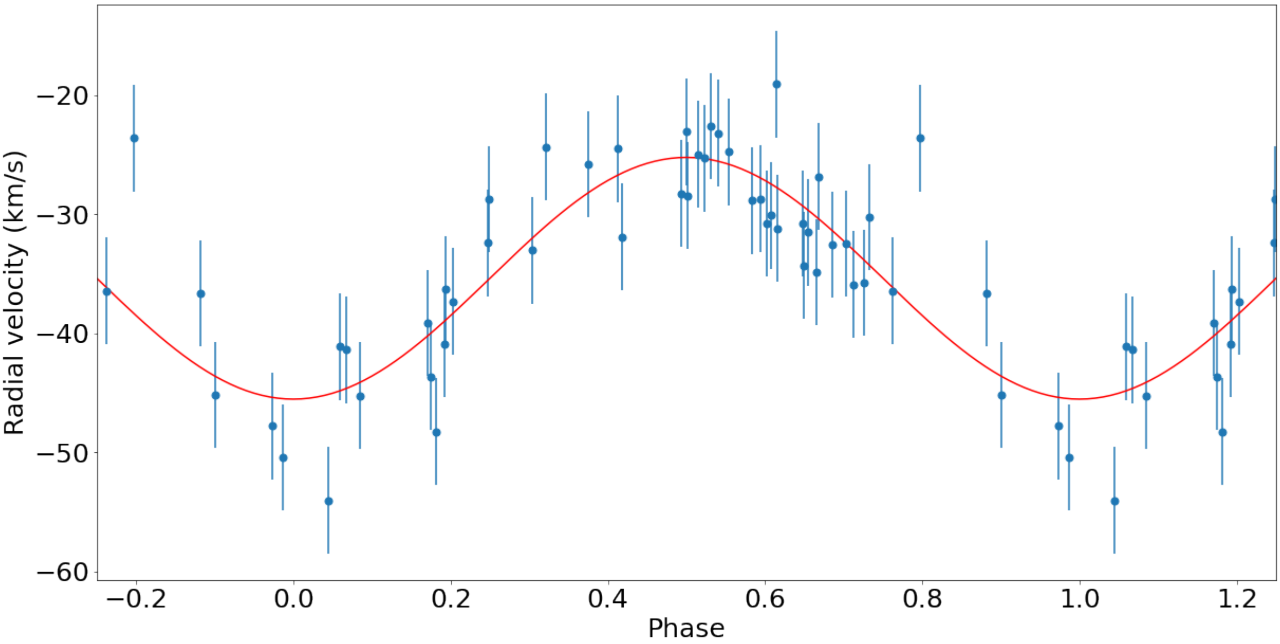

Figure 44: Radial velocity measurements and Fit 3.

Fit 3's amplitude and epoch are 0.04σ and 0.3σ from Mourard et al's result (2015) respectively, a significant improvement over Fit 1 [24]. On the other hand, the final systemic velocity difference remains very large at 39.2σ as restricting our fit to stable intervals limits the effect of the line profile variation on the amplitude result, but does not mitigate its effect on the γ result. A direct comparison between the two is shown on Figure 45.

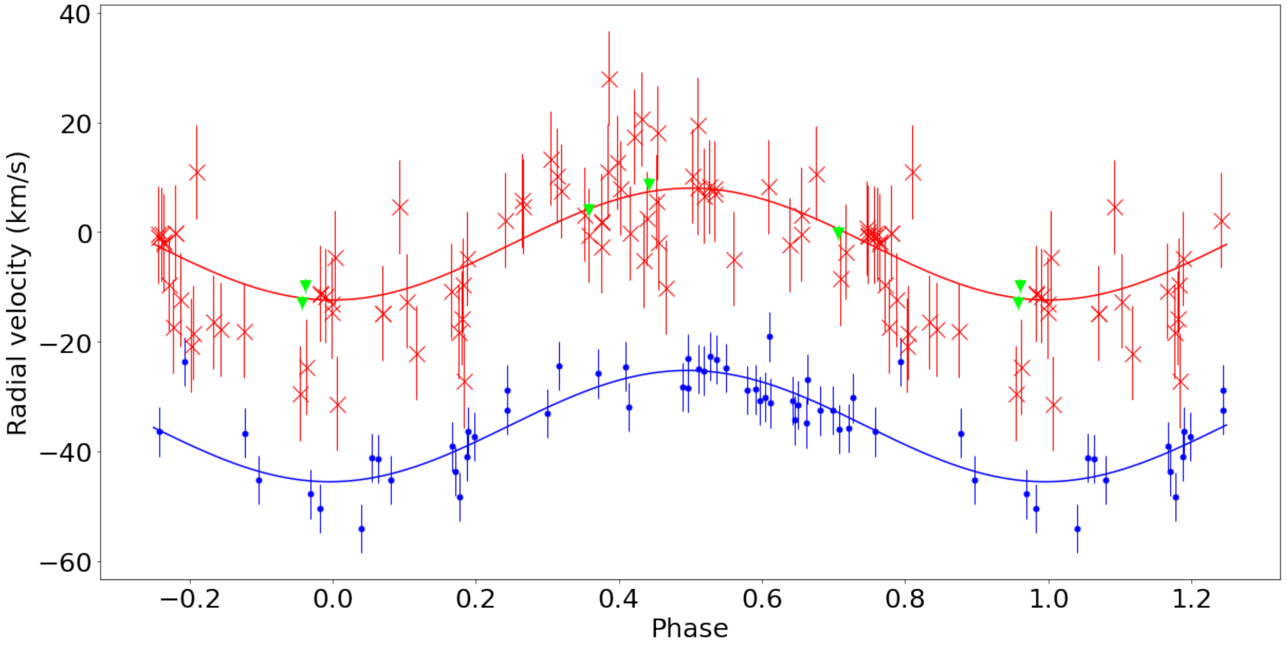

Figure 45: Comparison between the Fit 3 (points marked with dots) and Mourard et al's result (2015) (points marked as red x for the Hα data and green triangles for the UV data) [24]

5 X-ray analysis

In this final section, we will study ϕ Per's X-ray emission. Past observations have failed to detect any such emission [27], as they were rather shallow, so new, deeper X-ray observations were carried out. The orbital solution obtained in the previous section will be used to determine the phases of these observations allowing us to study whether the X-ray emission varies with the orbital phase and thus is related to the companion. The X-ray observations of ϕ Per were carried out using the Chandra X-ray Observatory.

5.1 Chandra and observations

5.1.1 Introduction to Chandra

Launched in 1999, the Chandra X-ray Observatory is currently NASA's flagship X-ray space telescope. It is the third space telescope of NASA's Great Observatory program which consists of the Hubble Space Telescope, the Compton Gamma Ray Observatory, the Chandra X-ray Observatory and the Spitzer Space Telescope. Of these four space telescopes, only Hubble and Chandra are still in service, with Chandra's mission being funded up to 2025 with possibilities for extension up to 2030 [59].

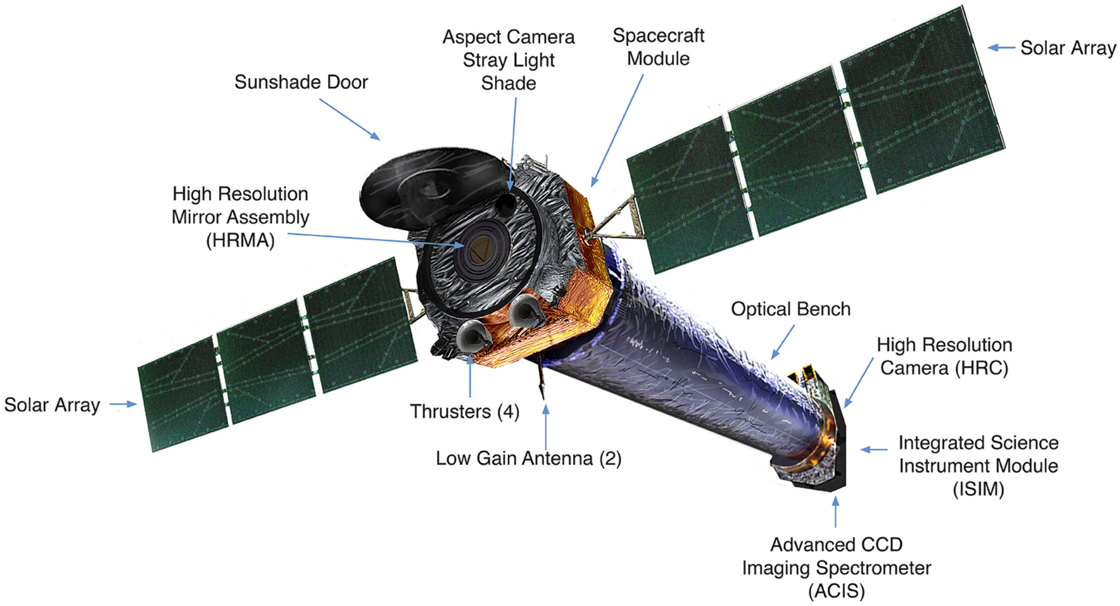

Figure 46: Illustration of the Chandra spacecraft and its components. Credit: NASA/CXC and J.Vaughan

The X-ray telescope aboard Chandra consists of 4 nested iridium-coated Wolter type I mirrors with an aperture of 1.2 meters and a focal length of 10 meters, known as the High Resolution Mirror Assembly (HRMA). The HRMA allows for X-rays of energies up to 10 keV to be focused while having an on-axis resolution of 0.5". This high sensitivity and high resolution allows Chandra to study very faint sources, even in crowded fields [56]. It is placed on a highly elliptical orbit with an apogee of 146000 km and a perigee of 2600 km. The spacecraft therefore spends 70% of it's orbit above the Earth's radiation belts (in which the instruments could be damaged if they remained for too long), allowing for very long continuous observations of up to 180000 seconds (2.08 days) [57].

The actual detection and measurement of X-rays are done by two instruments located at the focus of the telescope: the High Resolution Camera (HRC), and the Advanced CCD Imaging Spectrometer (ACIS)[56]. The former allows for high-resolution and wide-area imaging as well as very fast timing measurements but without spectral resolution, the latter measures the energy, position and arrival time of individual X-ray photons albeit with a smaller field of view than the HRC. In addition to these focal plane instruments, Chandra is also equipped with the High Energy and Low Energy Transmission Gratings (HETG and LETG). As they both produce dispersed spectra at the focal plane, they perform higher-resolution spectroscopy of bright X-ray sources using the HRC or ACIS cameras as detectors [53].

The ACIS features two detectors, ACIS-I and ACIS-S (see Figure 47). Both are arrays of 1024×1024 pixel CCDS, with ACIS-I being a 2×2 array used for imaging and ACIS-S being a 1×6 array that can be used both for imaging and for high-resolution spectroscopy in conjunction with the HETG or LETG [57]. The fields of view and time resolutions of the Chandra instruments are shown in Table 17.

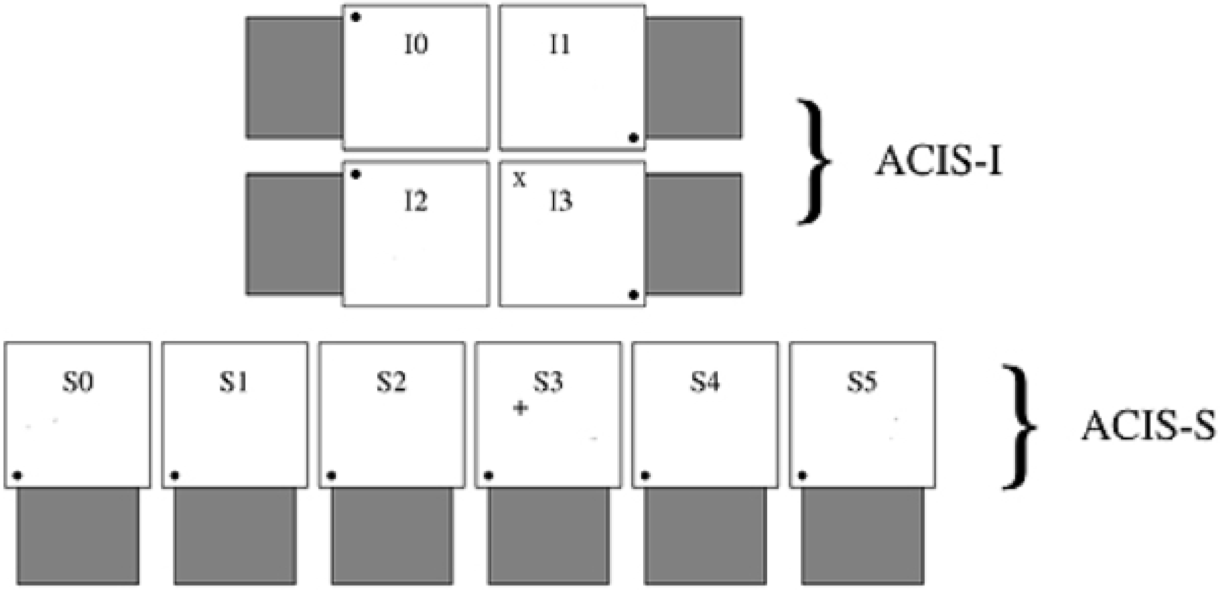

Figure 47: Layout of the ACIS' detectors. Taken from [55]

Two of ACIS' ten CCDs are back-illuminated (BI) rather than front-illuminated (FI), S1 and S3. The BI CCDs are more efficient at lower energies, while the FI CCDs are more efficient at higher energies. Initially, the FI chips had a better spectral resolution (see Figure 48). However this is no longer the case due to degradation of the FI CCDs, whereas the BI CCDs have remained nearly unaffected [57]. Of all the ACIS CCDs, currently S3 offers the highest spectral resolution[53]: our observations used this CCD.

	Widest FoV (arcmin)	Time resolution
HRC-I	30x30	/
HRC-C	3.4x99 (LETG spectroscopy) - 6x30 (timing mode)	10 ms (LETG spectroscopy) - 16μs (timing mode)
ACIS-I	16.9x16.9	3.2 s
ACIS-S	49.8x8.3	3.2 s

Table 17: Comparison of some of the characteristics of the various detectors on board Chandra. The time resolutions shown for the ACIS are maximum resolutions of the default operating mode. Information taken from [53].

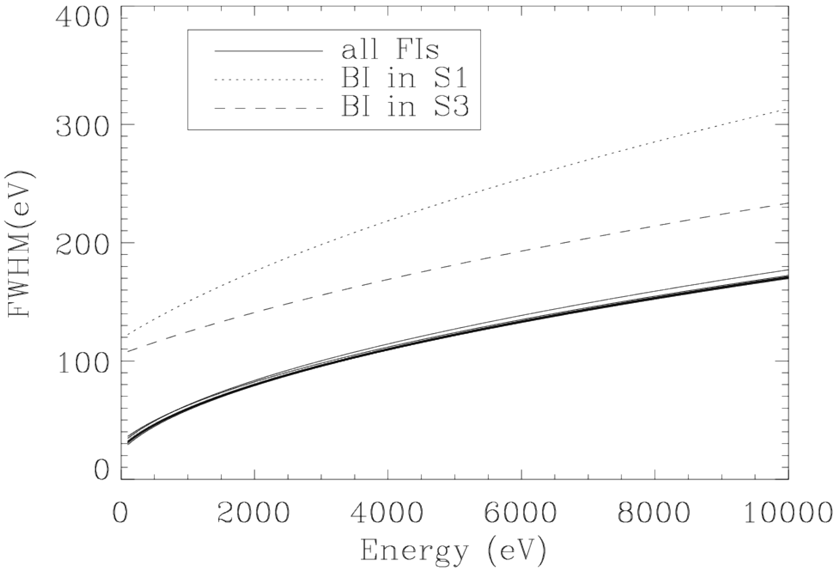

Figure 48: Pre-launch energy resolution of ACIS chips as a function of energy. The BI chips have retained this resolution since launch whereas the FI chips have not. Taken from [57].

It should also be noted that the imaging region of both ACIS detectors can be restricted to specific subarrays: This allows for a reduced read-out time, effectively increasing the time resolution of the detector albeit at the cost of the field of view. The default subarrays cover 1/2, 1/4 and 1/8 of the CCD [57]. The default subarray positions for the CCDs of either detector are shown on Figure 49. The time resolution when using these sub arrays on the whole detector or a single CCD are shown in table 18. Finally, it is important to note that the back-illuminated CCDs cannot be used without also using a front-illuminated chip. This front-illuminated chip monitors the background radiation to protect the instruments from damage. This task was formerly assigned to a dedicated instrument, Electron Proton Helium Instrument (EPHIN), which has since become unusable. Therefore the S3 CCD used for the observations will not achieve its maximum time resolution of 0.4 s, but instead achieves 0.5 s.

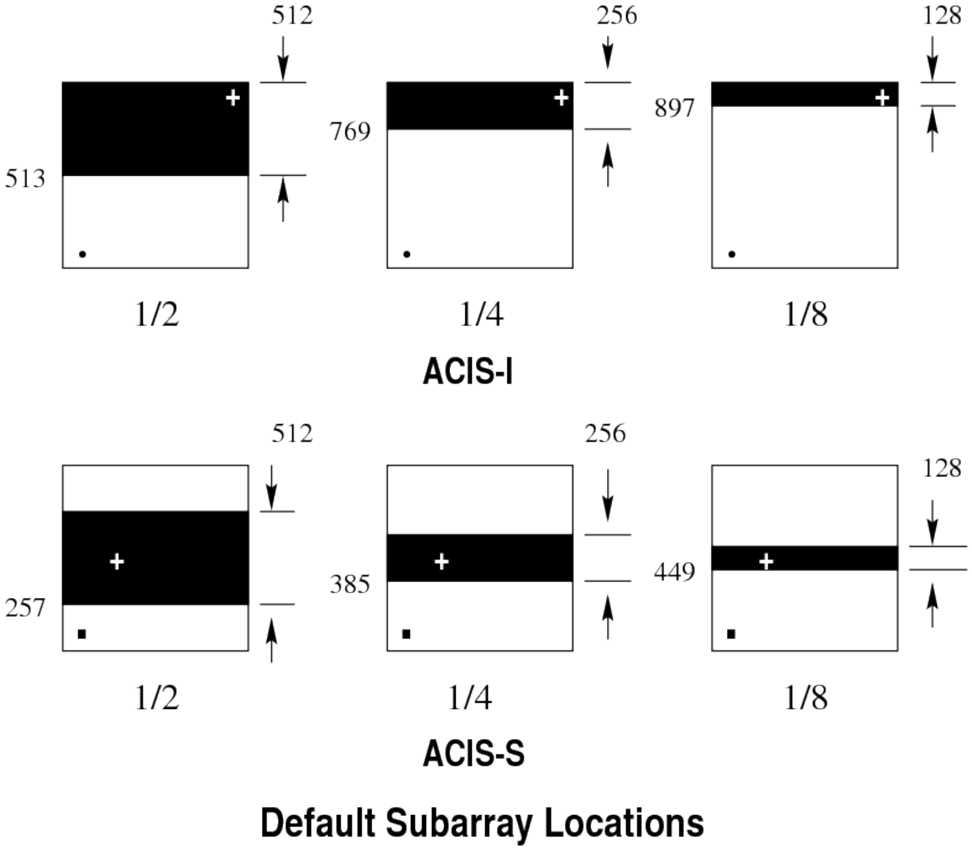

Figure 49: ACIS subarrays with their dimensions noted in pixels. Taken from [57]

	ACIS-I		ACIS-S	
Subarray	Time resolution, all CCDs (s)	Time resolution, single CCD (s)	Time resolution, all CCDs (s)	Time resolution, single CCD (s)
1/2 CCD	1.8	1.5	1.8	1.5
1/4 CCD	1.2	0.8	1.1	0.8
1/8 CCD	0.8	0.5	0.7	0.4

Table 18: ACIS time resolution for various subarrays. Information taken from [57].

5.1.2 Observations

The X-ray observations of ϕ Per were carried out using the ACIS-S3 CCD (1/8 subarray mode), as its ability to identify the individual X-ray photons and their arrival positions is crucial for the study of a likely faint source like ϕ Per. The 1/8 subarray mode was chosen to ensure as many single X-ray photons as possible could be individually detected thanks to the increased time resolution, as the luminosity of ϕ Per's emission was not known when the observations were proposed, and the usual setup would have caused problems for high luminosities (see Section 5.2.4).

Two observations were carried out, one in July and one in August 2022. The exact dates and their corresponding phases can be found in table 19. The X-ray data takes the form of an event list, i.e. a table containing the arrival time, position and shape of the electron cloud associated to each X-ray photon. The images from both observations are shown on Figure 50.

Observation date	2022-07-22	2022-08-23
Start time	08:56:05	14:17:45
End time	10:18:45	15:37:02
Duration (seconds)	4960	4865
Mid phase	0.0	0.25

Table 19: Observation characteristics. The mid phase was obtained utilising the final orbital solution from Section 4.3, Table 16 (reference epoch HJD 2456108.3 ± 1.0 and period 126.6982 ± 0.0035 days).

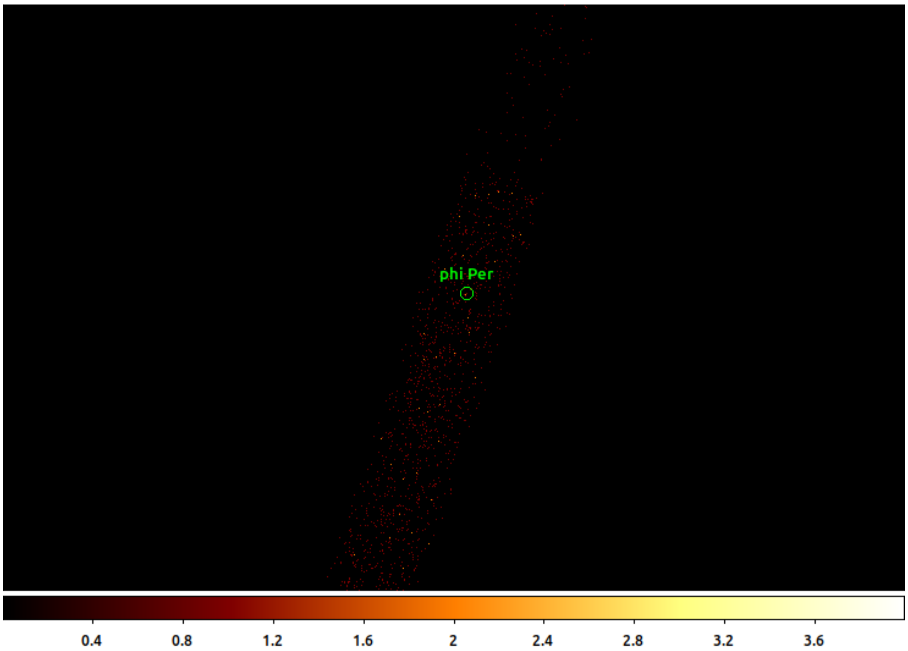

(a)

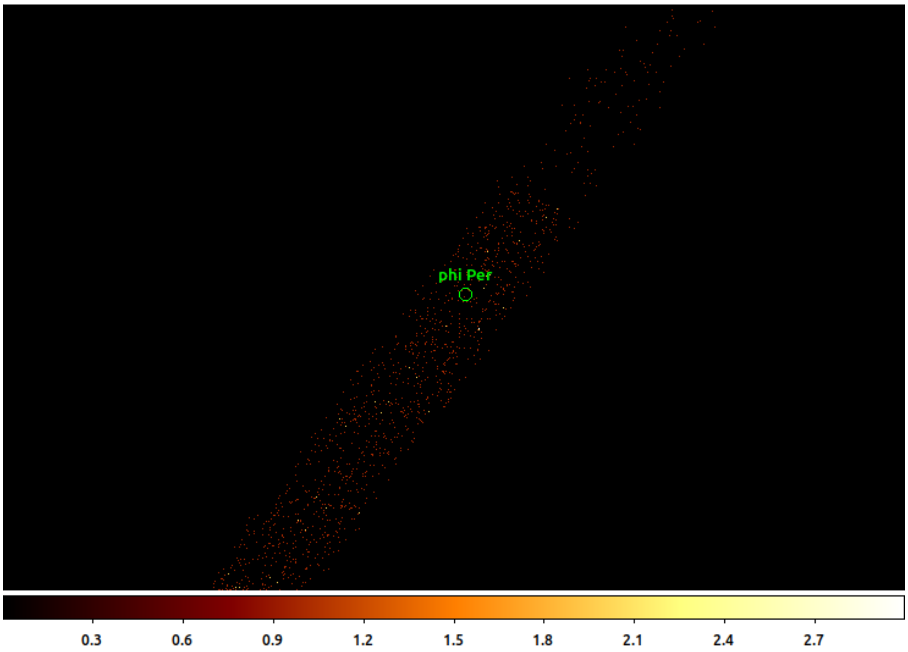

(b)

Figure 50: X-ray images from July (top) and August (bottom), highlighting the position of ϕ Per by a circle of 5" radius. The pixel colour indicates the number of X-ray photons detected within it.

5.2 Methodology

In this section the methodology of the analysis will be described. A large part of the subsequent data analysis was carried out using tools from Chandra Interactive Analysis of Operations (CIAO) software package. CIAO was specifically developed by the Chandra X-ray Center for analysis of Chandra data, making it ideal for the ϕ Per data.

The first step of the data analysis is to determine whether any X-ray source was detected within the field of view of the observations. CIAO offers two tools to facilitate this process: wavdetect and celldetect. Both tools have been used as one may identify a source while the other does not (since their detection methods are different) and more importantly, clear and significant sources should be found by both, allowing for a confirmation. Before detailing these tools, it should be noted that they both use image files rather than the original event files. Luckily CIAO provides a tool to generate exposure-corrected images from event lists within a specific energy band: fluximage. This tool also allows for the creation of a "PSF map", an image containing the radius of the point-spread function (PSF) in each pixel corresponding to a chosen enclosed count fraction or ECF [54].

5.2.1 Wavdetect

The more complex of the two detection tools is wavdetect. While slower and more memory intensive than celldetect, it can identify closely-spaced sources as separate and better identify extended sources. It functions by correlating the data with Marr wavelet (or "mexican hat") functions of various scales (see Figure 51) [54].

The wavelet function used in wavdetect is given by [52]:

$$W\left(x,y,s\right)=\frac{1}{\pi s^2}\left(1-\frac{x^2+y^2}{2s^2}\right)e^{-\frac{x^2+y^2}{2s^2}} \tag{22}$$

Where s is the wavelet scale.

For each given wavelet scale, pixels with high correlation values are removed from the data. Specifically, in each pixel, the correlation value C_i and the background B_i are estimated. This allows for the probability sampling distribution of C_i for a given B_i to be determined. It will hereafter be noted $P\left(C_i\left(B_i\right)\right)$. A threshold value C_T can then be calculated using a user-chosen significance value S_i by solving the following equation [54]:

$$S_i=\int\left(C_T dC_i\right)P\left(C_i\left(B_i\right)\right) \tag{23}$$

When a pixel presents $C_T < C_i$, it is removed from the image and replaced with the estimated background. This cleansing process is repeated until either a specified maximum number of

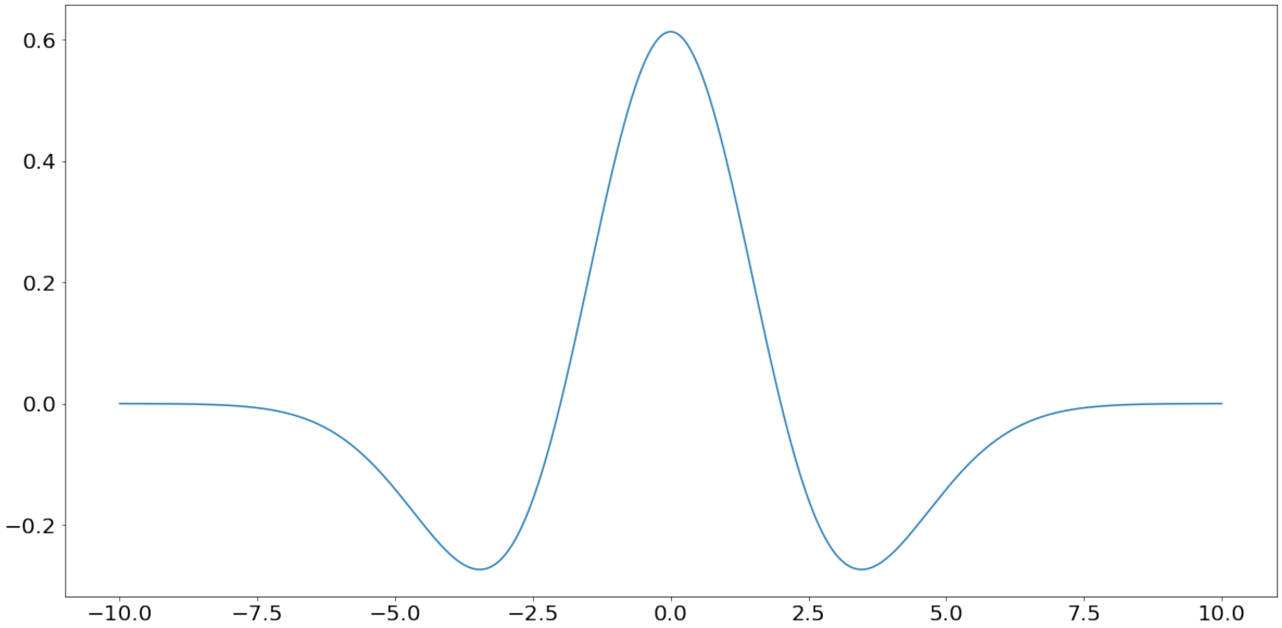

Figure 51: 2D mexican hat wavelet, with a scale value of 2

iterations (2 by default) is reached or the ratio of newly cleansed pixels to the total number of pixels falls below a preset value (0.0001 by default), i.e. too few new sources were found. Once this process stops, the cleansed data is used to estimate the background, which is then used to calculate a new threshold with the same method as during the cleansing process (Equation 23), albeit with a different significance value. This new threshold is then applied to the initial correlation of the raw data and the wavelet function for a final run of source identification [54].

This process is repeated for each wavelet scale. The properties (such as the count rate, location and if a PSF map is provided, the PSF size) of each source found for each scale are then computed [54].

5.2.2 Celldetect

Compared to wavdetect, celldetect is simpler and less memory-intensive to operate. It is also better at identifying faint sources. On the other hand, it has difficulty identifying individual sources in crowded fields, or extended sources (which it detects as multiple point sources). It functions by measuring the signal-to-noise ratio in a square-shaped cell. If the signal to noise ratio is above a given threshold, a candidate source is registered at the location of the cell. The signal is measured by simply summing the X-ray counts within the cell. The noise can be measured in different ways. The default method uses a larger background cell surrounding the signal cell. The counts in the background cell are then again simply summed and compared to the signal counts[54].

The SNR measurement is carried out for the complete dataset by covering the entirety of the image with overlapping cells. The size of the cell at a given location is determined by the point spread function at that point (given by the PSF map image generated by fluximage). As the PSF's size increases the further off-axis it is measured, so does the size of the cell. However, celldetect allows for a fixed cell size to be defined if needed [54].

5.2.3 Srcflux

While the two previously described tools aim at detecting X-ray sources, a good method for calculating the actual flux of any such source has yet to be detailed. Luckily, CIAO provides a tool for just that purpose: srcflux. This tool calculates the net count rate and flux of X-ray sources from an event list. The count rate is obtained with a method similar to aperture photometry, using a source region and an outer background region, subtracting the latter from the former, after adequate scaling. If these aperture shapes are not supplied by the user, the tool will generate a circular aperture encompassing 90% of the PSF size at 1 keV for the source region. The background region will then take the form of an annulus, whose inner and outer radii are equal to the source region's and 5 times the source region's respectively. This tool can also calculate upper and lower bounds corresponding to a confidence interval of a given significance. In the case of a non-detection, it will instead return an upper limit for the source count-rate [54].

Srcflux calculates the flux associated to the count rate assuming simple emission models (often typical of AGN emission). We will not make use of this capability but of dedicated models (see Section 5.2.4). Finally, srcflux allows for the combination of multiple data sets for a net count rate calculation [54]. This will allow us to combine our two observations.

5.2.4 Flux and Luminosity calculation

With the count rates in hand, the X-ray flux, hence the luminosity (or its upper limit in the case of no detection) of ϕ Per can be computed. The source flux will be calculated using the WebPIMMS tool provided by NASA's High Energy Astrophysics Science Archive Research Center (HEASARC). WebPIMMS, a web-version of the Portable Interactive Multi-Mission Simulator, allows for the conversion of count rates in a given energy band between instruments, or for the conversion of count rates into flux in a chosen band (in $erg/cm^2/s$). In all cases, it requires for the physical mechanism behind the X-ray emission to be taken into account by offering the ability to choose a model of the source emission such as thermal bremsstrahlung, the power law characteristic of emission arising from relativistic particles or an optically thin plasma[60]. In our case, we have chosen optically thin plasma, as X-ray emission from massive stars is usually of this type since it is emitted from hot plasma formed by shocks within the star's wind or from collisions between two stars' winds [27]. Since the hardness of ϕ Per's emission is not known, we have looked at the typical emission of other massive stars: OB stars typically emit soft X-rays with on average energies of $kT \sim 0.6$ keV. On the other hand, γ Cas stars emit at much higher energies ($kT \geqslant 5$ keV). Finally, Be + sdO systems that have been detected in X-rays have been found to have soft X-ray emission ($kT \sim 0.2$ keV) [27]. We have thus chosen a range of values for the temperature of the plasma which covers these three cases, along with an intermediate temperature between the typical OB and γ Cas energies, and an additional higher temperature in case ϕ Per's emission is particularly hard: $log(T) = 6.4, 6.85, 7.45, 7.8$ and 8.05, corresponding to energies of 0.24, 0.61, 2.43 5.44 and 9.67 keV. In addition, the emission can be absorbed by material along the line-of-sight. The amount of material will be represented by the column density of neutral hydrogen. The minimum value corresponds to the interstellar absorption and its column density N_H can be calculated from the reddening $E(B-V)$ using the following relation [12]:

$$N_H = 6.12 * 10^{21} E(B-V) \tag{24}$$

For ϕ Per, the interstellar absorption was accounted for using $E(B-V) = 0.162$ [?]. Circumstellar absorption may occur but is totally unknown for ϕ Per so it was put to zero. WebPIMMS provides both the observed flux as well as the flux corrected for interstellar absorption, which we will call F_X. The X-ray luminosity L_X can then be obtained using:

$$L_X = 4\pi d^2 F_X \tag{25}$$

Where d is the Gaia distance to the target. (184 ± 8 pc [2])

5.3 Results

5.3.1 Source detection

Fluximage was first used to create the exposure-corrected images and PSF maps for both observations. The energy band chosen was 0.5 to 10 keV as this is the range in which current X-ray instruments are the most sensitive. The PSF ECF is 0.8. The exposure corrected images are shown on Figure 52.

Wavdetect and celldetect were run using the exposure-corrected images and PSF map. Both of wavdetect's default significance thresholds were kept, which are 0.001 for the cleansing process and 10^{-6} for the final source identification. The default wavelet scales of 2 and 4 pixels were also maintained. The default significance threshold of 3 for the SNR was kept for celldetect. These default values are sufficient for our purposes (detection of a point source and its neighbours) as they have been well chosen for use with Chandra ACIS data.

Neither wavdetect nor celldetect found any source at all in either observation, suggesting any X-ray emission from ϕ Per to be very weak, if it exists at all.

5.3.2 Count rates and luminosities

The net count rates were obtained using a circle for the source region and an annulus for the background region. As no sources had been detected by wavdetect and celldetect, the

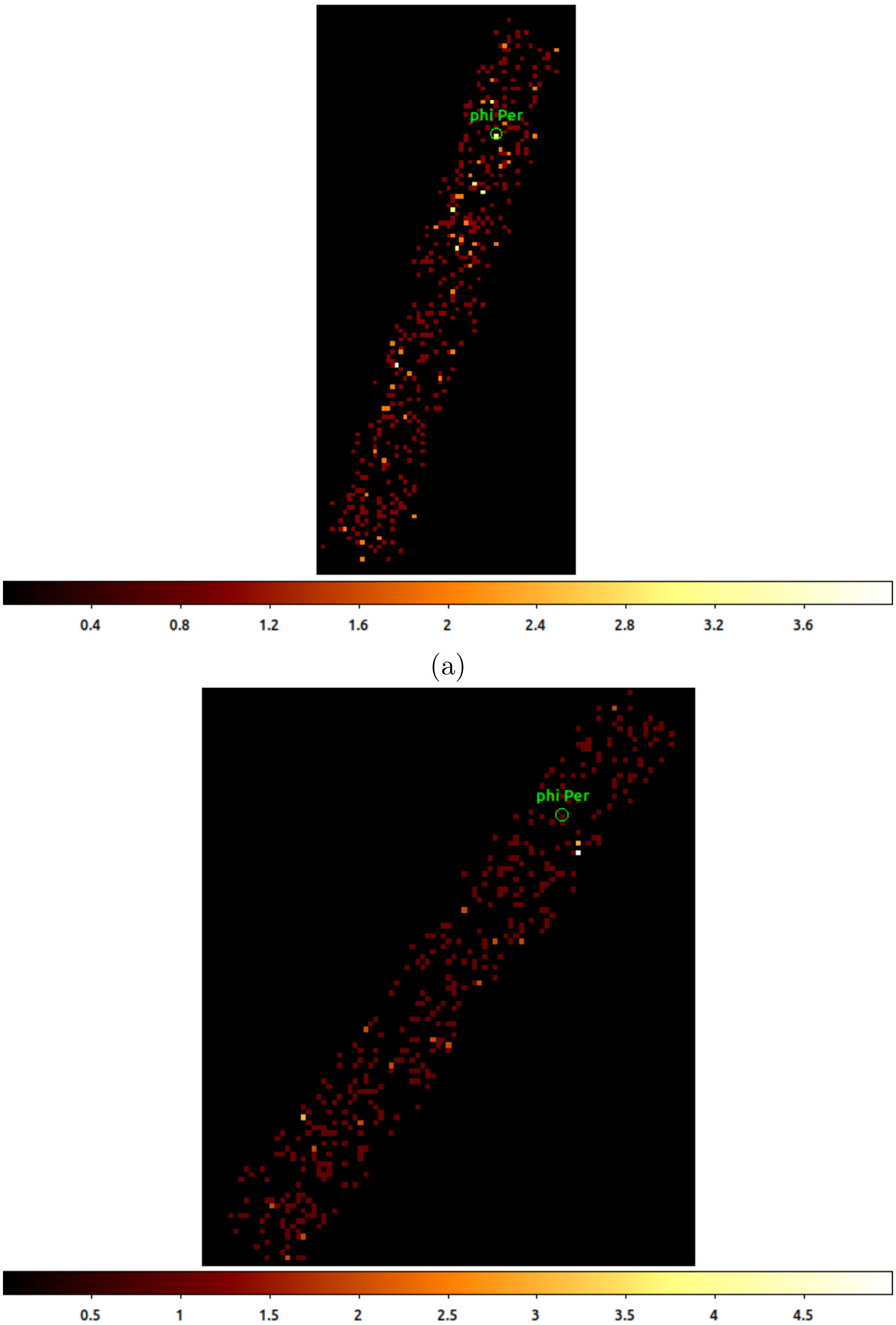

(a)

(b)

Figure 52: Exposure-corrected images for July (top) and August (bottom), highlighting the position of ϕ Per by a circle of 5" radius.

confidence interval (used to find the upper limit) was initially set to 95%. Trials with different sizes were performed knowing that the typical radius of the (1 keV) on-axis spatial PSF of ACIS is 2" (90% ECF) i.e. 4 pixels. The source region should be larger than this value, in order to encompass most of the PSF size (especially since the PSF size increases with energy). However should the source region be too large, it will be prone to contamination from unrelated sources. The background region should be large enough to properly estimate the background counts, but at the risk of also being contaminated by unrelated sources. Ultimately, four aperture sizes we chosen, noted as (inner aperture radius, outer aperture radius): (5",15"), (10",30"), (15",35") and (20",40"). These aperture sizes are shown on Figure 53. The net count rates and X-ray luminosities for each aperture are shown in table 20.

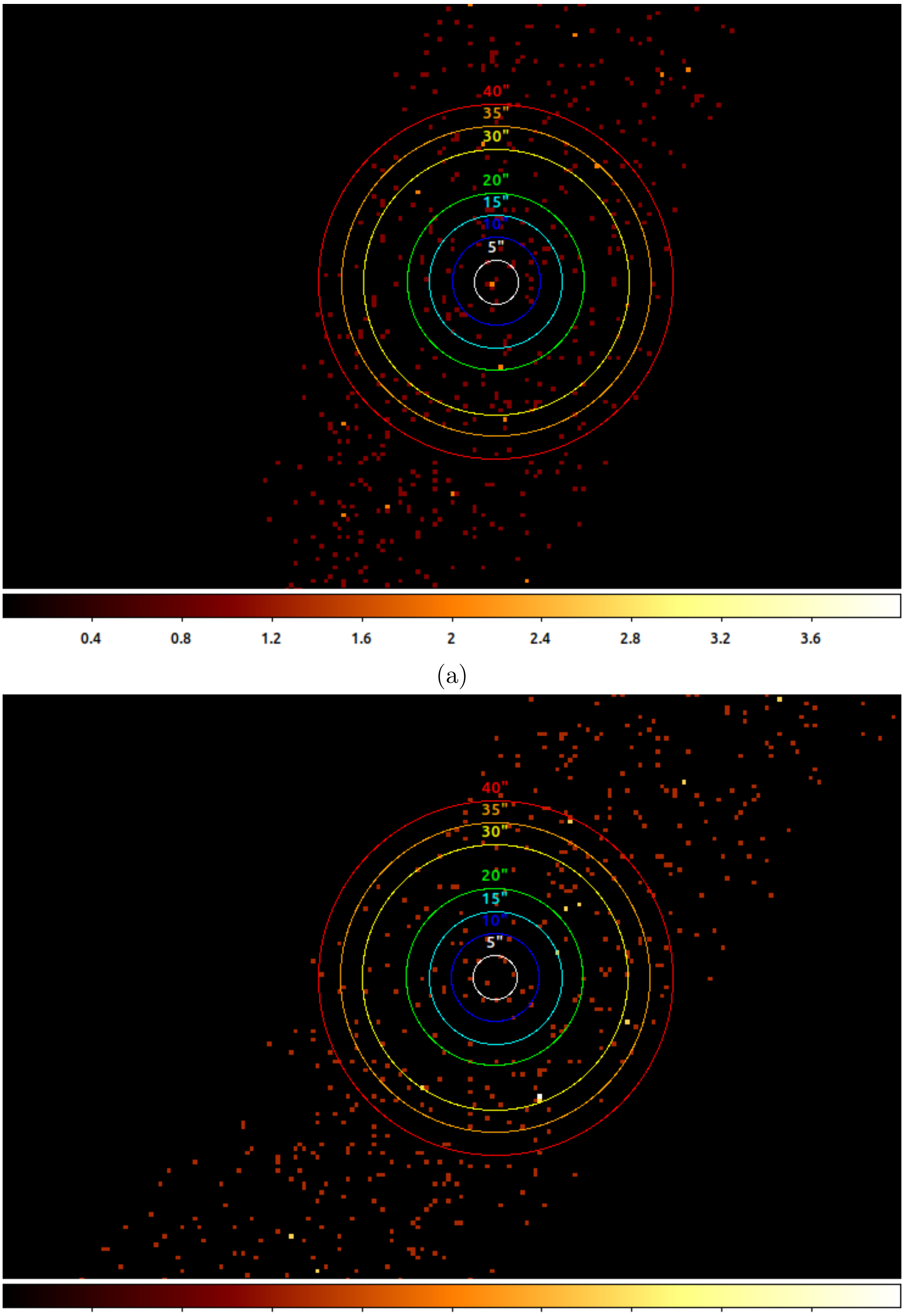

(a)

(b)

Figure 53: Apertures in July (top) and August (bottom)

Aperture sizes	Count rates (10^{-3} cts/s)			$\text{Log}(L_X/L_{BOL})$ (merged)				
	July	August	Merged	$log(T) = 6.4$	6.85	7.45	7.8	8.5
Non-detections								
(10",30")	< 2.17	< 2.23	< 1.42	< -7.8	< -8.4	< -8.8	< -8.7	< -8.7
(15",35")	< 3.50	< 1.93	< 1.73	< -7.7	< -8.3	<- 8.7	< -8.6	< -8.6
(20",40")	< 5.16	< 3.15	< 3.00	< -7.4	< -8.1	< -8.6	< -8.4	< -8.4
Marginal detection								
(5",15")	< 2.05	< 2.79	0.77 ± 0.50	< -8.0 ± 0.3	< -8.7 ± 0.3	< -9.1 ± 0.3	< -9.0 ± 0.3	< -8.9± 0.3

Table 20: Net count rates and X-ray to bolometric luminosity ratios for various aperture sizes. The results for non-detections are all 95% upper limits. The error bars for the marginal merged detection were obtained using a 68% confidence interval. The bolometric luminosity of ϕ Per ($log\,(L_{Bol}/L_{\odot}) = 4.16 \pm 0.04$) was obtained from [27].

5.3.3 Individual net count rates

Srcflux failed to detect any emission for either observation regardless of the aperture, instead returning the 95% confidence interval upper limits.

As both observations were carried out with similar durations and with an identical set up, one would expect the count rate upper limits to be similar between the two observations. While this appears to be the case for (10",30") and (5",15"), with both having upper limits in the 2 10^{-3} to 3 10^{-3} cts/s range, this is not the case for (15",35") and (20",40"). They instead present upper limits of 3.50 10^{-3} (July) and 1.93 10^{-3} (August) for the former and 5.16 10^{-3} (July) and 3.15 10^{-3} (August) for the latter. A possible cause for this discrepancy may be the larger aperture sizes as they could lead to contamination in either the source or the background region (or both). Looking at Figure 53, we find that for both aperture sizes, the source region contains more X-ray counts in the July observation than in the August observation. Conversely, the background region contains more X-ray counts in August than in July. The combination of a stronger source yet weaker background in July compared to August may explain the higher upper limit observed for the former. However, as we previously did not detect any X-ray source, we cannot conclusively attribute this discrepancy to a specific contamination in either observation.

5.3.4 Merged net count rates

The merged upper limits are smaller than those of the single observations for all aperture sizes, being $\sim$ 70% of the averaged count rates of both observations. This is not unexpected however when considering the signal to noise ratio: the SNR increases by a factor of $\sqrt{2}$ when merging two identical datasets, since while the number of source photons double, the noise increases by a factor of $\sqrt{2}$. This results in the merged upper limit being $\frac{1}{\sqrt{2}} \sim 70\%$ of the individual observations limits.

ϕ Per appears to be detected for the smallest aperture size, (5",15") but only at a 95% confidence interval (2σ). In order to obtain the 1σ error, the measurement was repeated at a confidence interval of 68%, giving us a net count rate for this detection of $(0.77 \pm 0.50)\,10^{-3}$ cts/s. This count rate (and therefore the luminosity range) agrees with the upper limits obtained by all three of the other apertures. While this may seem promising, we must remember that it was detected only at a 2σ confidence interval. This alongside the fact that no sources were found using the wavdetect and celldetect tools makes this detection marginal at best.

Three ranges of upper limits for L_X/L_{BOL} were obtained from the merged count rates. The three ranges overlap, with the (10",30") range having the smallest lower bound and conversely the (20",40") having the largest upper bound. Because of the probable contamination in the (15",35") and (20",40") apertures (Section 5.3.3), we will use the (10",30") range as our final upper limit value.

5.3.5 Discussion

Our final upper limit for L_X/L_{BOL} thus ranges from $log\,(L_X/L_{BOL}) < -8.8$ to -7.8 depending on the temperature of the emitting plasma. This result can be compared with Nazé et al's (2022)[27]. They used three values of kT for converting their count rates (0.2 keV , 0.6 keV and 5.4 keV). We restricted our result to this range, giving us $log\,(L_X/L_{BOL}) < -8.7$ to -7.8. Nazé et al (2022) similarly did not detect any emission from ϕ Per and calculated an upper limit in the 0.5-10 keV range of $\log(L_X/L_{BOL}) < -7.5$ to -7.3, using data from the Neil Gehrels Swift Observatory's XRT instrument [27]. The Chandra upper limit is an order of magnitude smaller than the Swift data, further constraining the level of X-ray emission from ϕ Per. Comparing the Swift and Chandra observations, one finds the Swift observation had a combined exposure of 4545 s [27], roughly half of the combined length of the Chandra observations (4960 s and 4865 s). The combined Chandra observations being double the length of the Swift observation cannot be the sole cause of the more constrained results, as the Chandra upper limit would be $\sim \frac{1}{\sqrt{2}} \times$ the Swift limit, as seen with the individual and merged Chandra observations (see Section 5.3.4).

From an instrumental point of view however, we find that Chandra is significantly more sensitive in the chosen X-ray range than Swift. This can be seen when comparing their effective areas, i.e. an X-ray telescope's reduced geometric area when taking into account its reflectivity, detector efficiency and off-axis vignetting, all of which are dependent on energy [54]. When comparing the two telescopes, we find that the ACIS-S effective area is indeed larger than that of the XRT (see Figure 54) This larger area allows for greater sensitivity, thus leading to the lower upper limit obtained.

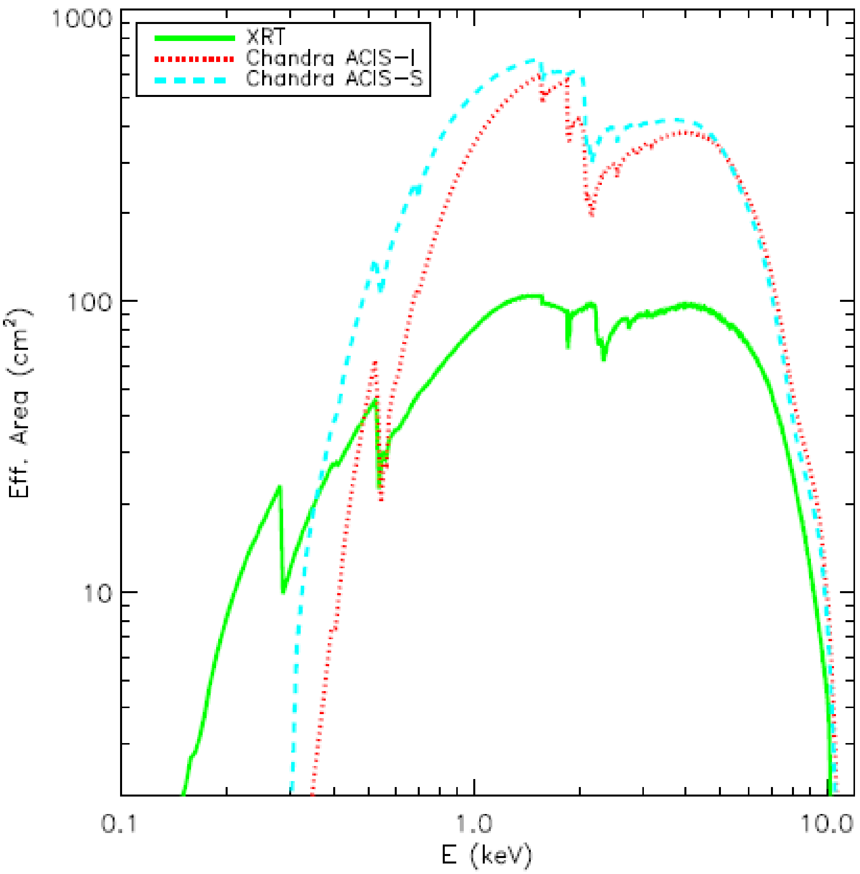

Figure 54: Comparison of the effective areas of the Chandra ACIS instrument and the Swift XRT instrument. From [48].

The lack of detection for both individual observations despite their different orbital phases (0.0 and 0.25) allows us to draw some conclusions. If the X-ray emission arose from a wind-wind collision or a disk-wind collision between the two stars, it would vary with the orbital phase due to changing absorption along the line of sight [36]. In the case of ϕ Per, it would reach a maximum at phase 0.75 (when the sdO is between us and the Be) and a minimum at phase 0.25 (when the Be is in front of its companion), as the Be's wind and disk would absorb part of the emission. Therefore if the emission were phase locked, one would expect it to be stronger during the July observation (phase 0.0) than during the August observation (phase 0.25). However neither were detected, indicating that there was no huge change in brightness. Therefore we will assume limited changes or constancy of the emission as a function of phase.

All in all, the Chandra observations have reinforced the conclusion that ϕ Per's X-ray emission is very faint, with the upper limit of the emission being an order of magnitude lower than previous results. The emission upper limit does not appear to vary much with the orbital phase, thus disfavouring any emission process involving the companion (such as a colliding winds scenario). It is also an order of magnitude fainter than the X-ray emission which arises from shocks in the winds of early-type massive stars, $log\,(L_X/L_{BOL}) \sim -7$ [27]. However this relation between bolometric and X-ray luminosity breaks down for stars later than B1 with no clear correlation for these later stars [35]. As ϕ Per's spectral type is B1.5 Ve [42], the possibility that its lower luminosity X-ray emission arises from collisions in the primary's wind cannot be ruled out. Finally, while the sole detection remains marginal, it agrees with the luminosities of detected Be + sdO binaries, such as HD 157042 ($\log(L_X/L_{BOL}) = -8.56 \pm 0.01$) or HD 43544 ($\log(L_X/L_{BOL}) = -8.08 \pm 0.01$) [27].

6 Conclusion

In this work, we have investigated the emissions of ϕ Per in the optical and X-ray domains, utilizing 178 Hα spectra from amateur astronomers as well as two Chandra observations.

In the optical domain, our goal was to determine a new orbital solution for the system based on radial velocity measurements of the Hα line profile. The line profile was found to be highly variable, necessitating the use of the Gaussian method to mitigate the strong variation of the line core by only sampling the wings of the line profile. Despite this, the initial orbital solution obtained was found to be still strongly affected by line profile variations from the inner disk. To mitigate this, orbital solutions were calculated over smaller time spans during which the line appears quite stable. Ultimately, a new orbital solution was successfully found. Unfortunately, the line profile variation may affect any orbital solution solely derived from disk lines such as Hα.

In X-rays, an initial search for sources failed to find any significant emission from ϕ Per. A method analogous to aperture photometry was then used to obtain an upper limit on its X-ray luminosity. Testing with multiple aperture sizes, we found the upper limit to be an order of magnitude lower than the past results [27] confirming that ϕ Per's X-ray emission is very faint. In addition, the lack of detection at either observation date indicates that the emission likely did not vary despite the difference in phase of the two observations (0.0 and 0.25). This suggests that no emission mechanism linked to the presence of a companion is at play in ϕ Per. Finally, it should be noted that the smallest aperture size did lead to a marginal detection, when both datasets were combined. This could indicate that the X-ray emission from ϕ Per lies just beyond the sensitivity of current observations. Future observations would be required in order to confirm this conclusion. A potential avenue for this could be merging more data sets than the two utilised in this work, in order to further increase the signal-to-noise ratio. Fortunately, more data from ϕ Per is expected in the coming months.

References

[1] S. J. Adelman, A. F. Gulliver, and D. E. Holmgren. Telluric Lines. In *M.A.S.S., Model Atmospheres and Spectrum Synthesis*, volume 108 of *Astronomical Society of the Pacific Conference Series*, page 293, January 1996.

[2] C. A. L. Bailer-Jones, J. Rybizki, M. Fouesneau, M. Demleitner, and R. Andrae. Estimating Distances from Parallaxes. V. Geometric and Photogeometric Distances to 1.47 Billion Stars in Gaia Early Data Release 3. , 161(3):147, March 2021.

[3] J. E. Bjorkman and J. P. Cassinelli. Equatorial Disk Formation around Rotating Stars Due to Ram Pressure Confinement by the Stellar Wind. *Astrophysical Journal*, 409:429, May 1993.

[4] H. Bozic, P. Harmanec, J. Horn, P. Koubsky, G. Scholz, D. McDavid, A. M. Hubert, and H. Hubert. Toward a consistent model of the B0.5IVe + sdO binary φ Persei. *Astronomy and Astrophysics*, 304:235, December 1995.

[5] A. C. Carciofi. The circumstellar discs of Be stars. In *Active OB Stars: Structure, Evolution, Mass Loss, and Critical Limits*, volume 272, pages 325–336, July 2011.

[6] A. C. Carciofi, A. T. Okazaki, J. B. Le Bouquin, S. Štefl, Th. Rivinius, D. Baade, J. E. Bjorkman, and C. A. Hummel. Cyclic variability of the circumstellar disk of the Be star ζ Tauri. II. Testing the 2D global disk oscillation model. *Astronomy and Astrophysics*, 504(3):915–927, September 2009.

[7] J. P. Cassinelli, J. C. Brown, M. Maheswaran, N. A. Miller, and D. C. Telfer. A Magnetically Torqued Disk Model for Be Stars. *Astrophysical Journal*, 578(2):951–966, October 2002.

[8] S. R. Cranmer and S. P. Owocki. The Effect of Oblateness and Gravity Darkening on the Radiation Driving in Winds from Rapidly Rotating B Stars. *Astrophysical Journal*, 440:308, February 1995.

[9] D. R. Gies, Jr. Bagnuolo, W. G., E. K. Baines, T. A. ten Brummelaar, C. D. Farrington, P. J. Goldfinger, E. D. Grundstrom, W. Huang, H. A. McAlister, A. Mérand, J. Sturmann, L. Sturmann, Y. Touhami, N. H. Turner, D. W. Wingert, D. H. Berger, M. V. McSwain, J. P. Aufdenberg, S. T. Ridgway, A. L. Cochran, D. F. Lester, N. C. Sterling, J. E. Bjorkman, K. S. Bjorkman, and P. Koubský. CHARA Array K'-Band Measurements of the Angular Dimensions of Be Star Disks. *Astrophysical Journal*, 654(1):527–543, January 2007.

[10] D. R. Gies, Jr. Bagnuolo, W. G., E. C. Ferrara, A. B. Kaye, M. L. Thaller, L. R. Penny, and G. J. Peters. Hubble Space Telescope Goddard High Resolution Spectrograph Observations of the Be + sdO Binary φ Persei. *Astrophysical Journal*, 493(1):440–450, January 1998.

[11] E. D. Grundstrom and D. R. Gies. Estimating Be Star Disk Radii using Hα Emission Equivalent Widths. *Astrophysical Journal, Letters*, 651(1):L53–L56, November 2006.

[12] S. B. Gudennavar, S. G. Bubbly, K. Preethi, and Jayant Murthy. A Compilation of Interstellar Column Densities. *Astrophysical Journal, Supplement*, 199(1):8, March 2012.

[13] R. W. Hanuschik. On the structure of Be star disks. *Astronomy and Astrophysics*, 308:170–179, April 1996.

[14] K. Hinkle, L. Wallace, J. Valenti, and D. Harmer. *Visible and Near Infrared Atlas of the Arcturus Spectrum 3727-9300 Å*. 2000.

[15] W. Hummel and M. Vrancken. Non-axisymmetric Be star circumstellar disks. *Astronomy and Astrophysics*, 302:751, October 1995.

[16] W. Hummel and S. Štefl. The circumstellar structure of the Be shell star φ Persei. II. Modeling. *Astronomy and Astrophysics*, 368:471–483, March 2001.

[17] J. A. Kennea, M. J. Coe, P. A. Evans, L. J. Townsend, Z. A. Campbell, and A. Udalski. Swift J011511.0-725611: discovery of a rare Be star/white dwarf binary system in the SMC. *Monthly Notices of the RAS*, 508(1):781–788, November 2021.

[18] S. Kraus, J. D. Monnier, X. Che, G. Schaefer, Y. Touhami, D. R. Gies, J. P. Aufdenberg, F. Baron, N. Thureau, T. A. ten Brummelaar, H. A. McAlister, N. H. Turner, J. Sturmann, and L. Sturmann. Gas Distribution, Kinematics, and Excitation Structure in the Disks around the Classical Be Stars β Canis Minoris and ζ Tauri. *Astrophysical Journal*, 744(1):19, January 2012.

[19] S. Kriz and P. Harmanec. A Hypothesis of the Binary Origin of Be Stars. *Bulletin of the Astronomical Institutes of Czechoslovakia*, 26:65, January 1975.

[20] M. Maintz, Th. Rivinius, S. Štefl, and O. Stahl. How Frequent is Evolutionary Spin-Up in Binary Be Stars? In *Stellar Rotation*, volume 215, page 95, June 2004.

[21] R. G. Martin, J. E. Pringle, C. A. Tout, and S. H. Lubow. Tidal warping and precession of Be star decretion discs. *Monthly Notices of the Royal Astronomical Society*, 416(4):2827–2839, 09 2011.

[22] G. Meynet, S. Ekström, A. Maeder, and F. Barblan. Initial Conditions for Reaching Critical Velocity. In *Active OB-Stars: Laboratories for Stellare and Circumstellar Physics*, volume 361 of *Astronomical Society of the Pacific Conference Series*, page 325, March 2007.

[23] J. Morrison. Chapter 1 - the wave-particle duality. In *Modern Physics with Modern Computational Methods (Third Edition)*, pages 1–17. Academic Press, third edition edition, 2021.

[24] D. Mourard, J. D. Monnier, A. Meilland, D. Gies, F. Millour, M. Benisty, X. Che, E. D. Grundstrom, R. Ligi, G. Schaefer, F. Baron, S. Kraus, M. Zhao, E. Pedretti, P. Berio, J. M. Clausse, N. Nardetto, K. Perraut, A. Spang, P. Stee, I. Tallon-Bosc, H. McAlister, T. ten Brummelaar, S. T. Ridgway, J. Sturmann, L. Sturmann, N. Turner, and C. Farrington. Spectral and spatial imaging of the Be+sdO binary ϕ Persei. *Astronomy and Astrophysics*, 577:A51, May 2015.

[25] P. Munar-Adrover, J. M. Paredes, M. Ribó, K. Iwasawa, V. Zabalza, and J. Casares. Discovery of X-Ray Emission from the First Be/Black Hole System. *Astrophysical Journal, Letters*, 786(2):L11, May 2014.

[26] Y. Nazé, G. Rauw, S. Czesla, M. A. Smith, and J. Robrade. Velocity monitoring of γ Cas stars reveals their binarity status. *Monthly Notices of the RAS*, 510(2):2286–2304, February 2022.

[27] Y. Nazé, G. Rauw, M. A. Smith, and C. Motch. The X-ray emission of Be+stripped star binaries. *Monthly Notices of the RAS*, 516(3):3366–3380, November 2022.

[28] A. T. Okazaki. Long-Term V/R Variations of Be Stars Due to Global One-Armed Oscillations of Equatorial Disks. , 43:75–94, February 1991.

[29] S. Owocki and A. Ud-Doula. Magnetic Spin-Up of Line-Driven Stellar Winds. In *Magnetic Fields in O, B and A Stars: Origin and Connection to Pulsation, Rotation and Mass Loss*, volume 305 of *Astronomical Society of the Pacific Conference Series*, page 350, January 2003.

[30] O. R. Pols, J. Cote, L. B. F. M. Waters, and J. Heise. The formation of Be stars through close binary evolution. *Astronomy and Astrophysics*, 241:419, January 1991.

[31] J. M. Porter. Continuum IR emission of Be star wind-compressed discs. *Astronomy and Astrophysics*, 324:597–605, August 1997.

[32] J. M. Porter and T. Rivinius. Classical Be Stars. *Publications of the ASP*, 115(812):1153–1170, October 2003.

[33] K. Postnov, L. Oskinova, and J. M. Torrejón. A propelling neutron star in the enigmatic Be-star γ Cassiopeia. *Monthly Notices of the RAS*, 465(1):L119–L123, February 2017.

[34] A. Quirrenbach, D. F. Buscher, D. Mozurkewich, C. A. Hummel, and J. T. Armstrong. Maximum-entropy maps of the Be shell star dzeta Tauri from optical long-baseline interferometry. *Astronomy and Astrophysics*, 283:L13–L16, March 1994.

[35] G. Rauw. X-Ray Emission of Massive Stars and Their Winds. In *Handbook of X-ray and Gamma-ray Astrophysics*, page 108. 2022.

[36] G. Rauw and Y. Nazé. X-ray emission from interacting wind massive binaries: A review of 15 years of progress. *Advances in Space Research*, 58(5):761–781, September 2016.

[37] P. Reig. Be/X-ray binaries. *Astronomy and Astrophysics, Supplement*, 332(1):1–29, March 2011.

[38] T. Rivinius, A. C. Carciofi, and Christophe Martayan. Classical Be stars. Rapidly rotating B stars with viscous Keplerian decretion disks. *Astronomy and Astrophysics Reviews*, 21:69, October 2013.

[39] S. M. Saad, M. A. Hamdy, and M. S. Abolazm. An overview investigation of Be/Shell stars. *NRIAG Journal of Astronomy and Geophysics*, 1(2):97–105, December 2012.

[40] B. E. Sabogal, K. Y. Ubaque, A. García-Varela, M. Álvarez, and L. Salas. Evidence of Dissipation of Circumstellar Disks from L-band Spectra of Bright Galactic Be Stars. *Publications of the ASP*, 129(971):014203, January 2017.

[41] D. P. Schneider and P. Young. The magnetic maw of 2A 0311-22.7. *Astrophysical Journal*, 238:946–954, June 1980.

[42] A. Schootemeijer, Y. Götberg, S. E. de Mink, D. Gies, and E. Zapartas. Clues about the scarcity of stripped-envelope stars from the evolutionary state of the sdO+Be binary system φ Persei. *Astronomy and Astrophysics*, 615:A30, July 2018.

[43] A. W. Shafter. On Measuring the Radial Velocity of White Dwarfs in Cataclysmic Binaries. In *Cataclysmic Variables and Low-Mass X-ray Binaries*, page 355, January 1985.

[44] A. W. Shafter, P. Szkody, and J. R. Thorstensen. X-Ray and Optical Observations of the Ultrashort Period Dwarf Nova SW Ursae Majoris: A Likely New DQ Herculis Star. *Astrophysical Journal*, 308:765, September 1986.

[45] Y. Shao and X.D. Li. On the Formation of Be Stars through Binary Interaction. *Astrophysical Journal*, 796(1):37, November 2014.

[46] S. N. Shore. Star clusters. In *Encyclopedia of Physical Science and Technology (Third Edition)*, pages 715–726. Academic Press, New York, third edition edition, 2003.

[47] T. A. A. Sigut and P. Patel. The Correlation between Hα Emission and Visual Magnitude during Long-term Variations in Classical Be Stars. , 765(1):41, March 2013.

[48] E. Tundo, A. Moretti, P. Tozzi, L. Teng, P. Rosati, G. Tagliaferri, and S. Campana. The Swift X-ray Telescope Cluster Survey: data reduction and cluster catalog for the GRB fields. *Astronomy and Astrophysics*, 547, 08 2012.

[49] A. ud-Doula, S. P. Owocki, and N. D. Kee. Disruption of circumstellar discs by large-scale stellar magnetic fields. *Monthly Notices of the RAS*, 478(3):3049–3055, August 2018.

[50] S. Štefl, A. T. Okazaki, T. Rivinius, and D. Baade. V/R Variations of Binary Be Stars. In *Active OB-Stars: Laboratories for Stellare and Circumstellar Physics*, volume 361 of *Astronomical Society of the Pacific Conference Series*, page 274, March 2007.

[51] J. Zorec and D. Briot. Critical study of the frequency of Be stars taking into account their outstanding characteristics. *Astronomy and Astrophysics*, 318:443–460, February 1997.

Webography

[52] Chandra X-ray Center. The Detect Reference Manual. https://cxc.harvard.edu/ciao/download/doc/detect_manual/manual.html, 2006. Accessed: 2023-05-25.

[53] Chandra X-ray Center. Chandra Instruments and Calibration. https://cxc.harvard.edu/cal/, 2019. Accessed: 2023-05-20.

[54] Chandra X-ray Center. Chandra Interactive Analysis of Observations. https://cxc.cfa.harvard.edu/ciao4.15/, 2019. Accessed: 2023-05-25.

[55] Chandra X-ray Center. Chandra X-ray Observatory. https://chandra.harvard.edu/, 2019. Accessed: 2023-06-24.

[56] Chandra X-ray Center. The Chandra X-ray Observatory. https://cxc.harvard.edu/cdo/about_chandra/overview_cxo.html, 2019. Accessed: 2023-05-20.

[57] Chandra X-ray Center. The Chandra Proposers' Observatory Guide. https://cxc.harvard.edu/proposer/POG/html/index.html, 2022. Accessed: 2023-05-20.

[58] European Southern Observatory. ESO-MIDAS User's Guide Volume B. https://www.eso.org/sci/software/esomidas/doc/user/18NOV/volb/index.html, 1999. Accessed: 2023-03-25.

[59] NASA. Chandra Returns to Full Science Operations. https://www.nasa.gov/mission_pages/chandra/news/update-on-chandra-x-ray-observatory-anomaly.html, 2020. Accessed: 2023-05-20.

[60] NASA HEASARC. webPIMMS. https://heasarc.gsfc.nasa.gov/cgi-bin/Tools/w3pimms/w3pimms.pl, 2014. Accessed: 2023-05-25.

[61] National Optical Astronomy Observatories. IRAF Newsletter – Number 14 – April 1998. http://iraf.nao.ac.jp/irafnews/apr98/irafnews.html, 1998. Accessed: 2023-03-25.

A Appendix: Radial velocities

This appendix lists the radial velocities obtained for Fit 1, Fit 2 and Fit 3 in Tables 21, 22 and 23. The radial velocities for the single year and stable interval fits are listed in A.1 and A.2 respectively. The error values correspond to each solution's RMS deviation.

Table 21

Radial velocities for Fit 1		
Date (HJD-2450000)	Phase	Radial velocity (km/s)
2237.4	0.4	-8.4 ± 8.2
2241.4	0.5	-13.4 ± 8.2
2253.4	0.6	-7.2 ± 8.2
2263.3	0.7	-7.6 ± 8.2
2284.3	0.8	-24.6 ± 8.2
2293.3	0.9	-26.4 ± 8.2
2303.3	1.0	-39.6 ± 8.2
2521.4	0.7	7.1 ± 8.2
2854.5	0.3	2.9 ± 8.2
2855.5	0.3	-1.1 ± 8.2
2857.6	0.3	1.9 ± 8.2
2915.5	0.8	-22.8 ± 8.2
3231.5	0.3	-8.0 ± 8.2
3232.7	0.3	-6.7 ± 8.2
3244.5	0.4	0.6 ± 8.2
3271.5	0.6	-5.1 ± 8.2
3301.5	0.8	-18.6 ± 8.2
3330.3	0.1	-27.7 ± 8.2
3962.6	0.1	-23.9 ± 8.2
4331.5	1.0	-21.0 ± 8.2
4358.5	0.2	-21.8 ± 8.2
4387.3	0.4	6.4 ± 8.2
4393.5	0.5	8.4 ± 8.2
4513.4	0.4	2.0 ± 8.2
4672.7	0.7	6.9 ± 8.2
4706.5	0.9	-23.7 ± 8.2
4793.5	0.6	8.2 ± 8.2
4866.3	0.2	-38.4 ± 8.2
5059.5	0.7	-18.2 ± 8.2
5060.6	0.7	-19.5 ± 8.2

Continuation of Table 21		
Date (HJD-2450000)	Phase	Radial velocity (km/s)
5067.5	0.8	-25.8 ± 8.2
5071.5	0.8	-26.1 ± 8.2
5072.4	0.8	-26.4 ± 8.2
5109.5	0.1	-30.0 ± 8.2
5117.4	0.2	-29.3 ± 8.2
5119.4	0.2	-31.4 ± 8.2
5203.4	0.9	-33.2 ± 8.2
5238.3	0.1	-37.4 ± 8.2
5270.3	0.4	-15.1 ± 8.2
5398.5	0.4	1.6 ± 8.2
5417.5	0.5	8.8 ± 8.2
5418.5	0.6	5.4 ± 8.2
5455.4	0.8	-17.7 ± 8.2
5534.3	0.5	-3.9 ± 8.2
5559.4	0.7	1.0 ± 8.2
5774.6	0.4	2.0 ± 8.2
5775.6	0.4	-1.6 ± 8.2
5777.5	0.4	-1.7 ± 8.2
5785.6	0.5	3.7 ± 8.2
5828.4	0.8	-10.8 ± 8.2
5831.5	0.8	-20.8 ± 8.2
5857.4	0.0	-33.0 ± 8.2
5879.7	0.2	-10.1 ± 8.2
5907.6	0.4	9.2 ± 8.2
5956.3	0.8	-12.2 ± 8.2
6143.6	0.3	-0.4 ± 8.2
6150.4	0.3	0.2 ± 8.2
6163.4	0.4	16.7 ± 8.2
6167.5	0.5	10.6 ± 8.2
6180.3	0.6	21.7 ± 8.2
6204.6	0.8	5.6 ± 8.2
6206.4	0.8	5.3 ± 8.2
6260.5	0.2	-6.9 ± 8.2
6267.3	0.3	0.2 ± 8.2
6270.5	0.3	17.9 ± 8.2
6291.4	0.4	20.4 ± 8.2
6301.4	0.5	27.1 ± 8.2

Continuation of Table 21		
Date (HJD-2450000)	Phase	Radial velocity (km/s)
6490.5	0.0	-15.8 ± 8.2
6556.4	0.5	27.0 ± 8.2
6628.6	0.1	-16.0 ± 8.2
6665.6	0.4	15.1 ± 8.2
6874.6	0.0	-22.8 ± 8.2
6926.5	0.5	11.9 ± 8.2
6956.4	0.7	0.7 ± 8.2
6960.4	0.7	-4.8 ± 8.2
6961.4	0.7	-4.6 ± 8.2
7327.4	0.6	0.7 ± 8.2
7345.4	0.8	-11.0 ± 8.2
7364.3	0.9	-26.9 ± 8.2
7617.6	0.9	-25.8 ± 8.2
7638.5	0.1	-39.1 ± 8.2
7666.4	0.3	-19.4 ± 8.2
7671.5	0.3	-13.1 ± 8.2
7693.4	0.5	1.9 ± 8.2
7713.6	0.7	-12.4 ± 8.2
7793.6	0.3	-12.9 ± 8.2
7989.5	0.8	-21.8 ± 8.2
7999.5	0.9	-27.3 ± 8.2
8017.4	0.1	-31.5 ± 8.2
8018.5	0.1	-31.8 ± 8.2
8034.6	0.2	-21.4 ± 8.2
8041.4	0.3	-16.4 ± 8.2
8041.4	0.3	-11.3 ± 8.2
8057.6	0.4	-11.3 ± 8.2
8072.4	0.5	-7.5 ± 8.2
8073.4	0.5	-4.4 ± 8.2
8073.4	0.5	-9.4 ± 8.2
8077.3	0.5	-4.0 ± 8.2
8078.5	0.6	-3.4 ± 8.2
8085.3	0.6	-11.3 ± 8.2
8092.3	0.7	-15.1 ± 8.2
8094.3	0.7	-18.4 ± 8.2
8094.6	0.7	-7.7 ± 8.2
8100.3	0.7	-19.8 ± 8.2

Continuation of Table 21		
Date (HJD-2450000)	Phase	Radial velocity (km/s)
8106.5	0.8	-21.1 ± 8.2
8133.3	1.0	-33.5 ± 8.2
8133.5	1.0	-28.7 ± 8.2
8142.3	0.1	-34.2 ± 8.2
8147.4	0.1	-34.0 ± 8.2
8158.4	0.2	-23.9 ± 8.2
8159.7	0.2	-31.4 ± 8.2
8162.3	0.2	-21.5 ± 8.2
8177.3	0.3	-6.8 ± 8.2
8328.6	0.5	-1.8 ± 8.2
8329.6	0.5	-2.8 ± 8.2
8333.6	0.6	-2.7 ± 8.2
8339.6	0.6	-5.4 ± 8.2
8345.4	0.7	-10.6 ± 8.2
8352.4	0.7	-10.7 ± 8.2
8364.4	0.8	-6.1 ± 8.2
8377.5	0.9	-30.8 ± 8.2
8388.3	1.0	-34.3 ± 8.2
8412.3	0.2	-25.6 ± 8.2
8414.5	0.2	-23.3 ± 8.2
8428.6	0.3	-7.3 ± 8.2
8449.6	0.5	1.5 ± 8.2
8466.8	0.6	2.2 ± 8.2
8468.6	0.6	-4.1 ± 8.2
8472.7	0.7	-5.2 ± 8.2
8487.6	0.8	-23.9 ± 8.2
8500.7	0.9	-34.4 ± 8.2
8505.7	0.9	-36.7 ± 8.2
8521.7	0.0	-33.5 ± 8.2
8526.6	0.1	-31.2 ± 8.2
8542.6	0.2	-19.8 ± 8.2
8557.6	0.3	-4.8 ± 8.2
8560.6	0.4	-3.6 ± 8.2
8567.7	0.4	2.4 ± 8.2
8574.7	0.5	-0.4 ± 8.2
8706.6	0.5	12.2 ± 8.2
8718.7	0.6	-1.0 ± 8.2

Continuation of Table 21		
Date (HJD-2450000)	Phase	Radial velocity (km/s)
8726.6	0.7	-7.5 ± 8.2
8730.6	0.7	-14.2 ± 8.2
8730.6	0.7	-8.3 ± 8.2
8731.6	0.7	-13.0 ± 8.2
8732.6	0.7	-12.8 ± 8.2
8738.5	0.8	-17.8 ± 8.2
8738.5	0.8	-21.1 ± 8.2
8742.5	0.8	-25.5 ± 8.2
8743.6	0.8	-29.0 ± 8.2
8746.5	0.8	-29.7 ± 8.2
8755.5	0.9	-35.7 ± 8.2
8757.5	0.9	-34.4 ± 8.2
8762.5	1.0	-38.4 ± 8.2
8764.5	1.0	-35.3 ± 8.2
8766.5	1.0	-37.1 ± 8.2
8768.5	1.0	-37.3 ± 8.2
8769.5	0.0	-34.6 ± 8.2
8770.5	0.0	-36.4 ± 8.2
8782.5	0.1	-29.1 ± 8.2
8783.5	0.1	-27.2 ± 8.2
8794.4	0.2	-24.5 ± 8.2
8846.3	0.6	-0.4 ± 8.2
8865.4	0.8	-28.0 ± 8.2
9051.5	0.2	-19.2 ± 8.2
9076.5	0.4	-5.7 ± 8.2
9097.5	0.6	-3.5 ± 8.2
9100.6	0.6	-4.8 ± 8.2
9101.6	0.6	-6.4 ± 8.2
9106.4	0.7	-6.6 ± 8.2
9110.5	0.7	-4.3 ± 8.2
9115.5	0.7	-8.9 ± 8.2
9329.3	0.4	1.4 ± 8.2
9481.4	0.6	3.1 ± 8.2
9496.4	0.7	-6.1 ± 8.2
9515.4	0.9	-23.0 ± 8.2
9567.3	0.3	-10.7 ± 8.2
9863.3	0.6	-0.5 ± 8.2

Table 22

Radial velocities for Fit 2		
Date (HJD-2450000)	Phase	Radial velocity (km/s)
2237.4	0.5	-13.9 ± 10.2
2241.4	0.5	-18.7 ± 10.2
2253.4	0.6	-13.7 ± 10.2
2263.3	0.7	-10.5 ± 10.2
2284.3	0.8	-26.4 ± 10.2
2293.3	0.9	-25.3 ± 10.2
2303.3	1.0	-36.1 ± 10.2
2521.4	0.7	2.0 ± 10.2
2854.5	0.3	7.0 ± 10.2
2855.5	0.4	4.1 ± 10.2
2857.6	0.4	7.3 ± 10.2
2915.5	0.8	-9.5 ± 10.2
3231.5	0.3	5.8 ± 10.2
3232.7	0.3	5.7 ± 10.2
3244.5	0.4	11.9 ± 10.2
3271.5	0.6	7.6 ± 10.2
3301.5	0.9	-13.2 ± 10.2
3330.3	0.1	-14.7 ± 10.2
3962.6	0.1	-31.0 ± 10.2
4331.5	0.0	-29.4 ± 10.2
4358.5	0.2	-28.3 ± 10.2
4387.3	0.4	0.0 ± 10.2
4393.5	0.5	0.0 ± 10.2
4513.4	0.4	-2.6 ± 10.2
4672.7	0.7	-6.2 ± 10.2
4706.5	1.0	-26.3 ± 10.2
4793.5	0.6	-2.5 ± 10.2
4866.3	0.2	-35.9 ± 10.2
5059.5	0.7	-6.3 ± 10.2
5060.6	0.8	-9.4 ± 10.2
5067.5	0.8	-14.4 ± 10.2
5071.5	0.8	-15.1 ± 10.2
5072.4	0.8	-18.1 ± 10.2
5109.5	0.1	-17.8 ± 10.2
5117.4	0.2	-16.6 ± 10.2

Continuation of Table 22

Date (HJD-2450000)	Phase	Radial velocity (km/s)
5119.4	0.2	-18.0 ± 10.2
5203.4	0.9	-23.5 ± 10.2
5238.3	0.2	-24.2 ± 10.2
5270.3	0.4	-6.3 ± 10.2
5398.5	0.4	-0.4 ± 10.2
5417.5	0.6	3.3 ± 10.2
5418.5	0.6	-0.8 ± 10.2
5455.4	0.9	-23.2 ± 10.2
5534.3	0.5	-15.0 ± 10.2
5559.4	0.7	-13.0 ± 10.2
5774.6	0.4	-7.9 ± 10.2
5775.6	0.4	-11.9 ± 10.2
5777.5	0.4	-13.9 ± 10.2
5785.6	0.5	-9.5 ± 10.2
5828.4	0.8	-20.0 ± 10.2
5831.5	0.8	-31.1 ± 10.2
5857.4	0.0	-40.6 ± 10.2
5879.7	0.2	-18.5 ± 10.2
5907.6	0.4	-2.0 ± 10.2
5956.3	0.8	-23.1 ± 10.2
6143.6	0.3	-1.2 ± 10.2
6150.4	0.4	-0.1 ± 10.2
6163.4	0.5	9.3 ± 10.2
6167.5	0.5	2.7 ± 10.2
6180.3	0.6	11.8 ± 10.2
6204.6	0.8	-10.5 ± 10.2
6206.4	0.8	-9.9 ± 10.2
6260.5	0.2	-13.7 ± 10.2
6267.3	0.3	-4.5 ± 10.2
6270.5	0.3	13.0 ± 10.2
6291.4	0.5	12.1 ± 10.2
6301.4	0.5	14.7 ± 10.2
6490.5	0.0	-10.7 ± 10.2
6556.4	0.6	25.0 ± 10.2
6628.6	0.1	-0.2 ± 10.2
6665.6	0.4	23.8 ± 10.2

Table 23

Radial velocities for Fit 3		
Date (HJD-2450000)	Phase	Radial velocity (km/s)
8017.4	0.1	-41.1 ± 4.5
8018.5	0.1	-41.4 ± 4.5
8034.6	0.2	-36.3 ± 4.5
8041.4	0.2	-32.4 ± 4.5
8041.4	0.2	-28.7 ± 4.5
8057.6	0.4	-25.8 ± 4.5
8072.4	0.5	-28.3 ± 4.5
8073.4	0.5	-23.1 ± 4.5
8073.4	0.5	-28.5 ± 4.5
8077.3	0.5	-22.6 ± 4.5
8078.5	0.5	-23.2 ± 4.5
8085.3	0.6	-28.7 ± 4.5
8092.3	0.6	-34.3 ± 4.5
8094.3	0.7	-34.9 ± 4.5
8094.6	0.7	-26.8 ± 4.5
8100.3	0.7	-35.9 ± 4.5
8106.5	0.8	-36.4 ± 4.5
8133.3	1.0	-47.8 ± 4.5
8328.6	0.5	-25.0 ± 4.5
8329.6	0.5	-25.3 ± 4.5
8333.6	0.6	-24.8 ± 4.5
8339.6	0.6	-30.8 ± 4.5
8345.4	0.6	-30.8 ± 4.5
8352.4	0.7	-32.5 ± 4.5
8364.4	0.8	-23.6 ± 4.5
8377.5	0.9	-45.2 ± 4.5
8388.3	1.0	-50.4 ± 4.5
8412.3	0.2	-43.7 ± 4.5
8414.5	0.2	-40.9 ± 4.5
8428.6	0.3	-33.0 ± 4.5
8142.3	0.0	-54.1 ± 4.5
8147.4	0.1	-45.3 ± 4.5
8158.4	0.2	-39.1 ± 4.5
8159.7	0.2	-48.3 ± 4.5
8162.3	0.2	-37.4 ± 4.5

Continuation of Table 23		
Date (HJD-2450000)	Phase	Radial velocity (km/s)
8177.3	0.3	-24.4 ± 4.5
9076.5	0.4	-31.9 ± 4.5
9097.5	0.6	-28.9 ± 4.5
9100.6	0.6	-30.1 ± 4.5
9101.6	0.6	-31.2 ± 4.5
9106.4	0.7	-31.5 ± 4.5
9110.5	0.7	-32.6 ± 4.5
9115.5	0.7	-35.8 ± 4.5
9329.3	0.4	-24.5 ± 4.5
9481.4	0.6	-19.1 ± 4.5
9496.4	0.7	-30.2 ± 4.5
9515.4	0.9	-36.7 ± 4.5

A.1 Single year radial velocities

Table 24

Radial velocities for 2004			
Date (HJD-2450000)	Radial velocity (km/s)		
	a = 200 km/s	a = 250 km/s	a = 300 km/s
3231.5	-8.0 ± 2.9	5.8 ± 0.5	11.8 ± 0.8
3232.7	-6.7 ± 2.9	5.7 ± 0.5	11.5 ± 0.8
3244.5	0.6 ± 2.9	11.9 ± 0.5	17.2 ± 0.8
3271.5	-5.1 ± 2.9	7.6 ± 0.5	12.4 ± 0.8
3301.5	-18.6 ± 2.9	-13.2 ± 0.5	-2.3 ± 0.8
3330.3	-27.7 ± 2.9	-14.7 ± 0.5	-3.7 ± 0.8

Table 25

Radial velocities for 2010			
Date (HJD-2450000)	Radial velocity (km/s)		
	a = 200 km/s	a = 250 km/s	a = 300 km/s
5203.4	-33.2 ± 6.6	-23.5 ± 6.2	-16.4 ± 8.4
5238.3	-37.4 ± 6.6	-24.2 ± 6.2	-17.6 ± 8.4
5270.3	-15.1 ± 6.6	-6.3 ± 6.2	-6.6 ± 8.4
5398.5	1.6 ± 6.6	-0.4 ± 6.2	-6.9 ± 8.4

Continuation of Table 25			
Date (HJD-2450000)	Radial velocity (km/s)		
	a = 200 km/s	a = 250 km/s	a = 300 km/s
5417.5	8.8 ± 6.6	3.3 ± 6.2	-4.2 ± 8.4
5418.5	5.4 ± 6.6	-0.8 ± 6.2	-9.8 ± 8.4
5455.4	-17.7 ± 6.6	-23.2 ± 6.2	-29.7 ± 8.4
5534.3	-3.9 ± 6.6	-15.0 ± 6.2	-24.4 ± 8.4
5559.4	1.0 ± 6.6	-13.0 ± 6.2	-23.8 ± 8.4

Table 26

Radial velocities for 2011			
Date (HJD-2450000)	Radial velocity (km/s)		
	a = 200 km/s	a = 250 km/s	a = 300 km/s
5774.6	2.0 ± 5.1	-7.9 ± 5.6	-14.0 ± 5.2
5775.6	-1.6 ± 5.1	-11.9 ± 5.6	-17.3 ± 5.2
5777.5	-1.7 ± 5.1	-13.9 ± 5.6	-22.6 ± 5.2
5785.6	3.7 ± 5.1	-9.5 ± 5.6	-14.8 ± 5.2
5828.4	-10.8 ± 5.1	-20.0 ± 5.6	-27.5 ± 5.2
5831.5	-20.8 ± 5.1	-31.1 ± 5.6	-35.1 ± 5.2
5857.4	-33.0 ± 5.1	-40.6 ± 5.6	-45.9 ± 5.2
5879.7	-10.1 ± 5.1	-18.5 ± 5.6	-27.5 ± 5.2
5907.6	9.2 ± 5.1	-2.0 ± 5.6	-7.3 ± 5.2

Table 27

Radial velocities for 2016			
Date (HJD-2450000)	Radial velocity (km/s)		
	a = 200 km/s	a = 250 km/s	a = 300 km/s
7617.6	-25.8 ± 5.2	-23.4 ± 3.6	-17.1 ± 3.5
7638.5	-39.1 ± 5.2	-26.3 ± 3.6	-14.7 ± 3.5
7666.4	-19.4 ± 5.2	-9.1 ± 3.6	-2.6 ± 3.5
7671.5	-13.1 ± 5.2	-4.3 ± 3.6	0.7 ± 3.5
7693.4	1.9 ± 5.2	7.3 ± 3.6	11.2 ± 3.5
7713.6	-12.4 ± 5.2	-8.8 ± 3.6	-3.8 ± 3.5

Table 28

Radial velocities for 2017			
Date (HJD-2450000)	Radial velocity (km/s)		
	$a = 200$ km/s	$a = 250$ km/s	$a = 300$ km/s
7793.6	-12.9 ± 3.4	-10.2 ± 4.2	-9.0 ± 5.2
7989.5	-21.8 ± 3.4	-33.0 ± 4.2	-39.2 ± 5.2
7999.5	-27.3 ± 3.4	-40.6 ± 4.2	-43.1 ± 5.2
8017.4	-31.5 ± 3.4	-38.3 ± 4.2	-41.1 ± 5.2
8018.5	-31.8 ± 3.4	-38.1 ± 4.2	-41.4 ± 5.2
8034.6	-21.4 ± 3.4	-30.8 ± 4.2	-36.3 ± 5.2
8041.4	-16.4 ± 3.4	-27.3 ± 4.2	-32.4 ± 5.2
8041.4	-11.3 ± 3.4	-23.1 ± 4.2	-28.7 ± 5.2
8057.6	-11.3 ± 3.4	-21.0 ± 4.2	-25.8 ± 5.2
8072.4	-7.5 ± 3.4	-21.2 ± 4.2	-28.3 ± 5.2
8073.4	-4.4 ± 3.4	-15.6 ± 4.2	-23.1 ± 5.2
8073.4	-9.4 ± 3.4	-20.4 ± 4.2	-28.5 ± 5.2
8077.3	-4.0 ± 3.4	-15.6 ± 4.2	-22.6 ± 5.2
8078.5	-3.4 ± 3.4	-16.0 ± 4.2	-23.2 ± 5.2
8085.3	-11.3 ± 3.4	-23.3 ± 4.2	-28.7 ± 5.2
8092.3	-15.1 ± 3.4	-29.1 ± 4.2	-34.3 ± 5.2
8094.3	-18.4 ± 3.4	-30.8 ± 4.2	-34.9 ± 5.2
8094.6	-7.7 ± 3.4	-21.4 ± 4.2	-26.8 ± 5.2
8100.3	-19.8 ± 3.4	-32.1 ± 4.2	-35.9 ± 5.2
8106.5	-21.1 ± 3.4	-31.5 ± 4.2	-36.4 ± 5.2

Table 29

Radial velocities for 2018			
Date (HJD-2450000)	Radial velocity (km/s)		
	$a = 200$ km/s	$a = 250$ km/s	$a = 300$ km/s
8133.3	-33.5 ± 4.3	-44.5 ± 4.2	-47.8 ± 4.6
8133.5	-28.7 ± 4.3	-40.5 ± 4.2	-44.0 ± 4.6
8142.3	-34.2 ± 4.3	-48.2 ± 4.2	-54.1 ± 4.6
8147.4	-34.0 ± 4.3	-41.4 ± 4.2	-45.3 ± 4.6
8158.4	-23.9 ± 4.3	-33.6 ± 4.2	-39.1 ± 4.6
8159.7	-31.4 ± 4.3	-42.3 ± 4.2	-48.3 ± 4.6
8162.3	-21.5 ± 4.3	-31.5 ± 4.2	-37.4 ± 4.6
8177.3	-6.8 ± 4.3	-17.4 ± 4.2	-24.4 ± 4.6

Continuation of Table 29			
Date (HJD-2450000)	Radial velocity (km/s)		
	a = 200 km/s	a = 250 km/s	a = 300 km/s
8328.6	-1.8 ± 4.3	-13.3 ± 4.2	-25.0 ± 4.6
8329.6	-2.8 ± 4.3	-15.9 ± 4.2	-25.3 ± 4.6
8333.6	-2.7 ± 4.3	-14.8 ± 4.2	-24.8 ± 4.6
8339.6	-5.4 ± 4.3	-18.5 ± 4.2	-30.8 ± 4.6
8345.4	-10.6 ± 4.3	-23.4 ± 4.2	-30.8 ± 4.6
8352.4	-10.7 ± 4.3	-25.2 ± 4.2	-32.5 ± 4.6
8364.4	-6.1 ± 4.3	-18.3 ± 4.2	-23.6 ± 4.6
8377.5	-30.8 ± 4.3	-41.8 ± 4.2	-45.2 ± 4.6
8388.3	-34.3 ± 4.3	-46.2 ± 4.2	-50.4 ± 4.6
8412.3	-25.6 ± 4.3	-36.4 ± 4.2	-43.7 ± 4.6
8414.5	-23.3 ± 4.3	-34.8 ± 4.2	-40.9 ± 4.6
8428.6	-7.3 ± 4.3	-22.9 ± 4.2	-33.0 ± 4.6
8449.6	1.5 ± 4.3	-15.0 ± 4.2	-26.0 ± 4.6
8466.8	2.2 ± 4.3	-14.1 ± 4.2	-24.1 ± 4.6
8468.6	-4.1 ± 4.3	-19.9 ± 4.2	-28.1 ± 4.6
8472.7	-5.2 ± 4.3	-20.1 ± 4.2	-28.9 ± 4.6

Table 30

Radial velocities for 2019			
Date (HJD-2450000)	Radial velocity (km/s)		
	a = 200 km/s	a = 250 km/s	a = 300 km/s
8487.6	-23.9 ± 2.5	-35.6 ± 2.9	-41.3 ± 3.1
8500.7	-34.4 ± 2.5	-45.0 ± 2.9	-49.9 ± 3.1
8505.7	-36.7 ± 2.5	-48.8 ± 2.9	-52.2 ± 3.1
8521.7	-33.5 ± 2.5	-45.9 ± 2.9	-52.4 ± 3.1
8526.6	-31.2 ± 2.5	-41.9 ± 2.9	-49.1 ± 3.1
8542.6	-19.8 ± 2.5	-31.3 ± 2.9	-38.9 ± 3.1
8557.6	-4.8 ± 2.5	-21.1 ± 2.9	-31.9 ± 3.1
8560.6	-3.6 ± 2.5	-19.5 ± 2.9	-29.4 ± 3.1
8567.7	2.4 ± 2.5	-15.3 ± 2.9	-25.1 ± 3.1
8574.7	-0.4 ± 2.5	-15.3 ± 2.9	-24.9 ± 3.1
8706.6	12.2 ± 2.5	-2.3 ± 2.9	-12.6 ± 3.1
8718.7	-1.0 ± 2.5	-16.2 ± 2.9	-23.2 ± 3.1
8726.6	-7.5 ± 2.5	-25.7 ± 2.9	-34.3 ± 3.1
8730.6	-14.2 ± 2.5	-29.5 ± 2.9	-38.9 ± 3.1

Continuation of Table 30			
Date (HJD-2450000)	Radial velocity (km/s)		
	a = 200 km/s	a = 250 km/s	a = 300 km/s
8730.6	-8.3 ± 2.5	-23.8 ± 2.9	-32.5 ± 3.1
8731.6	-13.0 ± 2.5	-28.7 ± 2.9	-38.4 ± 3.1
8732.6	-12.8 ± 2.5	-29.2 ± 2.9	-39.0 ± 3.1
8738.5	-17.8 ± 2.5	-32.3 ± 2.9	-38.9 ± 3.1
8738.5	-21.1 ± 2.5	-37.9 ± 2.9	-45.3 ± 3.1
8742.5	-25.5 ± 2.5	-39.5 ± 2.9	-45.3 ± 3.1
8743.6	-29.0 ± 2.5	-43.8 ± 2.9	-49.8 ± 3.1
8746.5	-29.7 ± 2.5	-43.8 ± 2.9	-49.7 ± 3.1
8755.5	-35.7 ± 2.5	-47.4 ± 2.9	-52.0 ± 3.1
8757.5	-34.4 ± 2.5	-43.9 ± 2.9	-47.6 ± 3.1
8762.5	-38.4 ± 2.5	-50.4 ± 2.9	-55.0 ± 3.1
8764.5	-35.3 ± 2.5	-48.6 ± 2.9	-54.4 ± 3.1
8766.5	-37.1 ± 2.5	-50.5 ± 2.9	-56.5 ± 3.1
8768.5	-37.3 ± 2.5	-50.6 ± 2.9	-56.8 ± 3.1
8769.5	-34.6 ± 2.5	-47.1 ± 2.9	-52.2 ± 3.1
8770.5	-36.4 ± 2.5	-49.5 ± 2.9	-55.3 ± 3.1
8782.5	-29.1 ± 2.5	-42.6 ± 2.9	-51.3 ± 3.1
8783.5	-27.2 ± 2.5	-39.1 ± 2.9	-48.8 ± 3.1
8794.4	-24.5 ± 2.5	-37.1 ± 2.9	-45.0 ± 3.1
8846.3	-0.4 ± 2.5	-18.4 ± 2.9	-29.4 ± 3.1

A.2 Stable interval radial velocities

Table 31

Radial velocities for Int 1			
Date (HJD-2450000)	Radial velocity (km/s)		
	a = 200 km/s	a = 250 km/s	a = 300 km/s
5534.3	-3.9 ± 5.7	-15.0 ± 5.7	-24.4 ± 5.9
5559.4	1.0 ± 5.7	-13.0 ± 5.7	-23.8 ± 5.9
5774.6	2.0 ± 5.7	-7.9 ± 5.7	-14.0 ± 5.9
5775.6	-1.6 ± 5.7	-11.9 ± 5.7	-17.3 ± 5.9
5777.5	-1.7 ± 5.7	-13.9 ± 5.7	-22.6 ± 5.9
5785.6	3.7 ± 5.7	-9.5 ± 5.7	-14.8 ± 5.9
5828.4	-10.8 ± 5.7	-20.0 ± 5.7	-27.5 ± 5.9
5831.5	-20.8 ± 5.7	-31.1 ± 5.7	-35.1 ± 5.9

Continuation of Table 31			
Date (HJD-2450000)	Radial velocity (km/s)		
	a = 200 km/s	a = 250 km/s	a = 300 km/s
5857.4	-33.0 ± 5.7	-40.6 ± 5.7	-45.9 ± 5.9
5879.7	-10.1 ± 5.7	-18.5 ± 5.7	-27.5 ± 5.9
5907.6	9.2 ± 5.7	-2.0 ± 5.7	-7.3 ± 5.9

Table 32

Radial velocities for Int 2			
Date (HJD-2450000)	Radial velocity (km/s)		
	a = 200 km/s	a = 250 km/s	a = 300 km/s
7638.5	-39.1 ± 3.2	-26.3 ± 3.5	-14.7 ± 5.4
7666.4	-19.4 ± 3.2	-9.1 ± 3.5	-2.6 ± 5.4
7671.5	-13.1 ± 3.2	-4.3 ± 3.5	0.7 ± 5.4
7693.4	1.9 ± 3.2	7.3 ± 3.5	11.2 ± 5.4
7713.6	-12.4 ± 3.2	-8.8 ± 3.5	-3.8 ± 5.4
7793.6	-12.9 ± 3.2	-10.2 ± 3.5	-9.0 ± 5.4

Table 33

Radial velocities for Int 3			
Date (HJD-2450000)	Radial velocity (km/s)		
	a = 200 km/s	a = 250 km/s	a = 300 km/s
8017.4	-31.5 ± 3.2	-38.3 ± 3.0	-41.1 ± 2.8
8018.5	-31.8 ± 3.2	-38.1 ± 3.0	-41.4 ± 2.8
8034.6	-21.4 ± 3.2	-30.8 ± 3.0	-36.3 ± 2.8
8041.4	-16.4 ± 3.2	-27.3 ± 3.0	-32.4 ± 2.8
8041.4	-11.3 ± 3.2	-23.1 ± 3.0	-28.7 ± 2.8
8057.6	-11.3 ± 3.2	-21.0 ± 3.0	-25.8 ± 2.8
8072.4	-7.5 ± 3.2	-21.2 ± 3.0	-28.3 ± 2.8
8073.4	-4.4 ± 3.2	-15.6 ± 3.0	-23.1 ± 2.8
8073.4	-9.4 ± 3.2	-20.4 ± 3.0	-28.5 ± 2.8
8077.3	-4.0 ± 3.2	-15.6 ± 3.0	-22.6 ± 2.8
8078.5	-3.4 ± 3.2	-16.0 ± 3.0	-23.2 ± 2.8
8085.3	-11.3 ± 3.2	-23.3 ± 3.0	-28.7 ± 2.8
8092.3	-15.1 ± 3.2	-29.1 ± 3.0	-34.3 ± 2.8
8094.3	-18.4 ± 3.2	-30.8 ± 3.0	-34.9 ± 2.8

Continuation of Table 33			
Date (HJD-2450000)	Radial velocity (km/s)		
	a = 200 km/s	a = 250 km/s	a = 300 km/s
8094.6	-7.7 ± 3.2	-21.4 ± 3.0	-26.8 ± 2.8
8100.3	-19.8 ± 3.2	-32.1 ± 3.0	-35.9 ± 2.8
8106.5	-21.1 ± 3.2	-31.5 ± 3.0	-36.4 ± 2.8
8133.3	-33.5 ± 3.2	-44.5 ± 3.0	-47.8 ± 2.8

Table 34

Radial velocities for Int 4			
Date (HJD-2450000)	Radial velocity (km/s)		
	a = 200 km/s	a = 250 km/s	a = 300 km/s
8328.6	-1.8 ± 5.3	-13.3 ± 5.0	-25.0 ± 5.1
8329.6	-2.8 ± 5.3	-15.9 ± 5.0	-25.3 ± 5.1
8333.6	-2.7 ± 5.3	-14.8 ± 5.0	-24.8 ± 5.1
8339.6	-5.4 ± 5.3	-18.5 ± 5.0	-30.8 ± 5.1
8345.4	-10.6 ± 5.3	-23.4 ± 5.0	-30.8 ± 5.1
8352.4	-10.7 ± 5.3	-25.2 ± 5.0	-32.5 ± 5.1
8364.4	-6.1 ± 5.3	-18.3 ± 5.0	-23.6 ± 5.1
8377.5	-30.8 ± 5.3	-41.8 ± 5.0	-45.2 ± 5.1
8388.3	-34.3 ± 5.3	-46.2 ± 5.0	-50.4 ± 5.1
8412.3	-25.6 ± 5.3	-36.4 ± 5.0	-43.7 ± 5.1
8414.5	-23.3 ± 5.3	-34.8 ± 5.0	-40.9 ± 5.1
8428.6	-7.3 ± 5.3	-22.9 ± 5.0	-33.0 ± 5.1

B Appendix: Additional phase plots.

This appendix contains the phase plots for the single year and single interval fits presented in Section 4.2.1. The error bars correspond to each fit's RMS deviation.

B.1 Single year fits

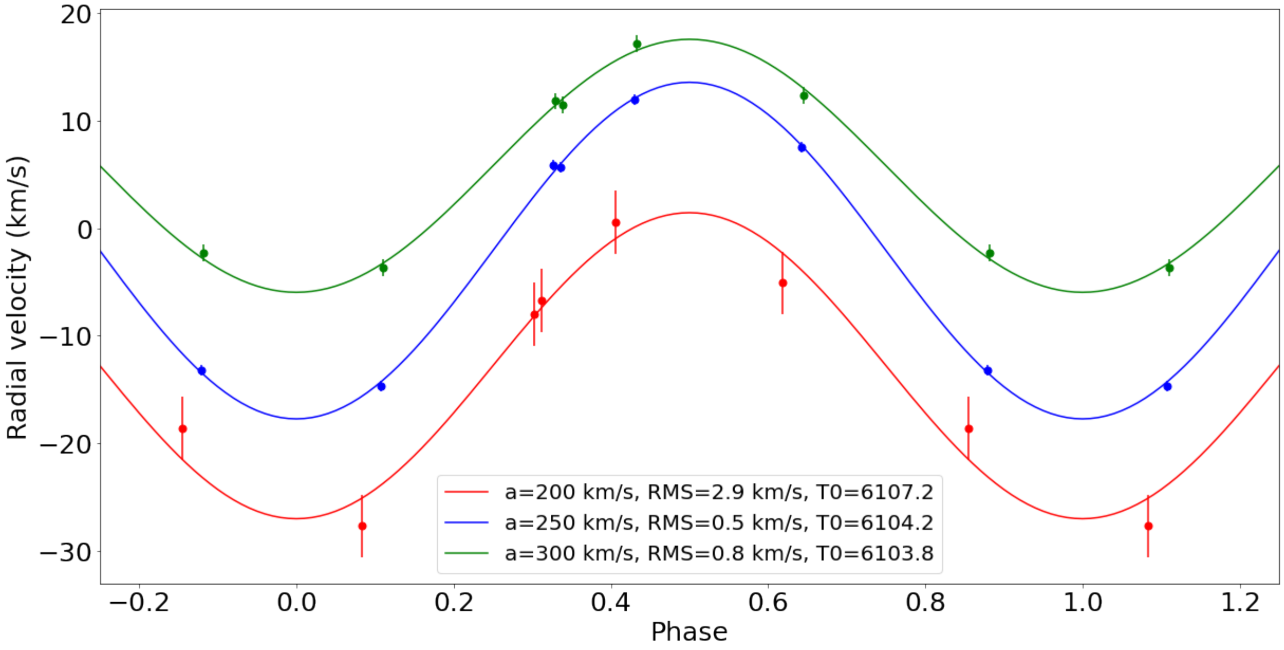

Figure 55: Radial velocities by phase for 2004.

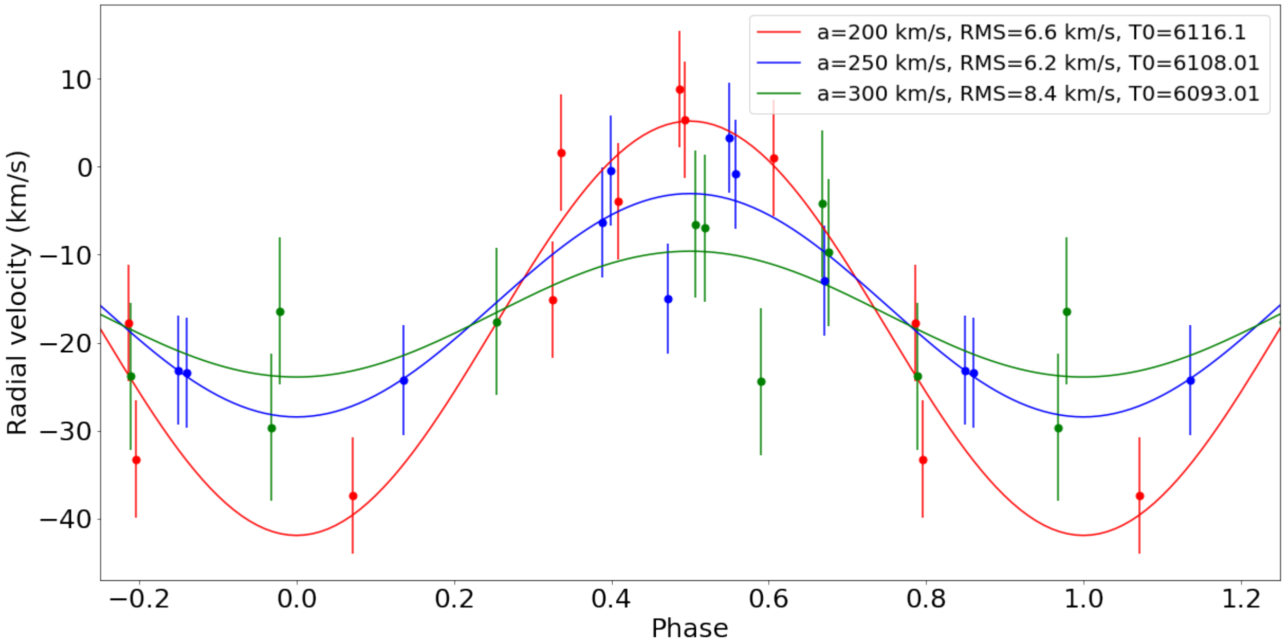

Figure 56: Radial velocities by phase for 2010.

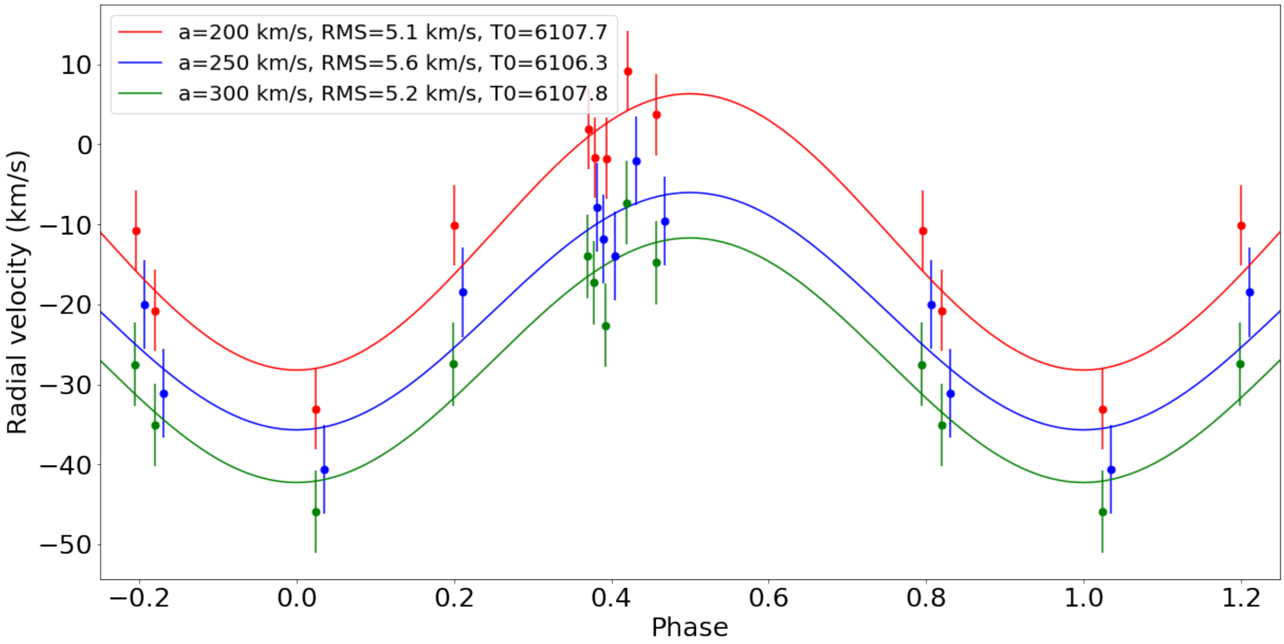

Figure 57: Radial velocities by phase for 2011.

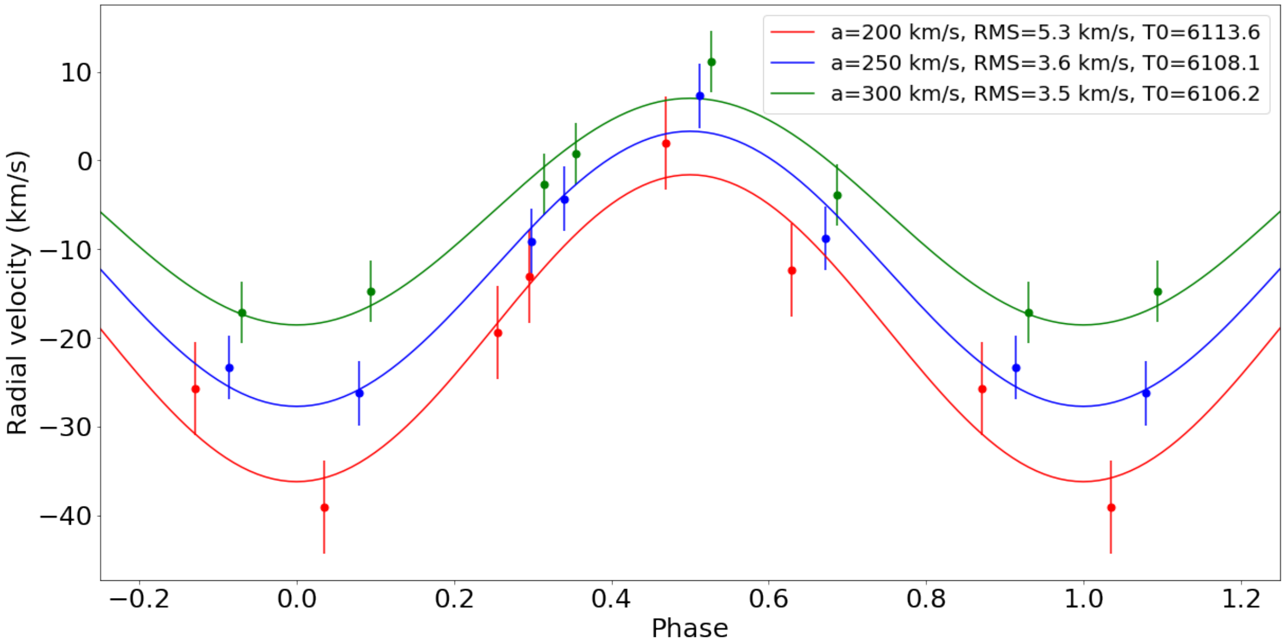

Figure 58: Radial velocities by phase for 2016.

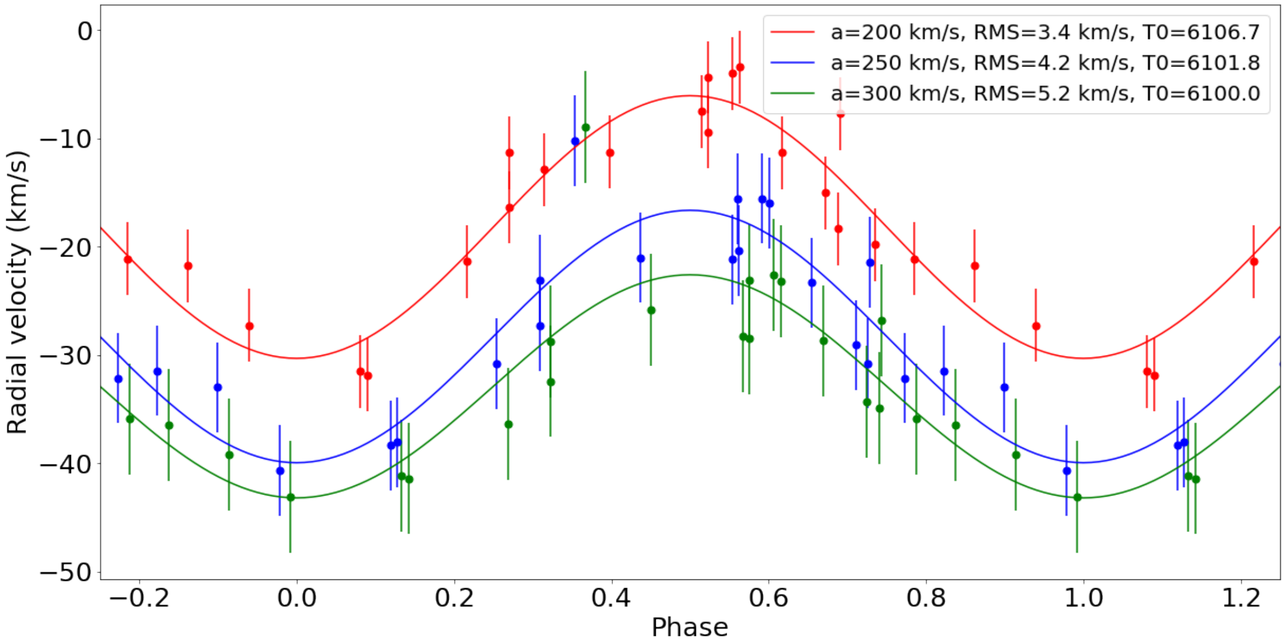

Figure 59: Radial velocities by phase for 2017.

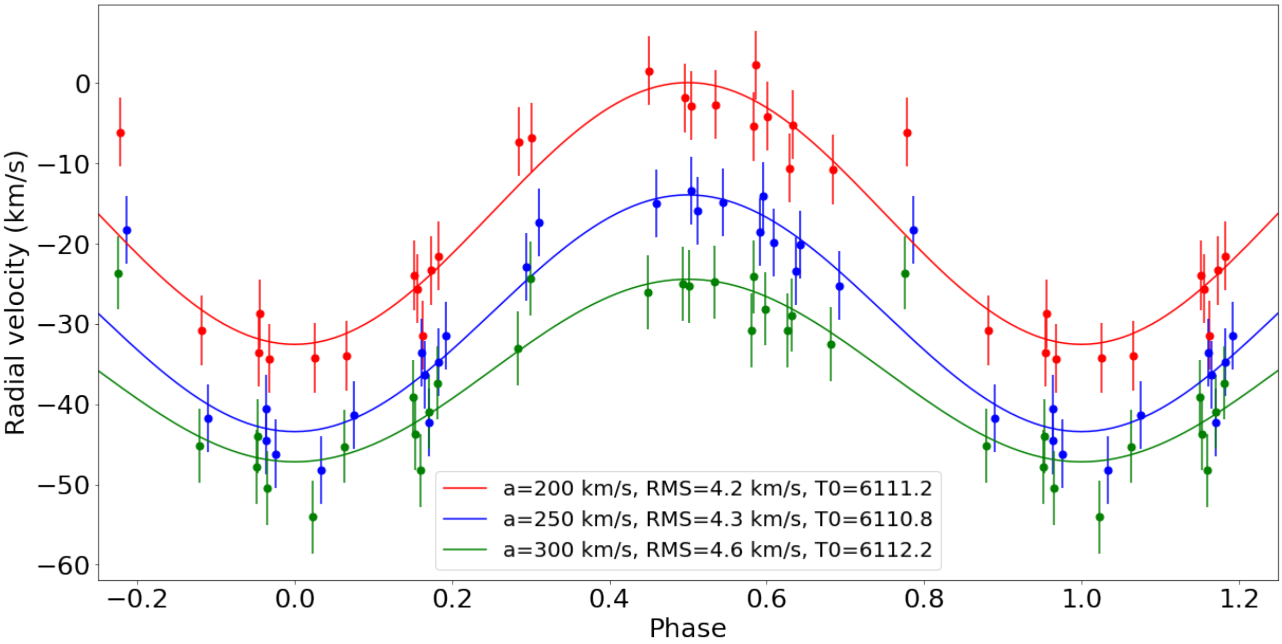

Figure 60: Radial velocities by phase for 2018.

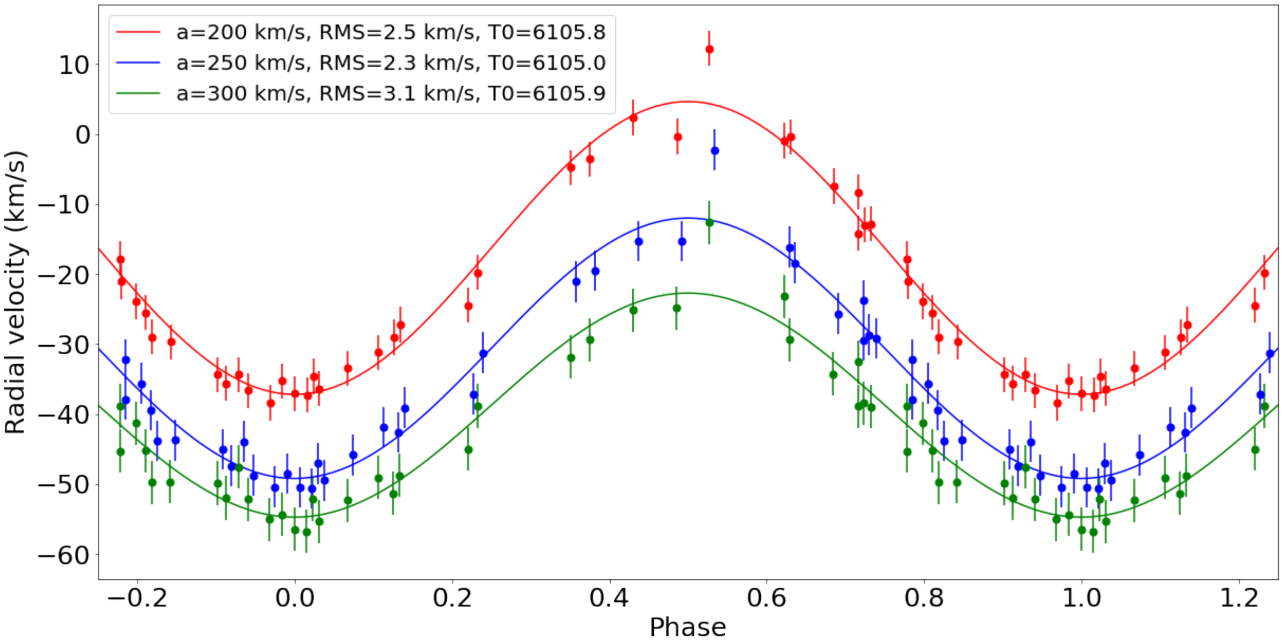

Figure 61: Radial velocities by phase for 2019.

B.2 Stable interval fits

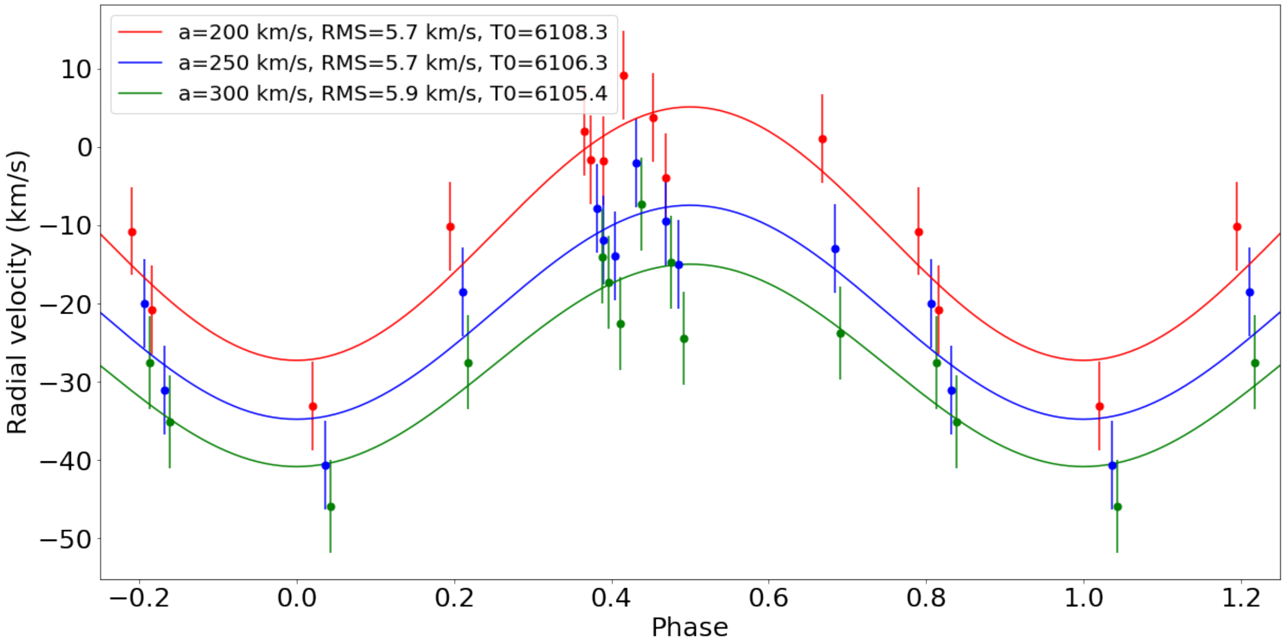

Figure 62: Radial velocities by phase for Int 1.

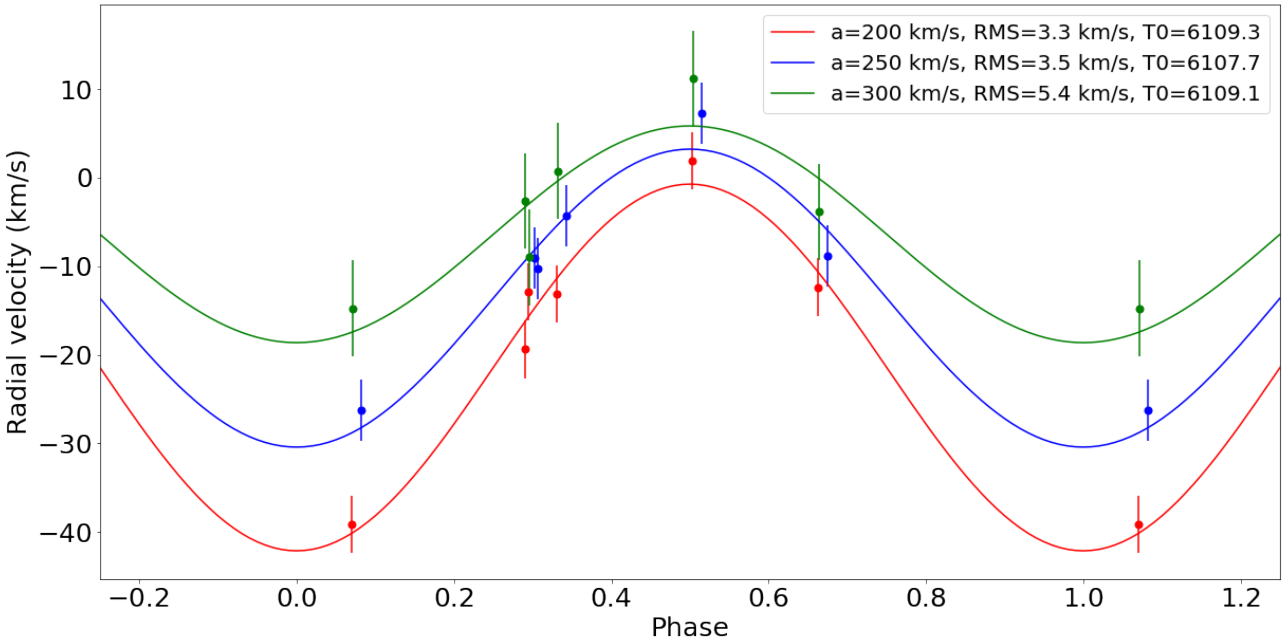

Figure 63: Radial velocities by phase for Int 2.

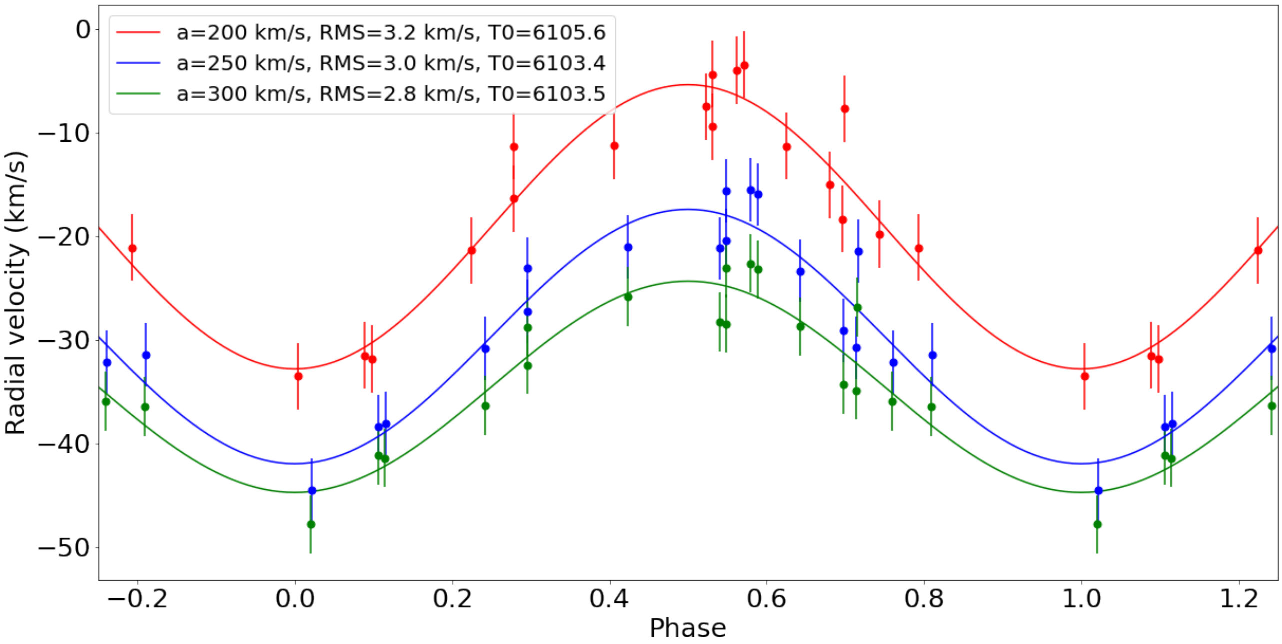

Figure 64: Radial velocities by phase for Int 3.

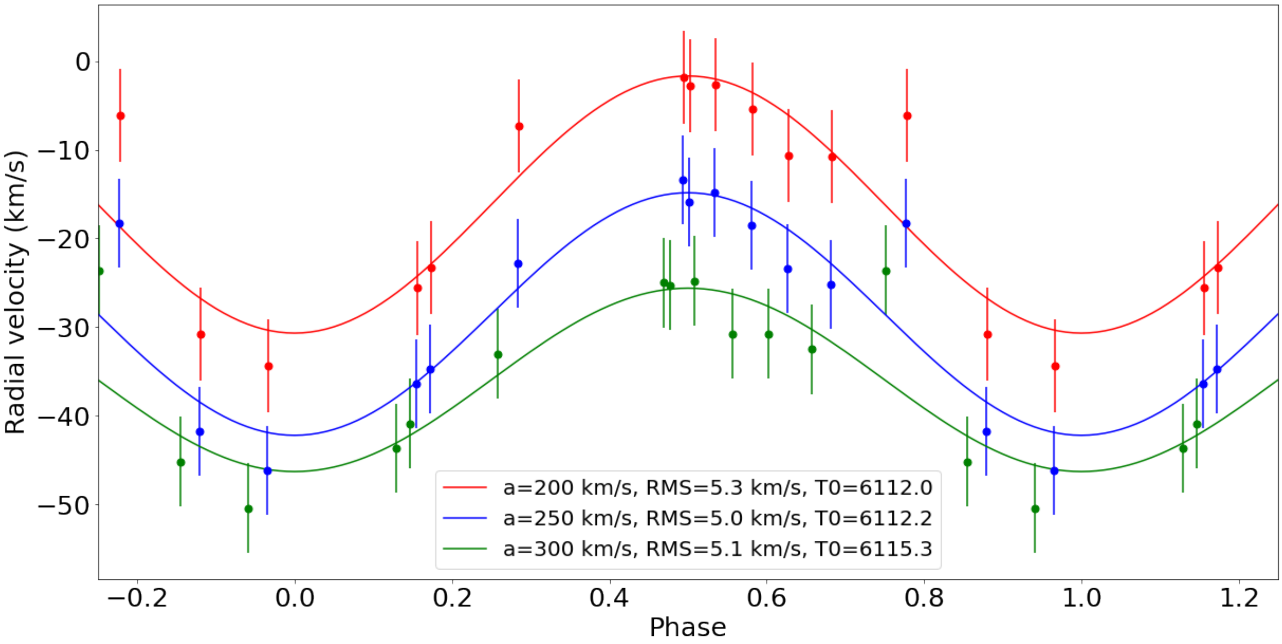

Figure 65: Radial velocities by phase for Int 4.